

ERROR ESTIMATES FOR THE CONVOLUTION BACKPROJECTION ALGORITHM IN COMPUTERIZED TOMOGRAPHY

**A Thesis Submitted
In Partial Fulfilment of the Requirements
for the Degree of**

DOCTOR OF PHILOSOPHY

by

PRABHAT MUNSHI

to the

**NUCLEAR ENGINEERING AND TECHNOLOGY PROGRAMME
INDIAN INSTITUTE OF TECHNOLOGY, KANPUR**

MAY, 1988

NOV 1988

LIBRARY

106303...

NETP-1988-D-MUN-ERR

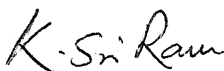
DEDICATED

TO

MY PARENTS

CERTIFICATE

This is to certify that the thesis entitled,
"ERROR ESTIMATES FOR THE CONVOLUTION BACKPROJECTION
ALGORITHM IN COMPUTERIZED TOMOGRAPHY" by Prabhat
Munshi has been carried out under our supervision and
has not been submitted elsewhere for a degree.



(Dr. K. Sri Ram)
Professor and Head
Nuclear Engg. & Tech. Programme
Indian Institute of Technology
Kanpur



(Dr. R.K.S. Rathore)
Professor
Department of Mathematics
Indian Institute of Technology
Kanpur



(Dr. M.S. Kalra)
Assistant Professor
Nuclear Engg. and Tech. Programme
Indian Institute of Technology
Kanpur

May, 1988.

ACKNOWLEDGEMENTS

I wish to express my thanks and deep sense of gratitude to my teachers and supervisors Professors K. Sri Ram, R.K.S. Rathore and M.S. Kalra for their invaluable advice and guidance during the course of the study. The patience and understanding of Prof. R.K.S. Rathore is particularly appreciated for introducing me to mathematical analysis.

I would also like to thank my other teachers, Professors B.P. Singh and A. Sengupta.

It has been a pleasure to have been associated with Professors I.D. Dhariyal and G.P. Kapoor with whom I have had many fruitful discussions.

I would like to thank the staff of NET, Mr.V.S. Tomar, Mr. S. Yadav, Mr. Gopal, Mr. S.S. Pathak, and Mr. R.S. Tripathi, for their co-operation and help.

Thanks are due to Pankaj and Richa for their timely assistance. The help of Akhil and Soami is also appreciated.

And, finally, a special note of thanks to Anu, for her help, covert and overt, which has been there throughout the course of the study.

I take this opportunity to thank Mr. U.S. Mishra for skilful typing of the thesis.

TABLE OF CONTENTS

	<u>Page</u>
LIST OF TABLES	vi)
LIST OF FIGURES	vii)
NOMENCLATURE	ix)
SYNOPSIS	xi)
CHAPTER 1	
INTRODUCTION	1
1.1 Overview	1
1.2 Brief Summary of A Few Related Works	3
1.3 Some Non-Medical Applications of CT	12
CHAPTER 2	
PRELIMINARIES	14
2.1 The CBP Algorithm	14
2.2 The Window Functions	17
2.3 Some Definitions	20
2.4 Theorem	23
CHAPTER 3	
DIRECT THEOREMS	26
3.1 Definitions	26
3.2 Lemmas	27
3.3 The ω_c -Estimate	29
3.4 The Asymptotic Formula	31
3.5 The $ f _{2m}$ Estimate	34
3.6 Localization Lemma	35
CHAPTER 4	
INVERSE THEOREM	37
4.1 Lemmas	37
4.2 Theorem	47
CHAPTER 5	
RESULTS	50
5.1 Reconstruction of a Unit Pixel	54
5.2 Reconstruction of a Simulation of a Damaged Nuclear Fuel-Bundle (NFB)	60
5.3 Reconstruction of a Simulation of a Human-brain Cross Section	72

Page

CHAPTER 6	DISCUSSION	89
	6.1 The Asymptotic Formula	92
	6.2 The ω_c -Estimate	92
	6.3 The Inverse Theorem	93
	Appendix A	95
	Appendix B	118
	Appendix C	141
	References	145

LIST OF TABLES

<u>Table</u>	<u>Title</u>	<u>Page</u>
2.1	Some commonly used window functions	16
5.1	Windows considered in the study	51
5.2	Reconstruction parameters	59
5.3	Reconstruction results for the unit pixel	61
5.4	Effect of cut-off frequency, R_c , on reconstruction errors for the nuclear fuel bundle	70
5.5	Normalized errors corresponding to Table (5.4)	71
5.6	Summary of errors in the reconstruction of human-brain	84
5.7	Normalized errors corresponding to Table (5.6).	85

LIST OF FIGURES

<u>Figure</u>	<u>Title</u>	<u>Page</u>
1.1	Parallel beam data collection geometry	5
1.2	Fan beam data collection geometry	6
5.1	Unit pixel response for (a) H99 window (b) H91 window	55
5.2	Unit pixel response for (a) Sinc window (b) H80 window	56
5.3	Unit pixel response for (a) H75 window (b) Cos window	57
5.4	Unit pixel response for (a) H54 window	58
5.5	Original simulation of damaged nuclear fuel bundle (NFB)	62
5.6	Reconstruction of NFB with H99 window for (a) $R_c = 16$ (b) $R_c = 32$ (c) $R_c = 64$	63
5.7	Reconstruction of NFB with H91 window for (a) $R_c = 16$ (b) $R_c = 32$ (c) $R_c = 64$	64
5.8	Reconstruction of NFB with Sinc window for (a) $R_c = 16$ (b) $R_c = 32$ (c) $R_c = 64$	65
5.9	Reconstruction of NFB with H80 window for (a) $R_c = 16$ (b) $R_c = 32$ (c) $R_c = 64$	66
5.10	Reconstruction of NFB with H75 window for (a) $R_c = 16$ (b) $R_c = 32$ (c) $R_c = 64$	67
5.11	Reconstruction of NFB with Cos window for (a) $R_c = 16$ (b) $R_c = 32$ (c) $R_c = 64$	68
5.12	Reconstruction of NFB with H54 window for (a) $R_c = 16$ (b) $R_c = 32$ (c) $R_c = 64$	69
5.13	Comparative performance (on NFB) of various windows for $R_c = 16$	73
5.14	Comparative performance (on NFB) of various windows for $R_c = 32$	74
5.15	Comparative performance (on NFB) of various windows for $R_c = 64$	75

<u>Figure</u>	<u>Title</u>	<u>Page</u>
5.16	Original simulation of human-brain	76
5.17	Reconstruction of human-brain with H99 window for (a) $R_c = 16$ (b) $R_c = 32$ (c) $R_c = 64$	77
5.18	Reconstruction of human-brain with H91 window for (a) $R_c = 16$ (b) $R_c = 32$ (c) $R_c = 64$	78
5.19	Reconstruction of human-brain with Sinc window for (a) $R_c = 16$ (b) $R_c = 32$ (c) $R_c = 64$	79
5.20	Reconstruction of human-brain with H80 window for (a) $R_c = 16$ (b) $R_c = 32$ (c) $R_c = 64$	80
5.21	Reconstruction of human-brain with H75 window for (a) $R_c = 16$ (b) $R_c = 32$ (c) $R_c = 64$	81
5.22	Reconstruction of human-brain with Cos window for (a) $R_c = 16$ (b) $R_c = 32$ (c) $R_c = 64$	82
5.23	Reconstruction of human-brain with H54 window for (a) $R_c = 16$ (b) $R_c = 32$ (c) $R_c = 64$	83
5.24	Comparative performance (on brain) of various windows for $R_c = 16$	86
5.25	Comparative performance (on brain) of various windows for $R_c = 32$	87
5.26	Comparative performance (on brain) of various windows for $R_c = 64$.	88

NOMENCLATURE

$ \cdot $	norm
\mathbb{R}^n	n-dimensional space (Eucledian)
S^{n-1}	unit sphere in \mathbb{R}^n
$x \cdot \theta$	inner product of x and θ
r, ϕ	polar co-ordinates
x, y	cartesian co-ordinates
f	cross section of interest
\tilde{f}	reconstructed f
$f * K$	convolution of f and K
s	perpendicular distance of data ray (parallel beam geometry)
θ	source direction (parallel beam geometry)
σ	angle of data ray from central ray (fan beam geometry)
β	source direction (fan beam geometry)
Δs	ray-spacing
$\Delta \theta$	source-direction-spacing
$p(s, \theta)$	projection data (parallel beam geometry)
$g(\sigma, \beta)$	projection data (fan beam geometry)
M	integer
M^+	$\left. \begin{array}{l} (M+1)/2 \\ -(M-1)/2 \end{array} \right\} M \text{ odd}$
M^-	
M^+	$\left. \begin{array}{l} M/2 - 1 \\ -M/2 \end{array} \right\} M \text{ even}$
M^-	

$\hat{\cdot}$, FT	Fourier transform
v	inverse Fourier transform
NRAY	total number of data-rays in a projection view
NVIEW	total number of projections view
R	Fourier frequency
R_c	Fourier frequency cut-off

SYNOPSIS

The concept of Computerized Tomography (CT) has been successfully applied in the areas of diagnostic radiology and non-destructive testing. Research continues in the CT area towards the development of more efficient CT machines and reconstruction algorithms so as to further improve the quality of reconstructed images. In this regard, a theoretical analysis of various errors in the reconstruction process becomes extremely important.

Various algorithms for CT reconstruction have been reported in literature, e.g., Direct Fourier Inversion, Convolution Backprojection (CBP), ART, SIRT, etc. Of the numerous methods reported, the CBP algorithm has been used widely as it is efficient, reasonably accurate, and easy to use. Some error estimates for this CBP algorithm have been developed by Natterer. These estimates incorporate the assumption of the cross section (being imaged) having an essentially band-limited projection data.

Generally, cross sections have a finite support and, hence, the projection data is necessarily not band-limited. Nevertheless, due to a finite frequency cut-off, R_c , incorporated in the implementation of the CBP method, the approximation obtained is band-limited. The present thesis deals with this inherent error, e_R , in the CBP approximation arising due to this band limiting aspect. Some direct and inverse results pertaining

to e_R have been established. The analysis assumes perfect (noise-free) data, and a continuous implementation of the convolution and backprojection integrals. A practical implementation of the CBP algorithm will introduce, apart from e_R , the discretization errors (studied by Natterer) arising due to discrete implementation of the convolution and backprojection integrals. Numerical experiments were carried out on cross sections simulating a damaged nuclear fuel bundle and a cancerous human brain.

The main results of the thesis are as follows:

- (a) If the convolution and the backprojection steps are properly discretized, then an arbitrary continuous cross section can be reconstructed using a sufficiently large Fourier cut-off frequency.
- (b) The quality of the reconstructed image is essentially governed by the flatness of the window function in the neighbourhood of origin.
- (c) The pointwise inherent error, e_R , depends on the radial smoothness of the cross section at the point under consideration.

A chapterwise summary of the thesis is as follows:

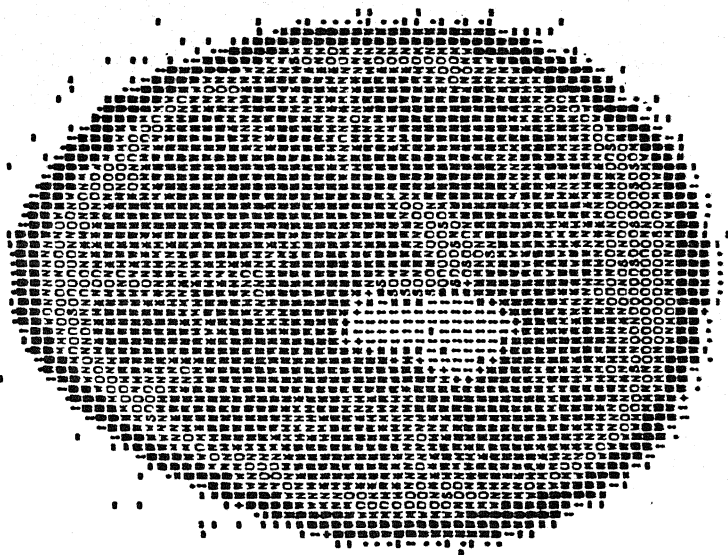
Chapter 1 contains a brief outline of the development of the theory of CT starting from Radon's original work of 1917. The convolution backprojection (CBP) algorithm is briefly

described and the window functions are introduced. Some of the previous works of Bracewell and Riddle, Ramachandran and Lakshminarayanan, Shepp and Logan, and Herman and Naparstek are recalled. Some estimates of the discretization errors developed by Natterer have been summarised.

In Chapter 2 'circular' Sobolev spaces Ω_{2m} , m a positive integer, and related interpolation spaces Ω_{2m}^β , $0 < \beta < 2m$, are introduced. These spaces, used subsequently in Chapters 3 and 4, are defined with the help of certain radially-averaged (RADAV) derivatives, $D_{r,\phi}^k$. These derivatives are also used to define the moduli of smoothness, $\omega_c(f^{[k]}; \delta)$ which serve to classify the smoothness properties of the cross sections. Also defined here is a class $|K_{2m}$ consisting of radially symmetric kernel functions $K(r)$ possessing certain smoothness and integrability requirements. The parallel beam tomographic inversion formula is shown to be a two dimensional convolution of the cross section f , with a radially symmetric kernel $K(r)$ belonging to $|K_{2m}$. The kernels corresponding to the popular functions, e.g., the sinc, cosine and generalized hamming windows, are shown to belong to $|K_{2m}$ where m equals 1.

In Chapter 3 some direct results pertaining to e_R are established. Some of these results estimate e_R in terms of $\omega_c(f^{[k]}; \delta)$, and the Fourier frequency cut-off, R_c . A pointwise asymptotic formula (for e_R) is derived. It

MANBW/257.64 F64X64 CODED PICTUREMPICW 64MPICW 64XANGLEW 200MAX= 128FW MAX= 31C=1180R=01W=01V=01F=00P=00R=00C=00F=10.00000



MINO -5MAX= 7ERROR= 0.75840CMON= 0.05311MPICW= 3332MPICW= 2512EMIN= -5.492392EMAX= 6.554502ELI= 0.911092EL2= 1.33779

Fig. B-5.20 (b) - Computer Output.

APPENDIX C

involves the RADAV derivatives, $D_{r,\phi}^k f(X)$, of the cross section f at the point X . An e_R -error estimate is also obtained for functions belonging to the class Ω_{2m} . The last result to this chapter, a localization lemma, shows the essential reconstruction equivalence of two different kernels which agree in the neighbourhood of origin.

Chapter 4, the kernel of the thesis, is devoted to the following inverse problem:

For what cross section f , the error e_R is $O(R_C^{-\beta})$, where $0 < \beta < 2m$? It is proved, herein, that such cross sections f are precisely the members of the interpolation space Ω_{2m}^β , i.e., e_R is $O(R_C^{-\beta})$, $0 < \beta < 2m$, if and only if, f belongs to Ω_{2m}^β .

Chapter 5 summarises the results of reconstructions performed using a discrete implementation of the CBP algorithm. Test runs were carried out on a unit pixel. A damaged nuclear fuel bundle was simulated and reconstruction experiments were carried out for several windows and varying values of R_C . The number of data rays and projection views were linked to R_C as per the sampling criterion and the optimality criterion. A relatively smooth image representing a cancerous human-brain was also processed by the CBP algorithm. The error measures chosen in the study represented the overall l_1, l_2 , sup, and inf errors in the region of interest. The summary of errors reveals that for a fixed window the overall error for both

the images is approximately $O(1/R_c)$.

Chapter 6 incorporates a brief discussion of the numerical results from the viewpoint of the image quality, the choice of appropriate error measures, and the smoothness aspect of the images used in the study.

CHAPTER 1

INTRODUCTION

1.1 Overview

The development of imaging systems based on the concept of Computerized Tomography (CT) has revolutionized the area of diagnostic radiology and non-destructive testing (NDT). The present day CT scanners are capable of detecting cancerous tissues at a very early stage which had not been the case with the usual X-ray machines. The CT methodology aims at 'reconstructing' the cross section (object function) of interest, from the 'projection' data taken by the CT machine. The physics and the mathematics of CT upto year 1986 has been covered in the works of Herman [1], Natterer [2] and Deans [3]. A careful study of the literature reveals the existence of several algorithms developed for reconstruction of two dimensional functions from their projection data. One such method is the convolution backprojection (CBP) algorithm which is used widely in various areas. The CBP algorithm has proved itself to be fast, relatively efficient, and easy to implement, thus making it quite attractive and competitive compared to various other methods reported in literature.

In the present work, an attempt is made towards the development of some error estimates for the CBP method. Such theoretical understanding, of the various errors involved in the reconstruction process, becomes quite important in studying the interplay of various parameters related to the design of the CT machine, and, the implementation aspect of the CT algorithm.

For perfect (noise-free) data, the major sources of error in the CBP algorithm may be characterized as,

- (i) the inherent error, e_R ,
- (ii) the convolution discretization error, e_C , and
- (iii) the backprojection discretization error, e_B .

These errors have been described in detail in Section 2.1.

For cross sections having a band-limited projection data, using an appropriate convolving function (e.g. band limited), the inherent error, e_R , could be made zero. However, cross sections generally have a finite support and, hence, the projection data is necessarily not band-limited. Nevertheless, due to a finite Fourier frequency cut-off, R_C , incorporated in the implementation of the CBP method, the approximation obtained is band limited. The inherent error, e_R , arises due to this band-limiting aspect.

The present thesis deals with this error, e_R , for the CBP algorithm. The estimates and the pointwise asymptotic formula developed in this work involve e_R , the smoothness of the cross section (function) at the point of interest, the Fourier cut-off frequency, and certain derivatives of the 'window' functions. An inverse theorem associates a precise order of approximation error, e_R , for functions belonging to a certain smoothness class.

1.2 Brief Summary of A Few Related Works

The first inversion formula to calculate a two dimensional function f from its line integrals owes its origin to the work of Radon [4] published in the year 1917. It is given by,

$$f(x) = - \frac{1}{\pi} \int_0^{\infty} \frac{dF_x(s)}{s} \quad (1.1)$$

where,

$$F_x(s) = \frac{1}{2\pi} \int_0^1 p(\theta, x \cdot \theta + s) d\theta \quad (1.2)$$

and,

$$p(\theta, s) = \int_{x \cdot \theta = s} f(x) dx \quad (1.3)$$

We note that p is the "projection-data" which is a set of integrals along the lines perpendicular to θ with

(signed) distance s from the origin. Here $\theta \in \mathbb{S}^1$ and $s \in \mathbb{R}^1$. Figure (1.1) shows the geometry of data-collection incorporated in Equations (1.1) to (1.3). This arrangement of source-detector systems is referred to as 'parallel-beam' geometry.

Herman and Naparstek [5] derived the inversion formula for a 'fan-beam' geometry in which a single rotating source is sufficient for an outer ring of stationary detectors (See Fig. 1.2). The reconstruction is achieved by the following equations:

$$f(r, \phi) = \frac{1}{4\pi^2} \int_0^{2\pi} \int_{-\delta}^{\delta} \frac{1}{\sin(\sigma' - \sigma)} D_v g(\sigma, \beta) d\sigma d\beta \quad (1.4)$$

where, δ is the object radius,

$$\sigma' = \tan^{-1} \left(\frac{r \cos(\beta - \phi)}{D + r \sin(\beta - \phi)} \right) \quad (1.5)$$

$$U = [(r \cos(\beta - \phi))^2 + (D + r \sin(\beta - \phi))^2]^{1/2} \quad (1.6)$$

and

$$D_v g(\sigma, \beta) = \frac{1}{U} \left[\frac{\partial g}{\partial \sigma} - \frac{\partial g}{\partial \beta} \right]. \quad (1.7)$$

Here $g(\sigma, \beta)$ is the projection data collected in the fan-beam mode and D is the distance of the source from the object-centre. A practical implementation requires 'regularization' of the singular integral in Eq.(1.4).

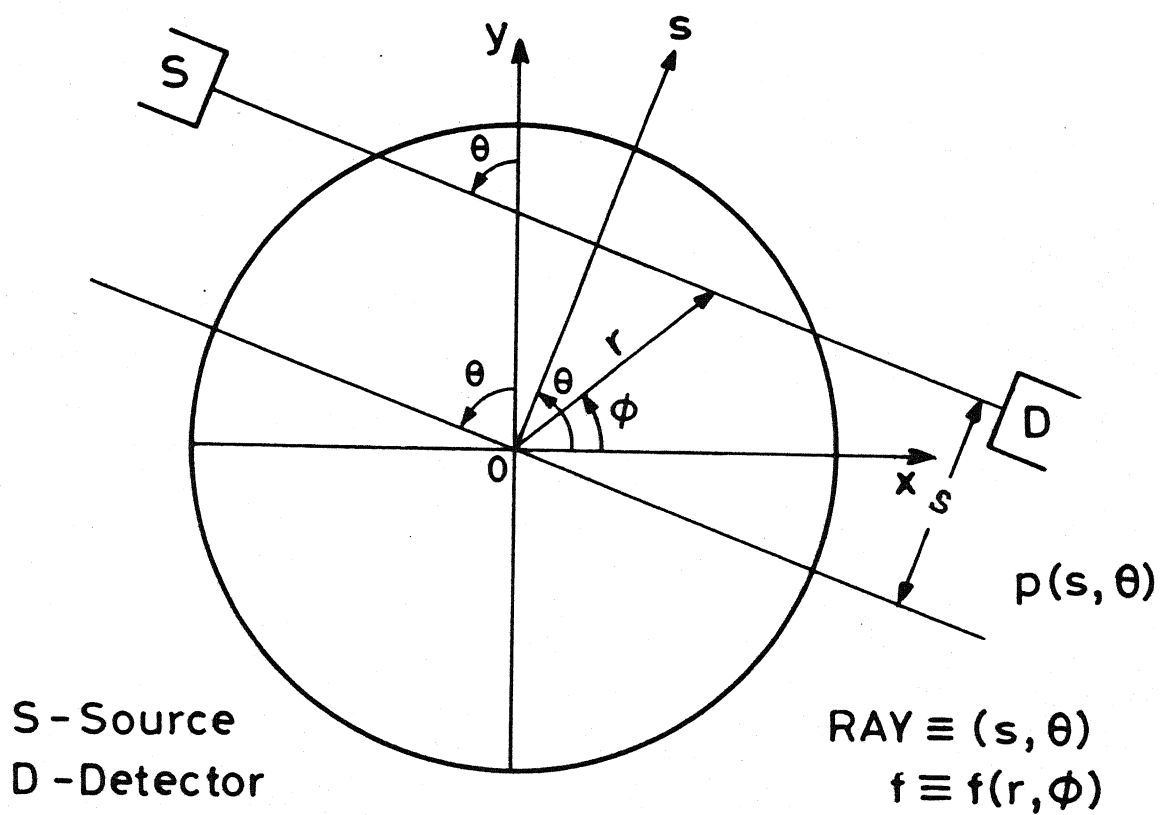


Fig.1.1 Parallel beam collection geometry .

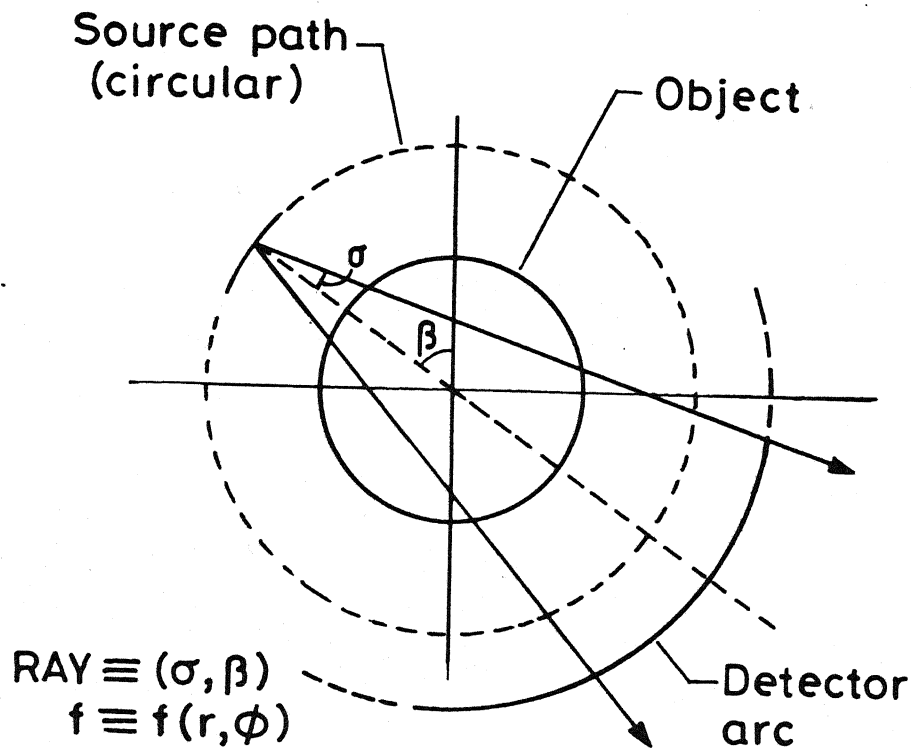


Fig. 1.2 Fan-beam data collection geometry.

An alternate to the Radon Inversion Formula involving Fourier Transform (FT) is given by the Projection-Slice Theorem [2]. The theorem states the equivalence of, the 2-dimensional FT of the object-function, and, the 1-dimensional FT (w.r.t. the variable s) of the projection data, p . Symbolically,

$$\hat{p}(R, \theta) = \hat{f}(R \cos \theta, R \sin \theta) \quad (1.8)$$

A 2-d Fourier inversion of the equation above leads to the well know tomographic formula,

$$f(r, \phi) = \int_0^\pi \int_{-\infty}^{\infty} \hat{p}(R, \theta) e^{i2\pi Rr \cos(\theta - \phi)} |R| dR d\theta \quad (1.9)$$

where,

$$\hat{p}(R, \theta) = \int_{-\infty}^{\infty} p(s, \theta) e^{-i2\pi Rs} ds$$

Here the data-collection geometry is of parallel-beam type.

In a practical implementation of Eq.(1.9), the factor $|R|$ in the integrand is replaced by $|R| W(R)$ where $W(R)$ is a suitable window function. Normally, $W(R)$ is an even function of R , the Fourier frequency, and has a compact support $[-R_c, R_c]$. If the frequency content of p is also supported in $[-R_c, R_c]$, i.e., if $\hat{p}(R, \theta)$ vanishes for $|R| > R_c$, then the filtered

version, with $W(R) = 1$ for $R \in [-R_c, R_c]$,

$$\tilde{f}(r, \phi) = \int_0^\pi \int_{-\infty}^\infty \hat{p}(R, \theta) e^{i2\pi Rr \cos(\theta - \phi)} |R| W(R) dR d\theta \quad (1.9a)$$

agrees with $f(r, \phi)$. In a general case the introduction of $W(R)$ with a finite cut-off R_c helps in stabilizing the singular nature of the integral. An implementation of Eq.(1.9a) in the spatial domain takes the form,

$$\tilde{f}(r, \phi) = \int_0^\pi \int_{-\infty}^\infty p(s, \theta) q(s' - s) ds d\theta \quad (1.9b)$$

where,

$$s' = r \cos(\theta - \phi)$$

and,

$$q(s) = \int_{-\infty}^\infty |R| W(R) e^{i2\pi Rs} dR \quad (1.10)$$

The inner integral in Eq.(1.9b) is a 1-d convolution, while the outer integral corresponds to the backprojection operation, thus giving rise to the name 'convolution backprojection'. The CBP method is also known as the filtered backprojection method indicating 'filtering' of the projection data, p , by the window function, $W(R)$.

The practical implementation suggested by Eq.(1.9a) was initially carried out by Bracewell and Riddle [6] in

radio astronomy. Ramachandran and Lakshminarayanan [7] described a parallel-beam implementation which took care of the discrete nature of data. In both of those works, the band-limiting window

$$W(R) = \begin{cases} 1 & , \quad |R| \leq R_c, \\ 0 & , \quad |R| > R_c, \end{cases}$$

was used.

Shepp and Logan [8] suggested the use of 'sinc' windows given by,

$$W(R) = \begin{cases} \frac{\text{Sin}(\pi R/2R_c)}{(\pi R/2R_c)} & , \quad |R| \leq R_c \\ 0 & , \quad |R| > R_c \end{cases} .$$

Several other window functions have been reported in literature [9]. We note that these windows are radially symmetric in the Fourier space.

In a practical situation where the projection data is discrete, a recommended value of R_c based on the Sampling Theorem [2] is given by,

$$R_c \geq 1/(2\Delta s)$$

where Δs is the spacing between the data rays.

Error estimates for the CBP algorithm have been reported by Natterer [2]. The theorem states (for a 2d function f) that the errors in the CBP scheme are given by e_1 and e_2 , where,

$$e_1 \leq \frac{1}{2} \epsilon_0^* (f, b) \quad (1.11)$$

and,

$$e_2 \leq \|f\|_{L_\infty(\Omega_n)} \eta(1, m) \quad (1.12)$$

where,

$$\epsilon_0^* (f, b) = 2\pi \sup_{\theta \in S^1} \int_{|\sigma_N| \geq b} |\sigma_N| |\hat{f}(\sigma\theta)| d\sigma. \quad (1.13)$$

Here ϵ_0^* is the error introduced by assuming the function f to be "b-bandlimited". We note that in Eqs. (1.11) - (1.13) the symbols σ_N and b are the same as R and R_c of Eqs. (1.9) - (1.10). These errors are introduced by the discretization of the continuous integrals occurring in the inversion formula. If a function is essentially b band-limited the term, ϵ_0^* , is negligible and the error in CBP method is strictly due to the discretization of the back-projection integral. We note that in Eqs. (1.11) - (1.13) it is assumed that $b \leq 1/m$ and $b \leq \pi/\Delta s$, where the back-projection quadrature rule is exact for even

spherical harmonics of degree $2m$ and $0 < \lambda < 1$. Here, η admits an estimate of the form $0 \leq \eta(1, b) \leq C(1)e^{-\lambda(1)b}$, provided C, λ , and B are positive numbers, and $b > B(1)$.

Natterer [10] has developed reconstruction error bounds for functions, f , belonging to certain Sobolev spaces, H^α , given by,

$$\|f\|_{H^\alpha(\mathbb{R}^2)}^2 = \int_{\mathbb{R}^2} (1+|R|^2)^\alpha |\hat{f}(R)|^2 dR < \infty, \quad (1.14)$$

where α is real. The reconstruction error, r , is defined as,

$$r(\alpha, n, \epsilon) = \sup \{ \|f_1 - f_2\|_{L_2(\Omega)} : \|\tilde{R}f_i - p\|_n \leq \epsilon, \\ \|f_i\|_{H_0^\alpha(\Omega)} \leq 1, i = 1, 2, \\ \text{for some } p \} \quad (1.15)$$

where Ω represents the bounded domain of f .

The lower bound of r is shown to be given by,

$$r(\alpha, n, \epsilon) \geq (C(\alpha, \Omega)) (n^{-\alpha/2} + \epsilon^{\alpha/(\alpha+1/2)}) \quad (1.16)$$

Here the projection data p consists of n line integrals with a root mean square error ϵ , and C is a constant.

\tilde{R}_f represents the true projection data for the function f .

1.3 Some Non-Medical Applications of CT

The most extensive use of CT scanners has been in the medical diagnostics area where CT images are instrumental in detecting cancerous tissues at a very early stage. The tremendous impact of CT in this area is evident by the awarding of the Nobel Prize (for the year 1979) to Hounsfield [11] and Cormack [12]. The Journal of Computerized Tomography is exclusively devoted to the medical imaging aspect of CT.

CT has been used in a completely different context by Kershaw [13], and more recently by Munshi [14] for determining densities in fluid-flows. The results of reconstructions (using CBP algorithms) for two-phase air-water flows have been reported by Kulacki et al [15], De Vuono et al [16], Schlosser et al [17], Seshadri et al [18] and Munshi et al [19]. Recently, tomographic algorithms suited for radially symmetric flow distributions have been developed by Rathore et al [20,21,22].

As mentioned in the earlier section, CT is being used in the nuclear industry for the non-destructive testing (NDT) of damaged nuclear fuel bundles [23] at the Argonne National Laboratory in Idaho Falls, USA. In Japan, the Toshiba TOSCANNER 4200 [24] is being used for detecting cracks in steel pipes. Inspection of wooden

poles (for power transmission) using a portable CT-scanner has also been reported [25] in the United States. Recently, CT has been applied in West Germany to assess the quality of meat, thus making it possible to examine the meat before slaughtering animals [26] .

CHAPTER 2

PRELIMINARIES

2.1 The CBP Algorithm

A digital implementation of the CBP algorithm is required to reconstruct real-life objects of interest. Following Lewitt [27] , the discrete implementation of Eq. (1.9b) leads to the following equation:

$$\tilde{f}(k\Delta x, l\Delta y) \simeq \Delta\theta \sum_{n=1}^N \tilde{p}(k\Delta x \cos\theta_n + l\Delta y \sin\theta_n, \theta_n) \quad (2.1)$$

where for KxL digitized image,

$$K^- \leq k \leq K^+ \text{ and } L^- \leq l \leq L^+ .$$

Here,

$$s' = k\Delta x \cos\theta_n + l\Delta y \sin\theta_n .$$

The evaluation of $\tilde{p}(s', \theta_n)$ has to be done for all KxL values of s' . For large ray-numbers, a practical approach is to calculate $\tilde{p}(m\Delta s, \theta_n)$ for $M^- \leq m \leq M^+$ and then use inexpensive interpolation to estimate the required KxL values of \tilde{p} from only M calculated values of the function. Thus the convolutions in Eq. (2.1) are computed by two operations: a discrete convolution, \tilde{p}_c , followed by an

interpolation operation resulting in the \tilde{p} values, \tilde{p}_I , at desired values, s' . The following equations represent the convolution-interpolation operations:

$$\tilde{p}_C(m' \Delta s, \theta_n) = \Delta s \sum_{m=M^-}^{M^+} p(m \Delta s, \theta_n) q((m' - m) \Delta s),$$

$$M^- \leq m' \leq M^+ \quad (2.2)$$

$$\tilde{p}_I(s', \theta_n) = \Delta s \sum_{m'} \tilde{p}_C(m' \Delta s, \theta_n) I(s' - m' \Delta s) \quad (2.3)$$

Here $I(s)$ is an interpolating function and the number of terms in the summation depends on the width of the non-zero part of $I(s)$. Two popular schemes used are, nearest neighbour interpolation and linear interpolation. Both of these give satisfactory results depending upon the information the user wants to obtain about the image [1].

The convolving function, $q(s)$, is evaluated once and stored for repeated use for different views. Some commonly used window functions are given in Table (2.1).

The discrete implementation of the tomographic inversion formula using the CBP algorithm, leads to the following errors in the reconstruction process:

- (i) The inherent error, e_R , at a point (r, ϕ) , is given by the difference of $f(r, \phi)$ and its approximation $\tilde{f}(r, \phi)$ as expressed in Eqs.(1.9) and (1.9a) respectively. This error is strictly

Table 2.1 : Some Commonly Used Window Functions

Window Name	$W(R)$
Band limited	1
Sinc	$(\text{Sin } (\pi R/2R_c))/(\pi R/2R_c)$
Cosine	$\text{Cos } (\pi R/2R_c)$
Generalized Hamming	$\alpha + (1-\alpha) \text{Cos } (\pi R/R_c)$
$0.5 \leq \alpha \leq 1.0$	

due to the finite cut-off, R_c of the Fourier frequency. We note that e_R is precisely zero if the function, $f(r, \phi)$, happens to have a band-limited projection data and R_c is chosen such that it is atleast equal to the largest frequency contained in f and $W(R) = 1$ in $[-R_c, R_c]$.

- (ii) The error, e_C , arising due to the discrete implementation of the convolution integral.
- (iii) The error, e_B , due to the discretization of the backprojection integral.

If the cut-off frequency, R_c , is related to the ray-spacing of the data, then the errors e_R and e_C will be coupled. The total error in the reconstruction, e_T , at any point is a combination of the above listed errors, e_R , e_C and e_B , at that point, i.e.,

$$e_T = e_R + e_B + e_C .$$

2.2 The Window Functions

The window functions that have been considered in this study are of the form,

$$W_A(R) = W(R/A)$$

where, W is a fixed window and A is a positive real parameter related to the cut-off frequency, R_c , in a

practical implementation. In fact, for this study A will be used interchangeably with R_c .

Let,

$$K(x,y) = \int_{-\infty}^{\infty} \int_{-\infty}^{\infty} W(R) e^{2\pi i(xX + yY)} dx dy \quad (2.4)$$

then,

$$W(R) = \int_{-\infty}^{\infty} \int_{-\infty}^{\infty} K(x,y) e^{-2\pi i(xX + yY)} dx dy \quad (2.5)$$

where

$$R = \{x^2 + y^2\}^{1/2}$$

If (r, ϕ) denote the polar co-ordinates of the point (x, y) , then,

$$K(r \cos \phi, r \sin \phi) = \int_0^{\pi} \int_{-\infty}^{\infty} W(R) e^{2\pi i R r \cos(\theta - \phi)} |R| dR d\theta \quad (2.6)$$

where,

$$\theta = \tan^{-1} (Y/X).$$

Using (2.6) in Eq.(1.10) we get

$$K(r \cos \phi, r \sin \phi) = \int_0^{\pi} q(r \cos(\theta - \phi)) d\theta. \quad (2.7)$$

we know that $W(R)$ is a radially symmetric function. FT of a radially-symmetric function is also radially symmetric. This implies that $K(r \cos\phi, r \sin\phi)$ is radially symmetric. Therefore, without loss of generality, for $\phi = 0$, Eq. (2.7) reduces to,

$$\begin{aligned} K(r) &= \int_0^{\pi} q(r \cos\theta) d\theta \\ &= (W)^V(r), \end{aligned} \quad (2.8)$$

i.e., K now represents a function of just one variable, r , and K is the inverse Fourier transform (FT) of W .

Writing, $K_A(r) = (W_A)^V(r)$, we have,

$$K_A(r) = A^2 K(Ar) \quad (2.9)$$

Again writing,

$$q_A(s) = \int_{-\infty}^{\infty} |R| W_A(R) e^{i2\pi Rs} ds$$

we have,

$$\begin{aligned} q_A(s) &= A^2 \int_{-\infty}^{\infty} |R| W(R) e^{i2\pi Rs} ds \\ &= A^2 q(As) \end{aligned} \quad (2.10)$$

Eq. (2.10) represents a family of convolving functions for evaluating $\tilde{f}(x,y)$ by the CBP method.

Summarizing, we have,

$$\begin{aligned}\tilde{f}(x,y) &= (\hat{p} \hat{w})^v(x,y) \\ &= (\hat{f} \hat{K})^v(x,y) \\ &= (f * K)(x,y)\end{aligned}$$

and with K replaced by K_A ,

$$f_A(x,y) = (f * K_A)(x,y) \quad (2.11)$$

Eq. (2.11) results in various approximations of the function, f , depending upon the function K and the parameter A .

2.3 Some Definitions

Let X denote a point in the plane \mathbb{R}^2 . The following alternate representations for X are also used:

- (i) (x,y) ,
 - (ii) $(x + iy)$,
 - (iii) $r e^{i\phi}$, $r = \{x^2 + y^2\}^{1/2}$,
- $$\phi = \tan^{-1}(y/x).$$

Expressions like $X + \rho e^{i\phi}$ would have their obvious meaning of representing the point $(x + \rho \cos \phi, y + \rho \sin \phi)$.

For a real valued f defined on \mathbb{R}^2 and for,
 $r \in [0, \infty)$, $\phi \in [0, 2\pi]$, $X \in \mathbb{R}^2$, we write,

$$f_{r,\phi}(X) = f(X + r e^{i\phi}) .$$

Taking average over ϕ , we get

$$f_{r,\bar{\phi}}(X) = \frac{1}{2\pi} \int_0^{2\pi} f_{r,\phi}(X) d\phi,$$

provided $f_{r,\phi}(X)$ is integrable w.r.t. ϕ . Further, we define,

$$D_{r,\bar{\phi}}^k f(X) = \frac{\partial^k}{\partial r^k} f_{r,\bar{\phi}}(X)$$

for $r \geq 0$, $X \in \mathbb{R}^2$, and $k = 0, 1, 2, \dots$

and, in particular,

$$D_{0,\bar{\phi}}^k f(X) = D_{r,\bar{\phi}}^k f(X) \Big|_{r=0}$$

2.3.1 The Space Ω_{2m}

We define Ω_{2m} to be the class of all real-valued functions f , bounded and continuous on \mathbb{R}^2 , for which $f_{r,\bar{\phi}}(X)$ is a $2m$ times continuously differentiable function of $r \in [0, \infty)$, with $D_{r,\bar{\phi}}^k f(X)$, a bounded and continuous function of (r, X) , for $k = 1, 2, \dots, 2m$. Clearly Ω_{2m} is a vector space over \mathbb{R} .

The functional,

$$||f||_{2m} = ||f||_c + ||D_{r,\bar{\phi}}^{2m} f(X)||_c$$

is obviously a norm on Ω_{2m} . Here,

$$||f||_c = \sup_{X \in \mathbb{R}^2} |f(X)|$$

and,

$$||D_{r,\bar{\phi}}^{2m} f(X)||_c = \sup_{\substack{X \in \mathbb{R}^2 \\ r \in [0, \infty)}} |D_{r,\bar{\phi}}^{2m} f(X)|$$

2.3.2 The Space Ω_0

The space Ω_0 consists of all bounded and continuous functions in \mathbb{R}^2 with the norm defined by,

$$||f||_0 = ||f||_c .$$

2.3.3 The Space IK_{2m}

We define IK_{2m} as the class of all radially symmetric functions $K(r)$ with the constraints,

$$(i) \quad 2\pi \int_0^\infty K(r) r dr = 1,$$

$$(ii) \quad 2\pi \int_0^{\infty} K(r) r^{2m+1} dr = A_{2m} \neq 0,$$

$$(iii) \quad \int_0^{\infty} K(r) r^{2k+1} dr = 0, \text{ for } k = 1, 2, \dots, (m-1),$$

and such that

$$K(x, y) = K(\sqrt{x^2 + y^2}) \in \Omega_{2m}.$$

Here m is a positive integer.

2.3.4 The Interpolation Space Ω_{2m}^{β}

The space Ω_{2m}^{β} is defined as the intermediate space consisting of functions $f \in \Omega_0$ for which $t^{-\beta} K_P(t^{2m}; f)$ is a bounded function of t , and $0 < \beta < 2m$. Here, K_P is the Peetre's functional for the pair (Ω_0, Ω_{2m}) , defined by,

$$K_P(t^{2m}; f) = \inf_{g \in \Omega_{2m}} \{ \|f - g\|_0 + t^{2m} \|g\|_{2m} \}.$$

2.4 Theorem

$\{\Omega_{2m}, \|\cdot\|_{2m}\}$ is a Banach space.

Proof

Let $\{f_n\}$ be Cauchy in $\{\Omega_{2m}, \|\cdot\|_{2m}\}$. Since the spaces of bounded and continuous functions over \mathbb{R}^2 and $\mathbb{R}^+ \times \mathbb{R}^2$ are complete, where $\mathbb{R}^+ \Rightarrow r \in [0, \infty)$, it follows that there exists a function f continuous and bounded on \mathbb{R}^2

and a function $g^{2m}(r, X)$, bounded and continuous on $\mathbb{R}^+ \times \mathbb{R}^2$ such that

$$\|f_n - f\|_C \rightarrow 0, \quad n \rightarrow \infty$$

and

$$\|D_{r, \bar{\phi}}^{2m} f_n(X) - g^{2m}(r, X)\|_C \rightarrow 0, \quad n \rightarrow \infty.$$

Using a well-known remainder form,

$$\begin{aligned} (f_n)_{r, \bar{\phi}}(X) &= f_n(X) + \sum_{j=1}^{2m} \frac{r^j}{j!} D_{o, \bar{\phi}}^j f_n(X) \\ &\quad + \frac{1}{(2m-1)!} \int_0^r [D_{s, \bar{\phi}}^{2m} f_n(X) - D_{o, \bar{\phi}}^{2m} f_n(X)] (r-s)^{2m-1} ds \end{aligned}$$

we have, taking limit as $n \rightarrow \infty$

$$\begin{aligned} f_{r, \bar{\phi}}(X) &= f(X) + \sum_{j=1}^{2m} \frac{r^j}{j!} g^j(0, X) \\ &\quad + \frac{1}{(2m-1)!} \int_0^r [g^{2m}(s, X) - g^{2m}(0, X)] (r-s)^{2m-1} ds \end{aligned} \quad (2.4)$$

where, for, $j = 1, 2, \dots, (2m-1)$

$$g^j(r, X) = \lim_{n \rightarrow \infty} D_{r, \bar{\phi}}^j f_n(X).$$

We note that the limit exists because of the well-known interpolation inequalities [28] and that the functions $g^j(r, X)$ defined thus are continuous and bounded function on $\mathbb{R}^+ \times \mathbb{R}^2$.

It follows from Eq. (2.4) that $f_{r, \bar{\phi}}(X)$ is $2m$ -times continuously differentiable function of $r \in [0, \infty)$ for each $X \in \mathbb{R}^2$. Furthermore,

$$\begin{aligned} D_{r, \bar{\phi}}^k f(X) &= g^k(0, X) + \sum_{j=1}^{2m-k} \frac{r^j}{j!} g^{k+j}(0, X) \\ &+ \frac{1}{(2m-k-1)!} \int_0^r [g^{2m}(r, X) - g^{2m}(0, X)] (r-s)^{2m-k-1} ds \end{aligned}$$

which shows that $D_{r, \bar{\phi}}^k f(X)$ are continuous functions on $\mathbb{R}^+ \times \mathbb{R}^2$, for $k = 1, 2, \dots, (2m-1)$. Since, again from Eq. (2.4)

$$D_{r, \bar{\phi}}^{2m} f(X) = g^{2m}(r, X)$$

it follows that $D_{r, \bar{\phi}}^{2m} f(X)$ is bounded, and continuous on $\mathbb{R}^+ \times \mathbb{R}^2$. This fact, in view of the boundedness of f , implies that $D_{r, \bar{\phi}}^j f(X)$, for $j = 1, 2, \dots, (2m-1)$ are bounded and continuous functions on $\mathbb{R}^+ \times \mathbb{R}^2$.

Hence $f \in \Omega_{2m}$. Finally, as,

$$\|f_n - f\|_{2m} = \|f_n - f\|_C + \|D_{r, \bar{\phi}}^{2m} f_n - g^{2m}(r, X)\|_C \rightarrow 0$$

as $n \rightarrow \infty$, the completeness of Ω_{2m} follows.

CHAPTER 3

DIRECT THEOREMS

The subject matter in this chapter deals with some direct estimates of error in reconstruction by the CBP method discussed in Section 2.1. The theorems developed here use certain derivatives and moduli of continuity of the object-function cross section. The estimates deal with the e_R -error.

3.1 Definitions

If we define,

$$D_{r, \phi}^k f(X) = \frac{\partial^k}{\partial r^k} f(X + r e^{i\phi}), \quad k = 0, 1, 2, \dots,$$

then whenever the order of differentiation and integration can be interchanged, we have,

$$D_{r, \bar{\phi}}^k f(X) = \frac{1}{2\pi} \int_0^{2\pi} D_{r, \phi}^k f(X) d\phi.$$

We now define a k -th modulus of continuity appropriate for error analysis of CBP, by,

$$\omega_c(f^{[k]}; \delta) = \sup_{\substack{0 < |h_1 - h_2| \leq \delta \\ X \in \mathbb{R}^2}} | D_{h_1, \bar{\phi}}^k f(X) - D_{h_2, \bar{\phi}}^k f(X) |$$

3.2 Lemmas

The following four lemmas are needed for establishing the direct theorems:

Lemma 3.2.1

$$\lim_{\delta \rightarrow 0} \omega_c (f^{[k]}; \delta) = 0 \quad (3.2.1)$$

if and only if

$$\lim_{|h_1 - h_2| \rightarrow 0} D_{h_1, \Phi}^k f(X) = D_{h_2, \Phi}^k f(X),$$

uniformly for all $X \in \mathbb{R}^2$.

The result (3.2.1) follows easily from the definition of $\omega_c (f^{[k]}; \delta)$.

Similarly we have,

Lemma 3.2.2

If $\delta_1 \leq \delta_2$, then,

$$\omega_c (f^{[k]}; \delta_1) \leq \omega_c (f^{[k]}; \delta_2) \quad (3.2.2)$$

Lemma 3.2.3

For any $\lambda, \delta > 0$

$$\omega_c (f^{[k]}; \lambda \delta) \leq (1+\lambda) \omega_c (f^{[k]}; \delta) \quad (3.2.3)$$

Proof

By Lemma (3.2.2) we have, with $h = |h_1 - h_2|$

$$\omega_c(f^{[k]}; \lambda \delta) \leq \omega_c(f^{[k]}; (1 + [\lambda]) \delta)$$

$$= \sup_{\substack{0 < h \leq (1 + [\lambda]) \delta \\ X \in \mathbb{R}^2 \\ h_1, h_2 \in \mathbb{R}^+}} |D_{h_1, \bar{\phi}}^k f(X) - D_{h_2, \bar{\phi}}^k f(X)|$$

$$\begin{aligned} &= \sup_{\substack{0 < h \leq (1 + [\lambda]) \delta \\ X \in \mathbb{R}^2, h_2 \in \mathbb{R}^+}} |D_{h_2+h, \bar{\phi}}^k f(X) - D_{h_2, \bar{\phi}}^k f(X)| \\ &\leq \sum_{j=1}^{1 + [\lambda]} \sup_{\substack{0 < h \leq \delta \\ h_2 + (j-1)h, h_2 \in \mathbb{R}^+ \\ X \in \mathbb{R}^2}} |D_{h_2+jh, \bar{\phi}}^k f(X) - D_{h_2+(j-1)h, \bar{\phi}}^k f(X)| \end{aligned}$$

$$= (1 + [\lambda]) \omega_c(f^{[k]}; \delta)$$

$$\leq (1 + \lambda) \omega_c(f^{[k]}; \delta),$$

completing this proof.

Lemma 3.2.4

The integral-type remainder in the Taylor's expansion is given by,

$$\begin{aligned}
f_{r,\bar{\phi}}(X) &= \sum_{j=0}^k \frac{r^j}{j!} D_{0,\bar{\phi}}^j f(X) \\
&= \frac{1}{(k-1)!} \int_0^r \{D_{s,\bar{\phi}}^k f(X) - D_{0,\bar{\phi}}^k f(X)\} (r-s)^{k-1} ds
\end{aligned}$$

3.3 The ω_c - Estimate

For a cross-section distribution $f(X)$ for which,

$$\omega_c(f^{[k]}; \delta) \rightarrow 0, \text{ as } \delta \rightarrow 0,$$

for some $k = 0, 1, 2, \dots, (2m-1)$, an error estimate for the CBP method is given by the following theorem:

Theorem

Let the CBP window, K belong to \mathbb{TK}_{2m} . Then for, $k = 0, 1, 2, \dots, (2m-1)$, the following holds:

$$\|f_A - f\|_c \leq \frac{B}{A^k} \omega_c(f^{[k]}; \frac{1}{A})$$

where, B is a positive constant independent of f or A and is given by,

$$B = \frac{2\pi}{k!} \int_0^\infty (\rho^{k+2} + \rho^{k+1}) |K(\rho)| d\rho.$$

Proof

Using lemma (3.2.4) we have,

$$\begin{aligned}
 f_A(X) - f(X) &= \int_0^{2\pi} \int_0^\infty [f(X - \frac{\rho}{A} e^{i\phi}) - f(X)] K(\rho) \rho \, d\rho d\phi \\
 &= 2\pi \sum_{j=1}^k \frac{D_{0,\bar{\phi}}^j f(X)}{A^j j!} \int_0^\infty \rho^{j+1} K(\rho) \, d\rho \\
 &\quad + \frac{2\pi}{(k-1)!} \int_0^\infty \int_0^{\rho/A} \{D_{s,\bar{\phi}}^k f(X) - D_{0,\bar{\phi}}^k f(X)\} (\frac{\rho}{A} - s)^{k-1} \\
 &\quad \quad \quad K(\rho) \rho \, ds \, d\rho
 \end{aligned}$$

Note that $D_{0,\bar{\phi}}^j f(X)$ is zero for j odd.

Hence, using the fact that $K \in \mathcal{IK}_{2\pi}$, we have,

$$\begin{aligned}
 |f_A(X) - f(X)| &\leq \frac{2\pi}{(k-1)!} \int_0^\infty \omega_c(f^{[k]}; \frac{\rho}{A}) \frac{\rho^{k+1}}{kA^k} |K(\rho)| \, d\rho \\
 &\leq \frac{2\pi}{k!A^k} \omega_c(f^{[k]}; \frac{1}{A}) \int_0^\infty (1+\rho) \rho^{k+1} |K(\rho)| \, d\rho
 \end{aligned}$$

from which the result follows.

This theorem relates the error, e_R , to the local smoothness properties of the function. Existence of a high order ω_c , i.e., k large, implies relatively low error due to the factor A^k in the denominator.

3.4 The Asymptotic Formula

The following result gives a precise pointwise estimate of error, e_R , in the CBP method for cross-sectional distributions which are sufficiently smooth at points under consideration.

Theorem

Let $K \in IK_{2m}$ and $f \in \Omega_0$. If $D_{0,\bar{\phi}}^{2m} f(X)$ exists at a point $X \in \mathbb{R}^2$, then, there holds the following asymptotic formula:

$$\lim_{A \rightarrow \infty} A^{2m} \{f_A(X) - f(X)\} = \frac{B_{2m}}{(2m)!} D_{0,\bar{\phi}}^{2m} f(X)$$

where,

$$B_{2m} = 2\pi \int_0^\infty K(\rho) \rho^{2m+1} d\rho$$

Proof

Since $f_{0,\bar{\phi}}^{(2m)}(X)$ exists, the Taylor's expansion of $f_{\rho,\bar{\phi}}(X)$ about $\rho = 0$ can be written as,

$$f_{\rho,\bar{\phi}}(X) = \sum_{j=0}^{2m} \frac{\rho^j}{j!} D_{0,\bar{\phi}}^j f(X) + \rho^{2m} g_X(\rho), \quad (3.4)$$

where, $g_X(\rho) \rightarrow 0$, as, $\rho \rightarrow 0$.

We note that the function,

$$g_X(\rho) = \{f_{\rho,\bar{\phi}}(X) - \sum_{j=0}^{2m} \frac{\rho^j}{j!} D_{0,\bar{\phi}}^j f(X)\} / \rho^{2m}$$

is bounded as $\rho \rightarrow 0, \infty$ and hence by its continuity for

$\rho \in (0, \infty)$, it follows that $g_X(\rho)$ is a bounded function of $\rho \in (0, \infty)$. We denote the bound by M_1 .

Now, multiplying Eq. (3.4) by $2\pi A^2 K(A\rho)\rho$ and integrating w.r.t. ρ , we get

$$f_A(X) - f(X) = \sum_{j=1}^{2m} \frac{2\pi D^j}{0, \bar{\phi}} \frac{f(X)}{j!} \int_0^\infty \rho^{j+1} A^2 K(A\rho) d\rho \\ + 2\pi \int_0^\infty g_X(\rho) \rho^{2m+1} A^2 K(A\rho) d\rho.$$

Using the property, $K \in \mathcal{TK}_{2m}$, we have

$$f_A(X) - f(X) = \frac{B_{2m}}{(2m)!} \frac{D^{2m}}{0, \bar{\phi}} \frac{f(X)}{A^{2m}} + \frac{2\pi}{A^{2m}} \int_0^\infty g_X(\rho/A) \rho^{2m+1} K(\rho) d\rho,$$

$$\text{where, } B_{2m} = 2\pi \int_0^\infty K(\rho) \rho^{2m+1} d\rho.$$

We note that,

- (i) $h_A(\rho) = |g_X(\rho/A) \rho^{2m+1} K(\rho)|$, is bounded by the integrable function $M_1 \rho^{2m+1} |K(\rho)|$, and,
- (ii) $g_A(\rho) \rightarrow 0$, as $\rho \rightarrow 0$, which implies that, $h_A(\rho) \rightarrow 0$ as $A \rightarrow \infty$, for every fixed $\rho \in (0, \infty)$.

Now (i) and (ii) imply the applicability of the Lebesgue dominated convergence theorem [29], and we have,

$$\lim_{A \rightarrow \infty} 2\pi \int_0^{\infty} g_A(\rho/A) \rho^{2m+1} K(\rho) d\rho = 0,$$

and the result follows.

For the special case, $K \in K_2$, i.e., $m = 1$, we have,

$$B_2 = 2\pi \int_0^{\infty} K(\rho) \rho^3 d\rho.$$

Now by Eq. (2.8),

$$W(R) = \int_0^{2\pi} \int_0^{\infty} K(r) e^{-i\pi Rr \cos(\theta-\phi)} r dr d\phi.$$

Since $W(R)$ is radially symmetric, substituting $\theta = 0$, without loss of generality, we get,

$$W(R) = \int_0^{2\pi} \int_0^{\infty} K(r) e^{-i2\pi Rr \cos\phi} r dr d\phi.$$

Differentiating twice, we obtain,

$$W''(R) = \int_0^{2\pi} \int_0^{\infty} (i2\pi)^2 (K(r)) (r \cos\phi)^2 e^{-i2\pi Rr \cos\phi} r dr d\phi$$

$$\Rightarrow W''(0) = (-4\pi^2) \int_0^{2\pi} \int_0^{\infty} r^3 K(r) dr \cos^2\phi d\phi$$

$$= -4\pi^2 \int_0^{\infty} r^3 K(r) dr$$

Thus,

$$B_2 = - \frac{W''(0)}{2\pi^2}$$

Similarly for higher order cases, $2m$, the error, e_R , will depend on the $2m$ -th derivative of $W(R)$ provided the object-function cross section is sufficiently smooth.

3.5 The $\|f\|_{2m}$ - Estimate

Let, $f \in \Omega_{2m}$, $K(X)$ be radially symmetric,

$$\int_0^{\infty} r^{2j+1} K(r) dr = 0, \text{ for } j = 0, 1, 2, \dots, (m-1),$$

and, $r^{2m+1} K(r) \in L^1 [0, \infty)$.

Then, if

$$\begin{aligned} 2\pi \int_0^{\infty} K(r) r dr &= 1, \\ \|f_A - f\|_0 &\leq \frac{M_2}{A^{2m}} \|f\|_{2m}, \end{aligned}$$

where M_2 is a constant independent of A and f .

Proof

$$\begin{aligned} &|f_A(X) - f(X)| \\ &= \left| 2\pi \int_0^{\infty} \int_0^{2\pi} \left\{ f\left(X - \frac{r}{A} e^{i\phi}\right) - f(X) \right\} K(r) r dr d\phi \right| \\ &= \left| 2\pi \int_0^{\infty} \left\{ f_{r/A, \bar{\phi}}(X) - f(X) \right\} K(r) r dr \right| \end{aligned}$$

$$= \left| 2\pi \int_0^\infty \frac{1}{j!} \sum_{j=1}^{2m-1} \left(\frac{r}{A}\right)^j D_{0,\bar{\phi}}^j f(X) + \frac{1}{2m!} \left(\frac{r}{A}\right)^{2m} D_{(\alpha r/A),\bar{\phi}}^{2m} f(X) \right\} r K(r) dr$$

$$\leq \frac{2\pi}{2m!} \|D_{r,\bar{\phi}}^{2m} f\|_0 A^{-2m} \int_0^\infty r^{2m+1} |K(r)| dr$$

$$\leq \frac{M_2}{A^{2m}} \|f\|_{2m}$$

where, $M_2 = \frac{2\pi}{2m!} \int_0^\infty r^{2m+1} |K(r)| r dr$, and, $0 < \alpha < 1$.

We note that this estimate is applicable for functions which are sufficiently smooth, i.e., belonging to the class Ω_{2m} .

3.6 Localization Lemma

Let $K_1, K_2 \in \mathbb{IK}_{2m}$ and $f \in \Omega_0$. If for some $\delta > 0$,

$$K_1(r) = K_2(r), \text{ for } 0 \leq r \leq \delta,$$

then,

$$\| (f_A)_1 - (f_A)_2 \|_0 \leq \frac{M_3}{A^{2m}} \|f\|_0,$$

where the constant M_3 does not depend on A or f and $(f_A)_i$ denotes the CBP approximation w.r.t. the function K_i .

Proof

$$| (f_A)_1(x) - (f_A)_2(x) |$$

$$\leq \int_0^\infty \int_0^{2\pi} |f(x - \frac{re^{i\phi}}{A})| |K_1(r) - K_2(r)| r dr d\phi$$

$$\leq 2\pi \int_{A\delta}^\infty |f_{r,\phi}(x)| (|K_1(rA)| + |K_2(rA)|) A^2 r dr$$

$$\leq \frac{2\pi}{(A\delta)^{2m}} ||f||_0 \int_0^\infty r^{2m+1} (|K_1(r)| + |K_2(r)|) dr$$

$$\leq \frac{2\pi (M_4 + M_5)}{(A\delta)^{2m}} ||f||_0$$

$$\text{where, } M_{i+3} = \int_0^\infty r^{2m+1} |K_i(r)| dr < \infty, \quad i = 1, 2.$$

Now, the result holds for,

$$M_3 = \frac{2\pi (M_4 + M_5)}{\delta^{2m}}.$$

The localization lemma effectively states that for A sufficiently large, the performance of the window function/convolving function depends on the values of K in the neighbourhood of origin only.

CHAPTER 4

INVERSE THEOREM

We now establish some inverse results for the CBP method. The result states that the inherent error, e_R , is $O(A^{-\beta})$, $0 < \beta < 2m$, if and only if the function under consideration belongs to the class Ω_{2m}^{β} defined earlier in Section 2.4. This theorem guarantees the error order for a given A (or R_c), the Fourier cut-off frequency, provided images can be thought of being represented by functions belonging to Ω_{2m}^{β} . We note that a higher value of β represents a relatively smoother image.

We first discuss some lemmas required for the proof of the main result.

4.1 Lemmas

The five lemmas concern with the smoothness of f_A and the bounds for the various norms of f_A .

4.1.1 Lemma

If, $K \in TK_{2m}$, and $f \in \Omega_0$ has a compact support, then,

$$f_A \in \Omega_{2m}$$

for each $A > 0$.

Proof

Since, f has a compact support, the integral,

$$f_A(X) = \int_0^{2\pi} \int_0^{\infty} f(\rho e^{i\alpha}) A^2 K(A(X - \rho e^{i\alpha})) \rho d\rho d\alpha$$

exists, and is a bounded and continuous function of $X \in \mathbb{R}^2$. Now using Fubini's theorem,

$$\begin{aligned} (f_A)_{r, \bar{\phi}}(X) &= \frac{1}{2\pi} \int_0^{2\pi} f_A(X + r e^{i\phi}) d\phi \\ &= \int_0^{2\pi} \int_0^{\infty} f(\rho e^{i\alpha}) \left(\frac{1}{2\pi} \int_0^{2\pi} A^2 K(A(X - \rho e^{i\alpha} + r e^{i\phi})) d\phi \right) d\rho d\alpha \\ &= \int_0^{2\pi} \int_0^{\infty} f(\rho e^{i\alpha}) (K_A)_{r, \bar{\phi}}(X - \rho e^{i\alpha}) \rho d\rho d\alpha \\ &= \int_0^{2\pi} \int_0^{\infty} f(\rho e^{i\alpha}) A^2 K_{Ar, \bar{\phi}}(A(X - \rho e^{i\alpha})) \rho d\rho d\alpha. \end{aligned}$$

Now, using compactness of f , it follows that the integration region is compact, say the disk $D(0, \rho_0)$, and then, since $D_{r, \bar{\phi}}^{2m} K_{Ar}(X)$ is continuous for all $r \in X$, it follows [30] that,

$$\frac{\partial^{2m}}{\partial r^{2m}} (f_A)_{r, \bar{\phi}}(X) = \int_0^{\infty} \int_0^{2\pi} f(\rho e^{i\alpha}) A^2 \frac{\partial^{2m}}{\partial r^{2m}} K_{Ar, \bar{\phi}}(A(X - \rho e^{i\alpha})) \rho d\rho d\alpha$$

and, since the integrand in the above expression is continuous w.r.t. $r, X, \rho e^{i\alpha}$, for each fixed A , it follows, using compactness of the support of f , that the integral is a continuous function of r and X , i.e.,

$D_{r, \bar{\phi}}^{2m} f_A(X)$ is a continuous function of r, X , where $r \in \mathbb{R}^+$, and $X \in \mathbb{R}^2$. The boundedness of $D_{r, \bar{\phi}}^{2m} f_A(X)$ follows from the boundedness of $D_{r, \bar{\phi}}^{2m} K(X)$ w.r.t. r and X and a bound is given by,

$$A^{2m+2} B_K \pi \rho_0^2 ||f||_0$$

where,

$$B_K = \sup_{\substack{r \in \mathbb{R}^+ \\ X \in \mathbb{R}^2}} |D_{r, \bar{\phi}}^{2m} K(X)|.$$

Thus,

$$f_A \in \Omega_{2m}, \text{ completing the proof.}$$

4.1.2 Lemma

Let, K be radially symmetric,

$$K \in \Omega_{2m} \cap L^1(\mathbb{R}^2)$$

$$D_{r, \bar{\phi}}^{2m} K \in S, \text{ a bounded set in } L^1(\mathbb{R}^2), \text{ for } r \in \mathbb{R}^+,$$

Then if $f \in \Omega_0$,

$$f_A \in \Omega_{2m}.$$

Proof

We have,

$$f_A(X) = \int_{\mathbb{R}^2} f\left(X - \frac{T}{A}\right) K(T) \, dT.$$

Hence,

$$\begin{aligned} |f_A(X)| &\leq \int_{\mathbb{R}^2} \left|f\left(X - \frac{T}{A}\right)\right| |K(T)| \, dT \\ &\leq \|f\|_0 \int_{\mathbb{R}^2} |K(T)| \, dT \\ &= M_6 \|f\|_0 \end{aligned}$$

where, $M_6 < \infty$ because $K(T) \in L^1(\mathbb{R}^2)$. Hence f_A is bounded with

$$\|f_A\|_0 \leq M_6 \|f\|_0.$$

Now we prove the continuity of f_A .

We have,

$$|f_A(X) - f_A(X_0)| \leq \int_{\mathbb{R}^2} \left|f\left(X - \frac{T}{A}\right) - f\left(X_0 - \frac{T}{A}\right)\right| |K(T)| \, dT.$$

(4.1.2)

Now, for every T ,

$$\left|f\left(X - \frac{T}{A}\right) - f\left(X_0 - \frac{T}{A}\right)\right| |K(T)| \rightarrow 0$$

as, $X \rightarrow X_0$.

Moreover, this integrand is bounded by,

$$2 \|f\|_0 |K(T)| \in L^1(\mathbb{R}^2).$$

Hence, by Lebesgue's dominated convergence theorem, the r.h.s. of Eq.(4.1.2) $\rightarrow 0$, as $X \rightarrow X_0$. This means that,

$$\lim_{X \rightarrow X_0} f_A(X) = f_A(X_0),$$

i.e., $f_A(X)$ is continuous at $X=X_0$. Since, X_0 is arbitrary, $f_A(X)$ is a continuous function of X .

We can write

$$(f_A)_{r, \bar{\phi}}(X) = \int_{\mathbb{R}^2} f(T) A^2 K_{Ar, \bar{\phi}}(A(X-T)) dT.$$

Since, $f \in \Omega_0$, and $D_{r, \bar{\phi}}^{2m} K \in S \subset L^1(\mathbb{R}^2)$, the functions,

$$\frac{\partial^k}{\partial r^k} (f_A)_{r, \bar{\phi}}(X), \quad k = 0, 1, 2, \dots (2m)$$

exist and are bounded and continuous functions on $(r, X) \in (\mathbb{R}^+ \times \mathbb{R}^2)$ and

$$\frac{\partial^k}{\partial r^k} (f_A)_{r, \bar{\phi}}(X) = \int_{\mathbb{R}^2} f(T) A^2 \frac{\partial^k}{\partial r^k} K_{Ar, \bar{\phi}}(A(X-T)) dT.$$

We note that for the integrability of the intermediate derivatives, $D^{k_{r,\bar{\phi}}}$ K , we use the interpolation inequalities [28].

4.1.3 Lemma

Let $f \in \Omega_0$,

$$K \in L^1(\mathbb{R}^2).$$

Then there exists a constant M_7 , independent of f , such that,

$$\|f_A\|_0 \leq M_7 \|f\|_0.$$

The fact $f_A \in \Omega_0$ is a part of the conclusion.

Proof

We know that,

$$(i) \quad f_A(X) = \int_{\mathbb{R}^2} f(X-T) A^2 K(AT) dT.$$

(ii) f is bounded and continuous, and

(iii) $K \in L^1(\mathbb{R}^2)$.

This implies that $f_A(X)$ exists for every X . Moreover,

$$|f_A(Y) - f_A(X)| \leq \int_{\mathbb{R}^2} |f(Y - \frac{T}{A}) - f(X - \frac{T}{A})| |K(T)| dT.$$

As, $Y \rightarrow X$, the integrand approaches zero for every T .

Since the integrand is dominated by,

$$2 \|f\|_0 |K(T)|,$$

which is integrable, (by Lebesgue's Dominated Convergence Theorem), we have,

$$\lim_{Y \rightarrow X} f_A(Y) = f_A(X).$$

Hence $f_A(X)$ is a continuous function of X . Finally, as

$$|f_A(X)| \leq \|f\|_0 \int_{\mathbb{R}^2} |K(T)| dT,$$

we have,

$$\|f_A\|_0 \leq M_7 \|f\|_0$$

$$\text{where, } M_7 = \int_{\mathbb{R}^2} |K(T)| dT.$$

Thus, we have shown that f_A is bounded and continuous function of X , i.e.,

$$f_A \in \Omega_0.$$

This completes the proof.

4.1.4 Lemma

Let, $f \in \Omega_0$, K be radially symmetric, $K \in \Omega_{2m}$, with, $K(X) \in L^1(\mathbb{R}^2)$, $D_{r,\Phi}^{2m} K(X) \in L^1(\mathbb{R}^2)$, for each $r \in [0, \infty)$, and,

$$\sup \{ \| D_{r, \bar{\phi}}^{2m} K(X) \|_1 : r \geq 0 \} = L < \infty.$$

Then, for all $A \geq 1$,

$$\| f_A \|_{2m} \leq M_8 A^{2m} \| f \|_0,$$

where M_8 is a constant independent of A and f .

Proof

We have,

$$\begin{aligned} D_{r, \bar{\phi}}^{2m} f_A(X) &= \frac{\partial^{2m}}{\partial r^{2m}} \frac{1}{2\pi} \int_0^{2\pi} \int_{T \in \mathbb{R}^2} f(X + re^{i\phi} - \frac{T}{A}) K(T) dT d\phi \\ &= \frac{\partial^{2m}}{\partial r^{2m}} \frac{1}{2\pi} \int_0^{2\pi} \int_{T \in \mathbb{R}^2} f(T) K(A(X - T + re^{i\phi})) A^2 dT d\phi. \end{aligned}$$

Now using Fubini's theorem, we get,

$$\begin{aligned} D_{r, \bar{\phi}}^{2m} f_A(X) &= \int_{T \in \mathbb{R}^2} f(T) \frac{\partial^{2m}}{\partial r^{2m}} K_{Ar, \bar{\phi}}(A(X - T)) A^2 dT \\ &= A^{2m} \int_{T \in \mathbb{R}^2} f(X - \frac{T}{A}) \frac{\partial^{2m}}{\partial r^{2m}} K_{r, \bar{\phi}}(T) dT \end{aligned}$$

Hence,

$$\begin{aligned} \| D_{r, \bar{\phi}}^{2m} f(X) \|_0 &\leq A^{2m} \| f \|_0 \int_{T \in \mathbb{R}^2} \left| \frac{\partial^{2m}}{\partial r^{2m}} K_{r, \bar{\phi}}(T) \right| dT \\ &\leq L A^{2m} \| f \|_0. \end{aligned}$$

We have already shown, (Lemma 4.1.3)

$$||f_A||_0 \leq M_6 ||f||_0.$$

Thus,

$$||f_A||_{2m} = ||f_A||_0 + \sup_{r \geq 0} ||D_{r, \bar{\phi}}^{2m} f_A||_0$$

$$\leq LA^{2m} ||f||_0 + M_6 ||f||_0$$

$$\leq M_7 A^{2m} ||f||_0$$

where $M_7 = L + M_6$, and we note that $A \geq 1$. This completes the proof.

Lemma 4.1.5

Let, $f \in \Omega_{2m}$, $K(X) \in L^1(\mathbb{R}^2)$, be radially symmetric, then,

$$||f_A||_{2m} \leq M_8 ||f||_{2m}$$

where M_8 is a constant independent of f .

Proof

$$\begin{aligned} & ||D_{r, \bar{\phi}}^{2m} f_A(X)||_0 \\ &= ||D_{r, \bar{\phi}}^{2m} \int_{\mathbb{R}^2} f(X-T) A^2 K(AT) dT||_0 \end{aligned}$$

$$= \left\| \int_{\mathbb{R}^2} \{ D_{r, \bar{\phi}}^{2m} f(X-T) \} A^2 K(AT) dT \right\|_0$$

$$\leq \left\| D_{r, \bar{\phi}}^{2m} f(X) \right\|_0 \int_{\mathbb{R}^2} A^2 |K(AT)| dT$$

$$= M_{81} \left\| D_{r, \bar{\phi}}^{2m} f \right\|_0$$

$$\leq M_{81} \|f\|_{2m}$$

where, $M_{81} = \|K(X)\|_1$.

We have already proved, (Lemma 4.1.3., Def of $\|\cdot\|_{2m}$)

$$\|f_A\|_0 \leq M_6 \|f\|_0 \leq M_{82} \|f\|_{2m}, \text{ say.}$$

Hence, we have,

$$\begin{aligned} \|f_A\|_{2m} &= \|f_A\|_0 + \sup_r \{ \|D_{r, \bar{\phi}}^{2m} f_A\|_0 : r \geq 0 \} \\ &\leq M_8 \|f\|_{2m} \end{aligned}$$

where, $M_8 = M_{81} + M_{82}$,

completing the proof.

4.2 Theorem

Let, $K \in \mathcal{IK}^{2m}$, $f \in \Omega_0$, and β be a real number such that, $0 < \beta < 2m$. Then,

$$||f_A - f||_0 = O(A^{-\beta})$$

as $A \rightarrow \infty$,

if, and only if, $f \in \Omega_{2m}^\beta$.

Proof:

Let, $||f_A - f||_0 = O(A^{-\beta})$, with $0 < \beta < 2m$.

Since, $K \in \mathcal{IK}^{2m}$, in view of the localization lemma (3.6), K could be assumed to have compact support.

Then the conditions for lemmas (4.1.2) - (4.1.5) are satisfied implying that $f_A \in \Omega_{2m}$. So, for any given

$g \in \Omega_{2m}$,

$$\begin{aligned} ||f_A||_{2m} &= ||(f-g)_A + g_A||_{2m} \\ &\leq ||(f-g)_A||_{2m} + ||g_A||_{2m}. \end{aligned}$$

Thus, for any $t > 0$,

$$\begin{aligned} ||f_A - f||_0 + t^{2m} ||f_A||_{2m} &\leq O(A^{-\beta}) + t^{2m} \{ ||(f-g)_A||_{2m} \\ &\quad + ||g_A||_{2m} \}. \end{aligned}$$

Now, by lemmas (4.1.3) and (4.1.4),

$$||(f-g)_A||_{2m} \leq M_7 A^{2m} ||(f-g)||_0,$$

and, $||g_A||_{2m} \leq M_8 ||g||_{2m}.$

Thus,

$$||f - f_A||_0 + t^{2m} ||f_A||_{2m} \leq O(A^{-\beta}) + t^{2m} \{M_7 A^{2m} ||(f-g)||_0 + M_8 ||g||_{2m}\}$$

Taking infimum over $g \in \Omega_{2m}$, we have,

$$K_P(t^{2m}; f) = O[A^{-\beta} + (At)^{2m} K_P(\frac{1}{A^{2m}}; f)],$$

where K_P is the Peetre's functional (Section 2.3.4). Now using Berens-Lorentz lemma [31], we get

$$K(t^{2m}; f) = O(t^\beta),$$

i.e., $f \in \Omega_{2m}^\beta.$

Conversely,

assuming, $f \in \Omega_{2m}^\beta$, for each $t > 0$, we have a $g_t \in \Omega_{2m}$, such that,

$$||f - g_t||_0 \leq M_9 t^\beta,$$

and, $||g_t||_{2m} \leq M_{10} t^{\beta-2m}.$

Hence by triangle inequality,

$$||f_A - f||_0 \leq ||f_A - (g_t)_A||_0 + ||(g_t)_A - g_t||_0 + ||g_t - f||_0 .$$

Now using lemma (4.1.3) and theorem (3.5),

$$||f_A - f||_0 \leq (M_7+1) ||f - g_t||_0 + \frac{M_2}{A^{2m}} ||g_t||_{2m} .$$

Choosing, $t = \frac{1}{A}$, we get,

$$||f_A - f||_0 \leq (M_7 + 1) M_9 A^{-\beta} + \frac{M_2}{A^{2m}} M_{10} A^{2m-\beta}$$

$$= [(M_7+1)M_9 + M_2 M_{10}] A^{-\beta}$$

$$= O(A^{-\beta}) .$$

This completes the proof.

CHAPTER 5

RESULTS

A discrete version of the parallel-beam CBP algorithm was implemented on the DEC-1090 computer system. The seven windows chosen for the study are given in Table (5.1). These windows have been listed in increasing order of their $|W''(0)|$, the second derivative (w.r.t. the Fourier frequency) at the origin in the Fourier space. For the generalized Hamming window, the cases H91 and H75 have been chosen because, for these windows, the values of $W''(0)$ are the same as those for the sinc and the cosine windows respectively.

Initial test cases were run on a unit pixel. Next, extensive computer experiments were performed (with varying R_c) on a simulated image of a damaged nuclear fuel bundle (NFB). Finally, reconstructions were obtained for a simulated cross-section of a human brain.

Projection data was generated by numerical integration with a step-size equalling $\Delta s/3$. The cut-off frequency, R_c , was chosen as per the sampling criterion [2]. Also, to reduce the discretization errors related to the back-projection integral, the number of projection views, NVIEW, were linked to the number of rays, NRAY, by the following equation [2] :

$$\text{NVIEW} = ((\text{NRAY}-1)/2)\pi$$

Table 5.1 : Windows Considered in the Study

Window	Code	$ W'(0) $	$ W''(0) $
Generalized Hamming $\alpha = 0.999$	H99	0.0	0.001
Generalized Hamming $\alpha = 0.917$	H91	0.0	0.083
Sinc	Sinc	0.0	0.083
Generalized Hamming $\alpha = 0.80$	H80	0.0	0.20
Generalized Hamming $\alpha = 0.75$	H75	0.0	0.25
Cosine	Cos	0.0	0.25
Generalized Hamming $\alpha = 0.54$	H54	0.0	0.46

Note : Table (2.1) gives the expressions for these windows.

106303

The errors reported are of the following type:

$$\text{ERMIN} = \text{Min } (\tilde{f} - f)$$

$$\text{ERMAX} = \text{Max } (\tilde{f} - f)$$

$$\text{ERL1} = \frac{1}{\text{MP}} \sum_i \sum_j |(\tilde{f}_{ij} - f_{ij})|$$

$$\text{ERL2} = \frac{1}{\text{MP}} \sum_i \sum_j |\tilde{f}_{ij} - f_{ij}|^2 \quad 1/2$$

$$\bar{E} = \frac{1}{\text{NP}} \sum_i \sum_j |\tilde{f}_{ij}^{\text{CD}} - f_{ij}^{\text{CD}}|$$

Here,

MP represents the total number of pixels considered for evaluation of ERL1 and ERL2,

NP represents the total number of pixels considered for evaluation of \bar{E} ,

and, superscript CD implies the value of the function after the 32 gray level coding.

The errors, ERL1 and ERL2, represent the usual l_1 and l_2 errors. The error \bar{E} represents an index of visual quality of the reconstructed image. For a given window and a fixed R_c , ERMIN and ERMAX give an indication of smoothness of the function concerned. Some researchers

use l_2 errors for comparing reconstructed images while others report error-measures similar to those used in this study.

We note that the radius of integration for the evaluation of \bar{E} is 1.0, while that for the evaluation of ERL1 and ERL2 is 0.9. This reduced radius was chosen as the majority of the region of interest (for the images considered in this study) is covered by a radius of 0.9 units.

The normalized errors corresponding to ERL1, ERL2, and \bar{E} are defined as follows:

$$\text{ERL1N} = \frac{(\text{ERL1}) (\text{MP})}{\sum_i \sum_j |f_{ij}|}$$

$$\text{ERL2N} = \frac{(\text{ERL2}) (\text{MP})}{\sum_i \sum_j |f_{ij} - \bar{f}|^2}^{1/2}$$

$$\overline{\text{EN}} = \frac{(\bar{E}) (\text{NP})}{\sum_i \sum_j |f_{ij}^{\text{CD}}|}$$

Here, \bar{f} denotes the function value averaged over the entire region of interest. Again, as in the previous case, ERL1N and ERL2N were calculated for the picture region of 0.9 radius.

5.1 Reconstruction of a Unit Pixel

Test runs, involving the reconstruction of a unit pixel, were performed using 65 rays and 100 views. Figures (5.1) - (5.4) depict the normalized log magnitude plots (for the central ray, $\phi = 0$) of the reconstructions obtained from projection data of the unit pixel. Following Herman [1], the output parameters of interest are listed below:

- (i) $\tilde{f}_{DB}(r)$ is the normalized log output

$$= 10 \log_{10} \left| \frac{\tilde{f}(r, 0)}{\tilde{f}(0, 0)} \right|$$
- (ii) Half-width at half-maximum (HWHM) is the smallest positive r such that $\tilde{f}_{DB}(r) = 10 \log_{10} 0.5$
- (iii) Size of the first overshoot is the value of $\tilde{f}_{DB}(r)$ such that $\tilde{f}_{DB}(r_{-1}) < \tilde{f}_{DB}(r) < \tilde{f}_{DB}(r_{+1})$.
On the given discretization, the point r_{-1} precedes point r and the point r_{+1} follows point r .
- (iv) The tail is the value of \tilde{f}_{DB} for the last pixel, i.e., $\tilde{f}_{DB}(0.9)$.

Table (5.2) shows the above-mentioned parameters of interest for the reconstructions using all the seven windows. The H99 window has the minimum HWHM but the largest 'tail' and the largest 'first overshoot'. The

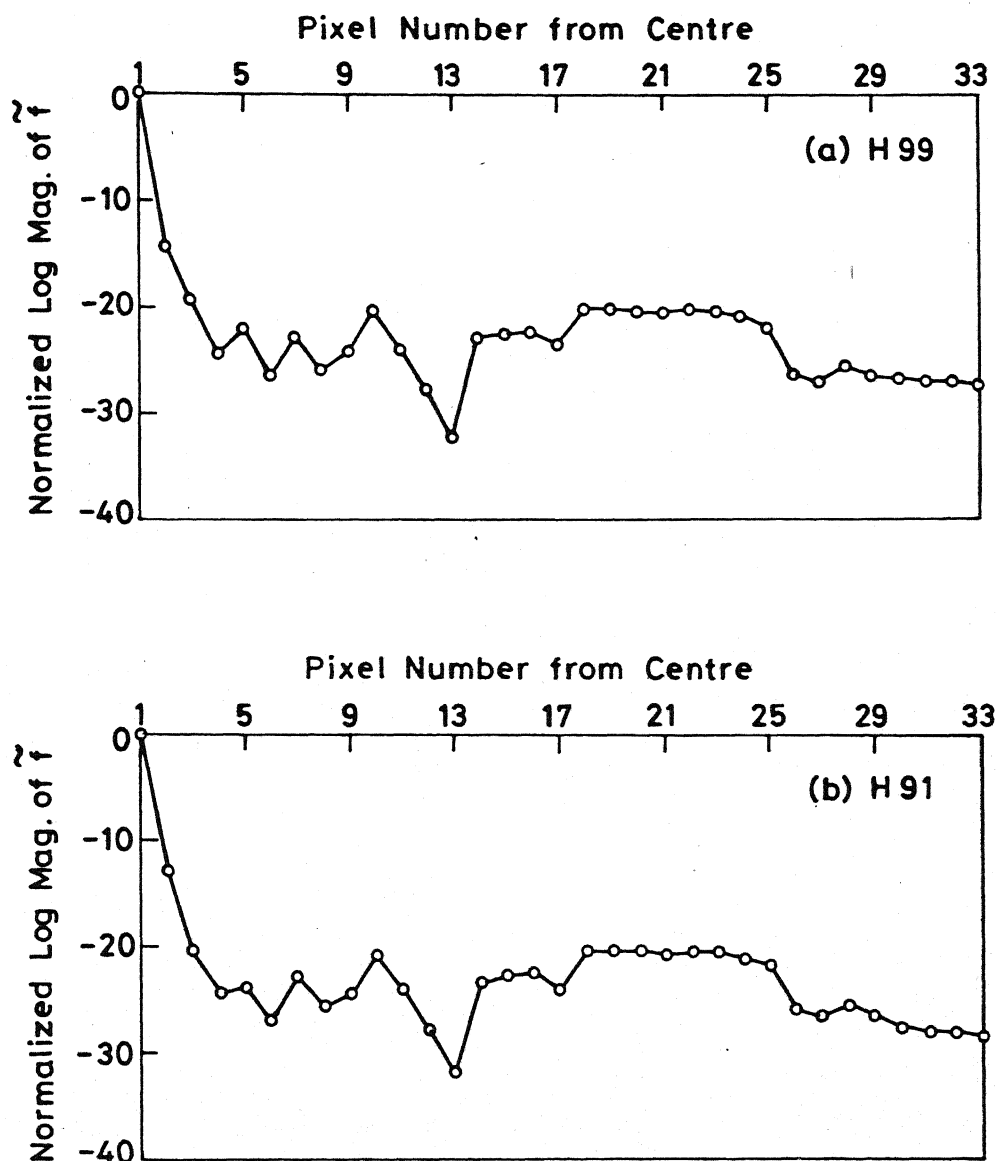


Fig. 5.1 Unit Pixel response for (a) H99 window
(b) H91 window.

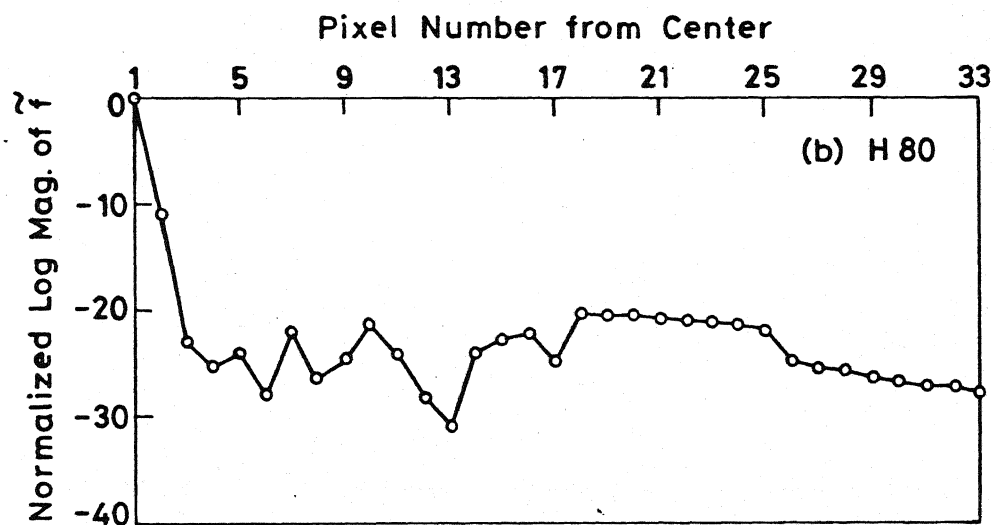
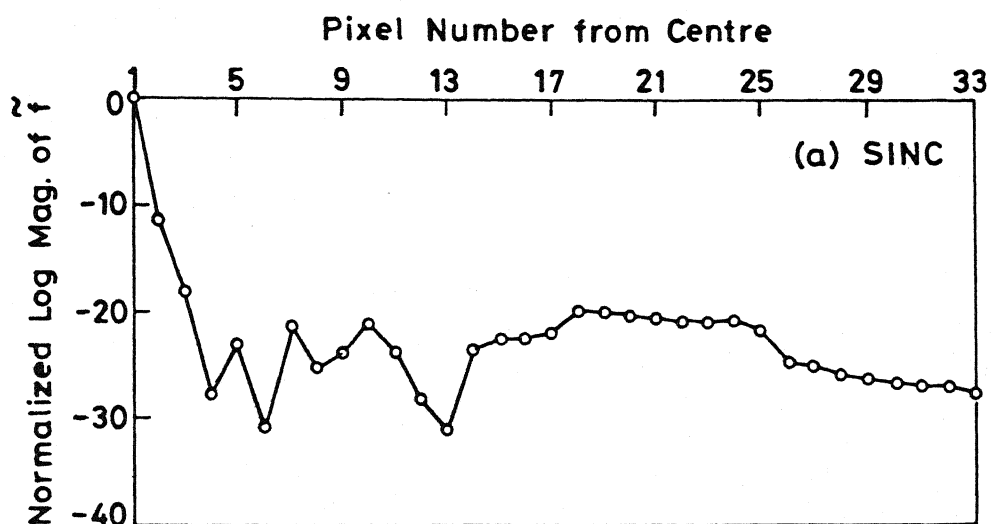


Fig. 5.2 Unit Pixel response for (a) SINC window
(b) H 80 window

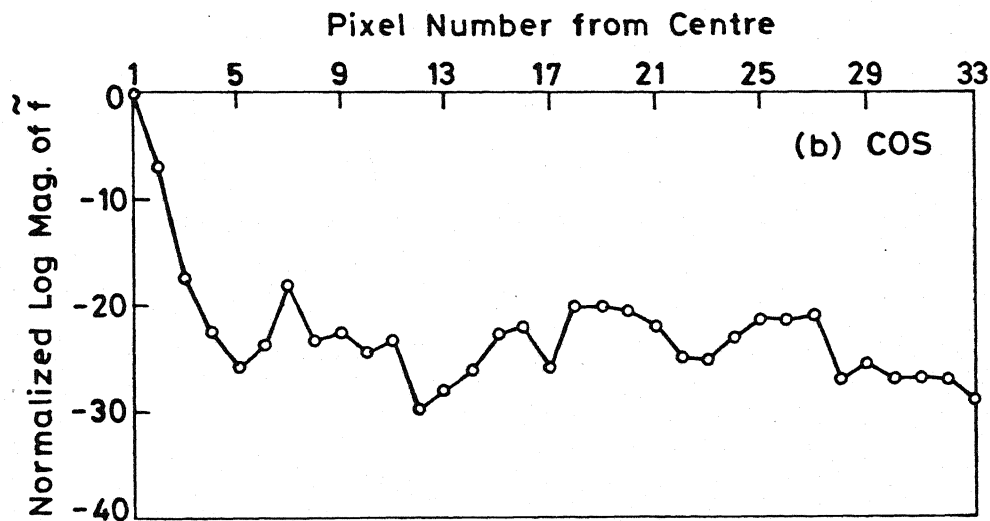
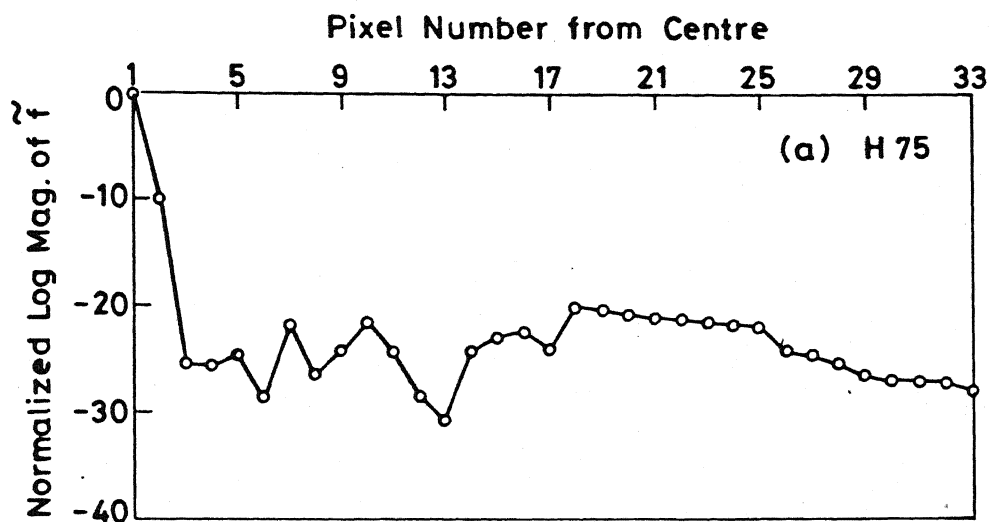


Fig. 5.3 Unit Pixel response for (a) H 75 window
(b) COS window.

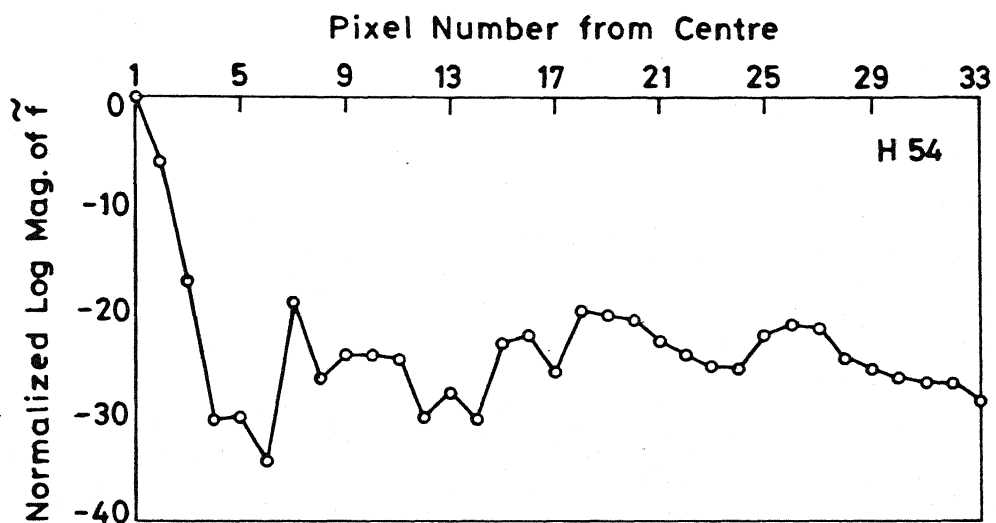


Fig. 5.4 Unit Pixel response for H 54 window .

Table 5.2 : Reconstruction Parameters

Ray-spacing , Δs	R_c	Number of views	Number of Rays
2/65	16.25	100	65
2/64	16.00	100	64
2/128	32.00	200	128
2/256	64.00	400	256

Note : (a) 65-ray combination used only in the unit pixel reconstruction

(b) Sampling $R_c = (1/2\Delta s)$

(c) Optimal NVIEW = $((N_{RAY}-1)/2)\pi$

window H54 has the maximum HWHM and the smallest 'tail' and first 'overshoot'. These results (Table (5.3)) agree with point-response results reported by Herman [1].

5.2 Reconstruction of a Simulation of a Damaged Nuclear Fuel-Bundle (NFB)

Figure (5.5) shows a 64x64 digitized simulation of the cross-section of a 9x9 NFB consisting of 79 good fuel rods and 2 damaged fuel rods. The normal fuel-rods are represented by 2x2 white squares (4 pixels) while the damaged rods are shown by dark squares. The dark lines represent the coolant fluid flowing through the fuel-bundle. To observe the 'edge-effects', some extra squares and two rings were included in the overall image. A suitable 32 gray-level scheme was chosen for overprinting purposes.

Reconstructions were performed using all the seven windows mentioned in Table (5.1). Also for each window, three cases were run for R_c -values of 16, 32, and 64. The corresponding rays and views are given in Table (5.2). The reconstructed images (small size) appear in Figs. (5.6) - (5.12) for all the seven windows (see Appendix A for large-size images of the same reconstructions). The summary of errors appears in Tables (5.4)-(5.5). The tables reveal that for each window all the errors reduce with increasing R_c . In fact, doubling R_c reduces the

Table 5.3 : Reconstruction Results of Figs.(5.1)-(5.4) for the Unit Pixel

Window Code	HWHM	First Overshoot	Tail
H99	0.210	-22.763	-27.429
H91	0.230	-23.150	-27.501
Sinc	0.260	-23.203	-27.735
H80	0.280	-24.028	-27.646
H75	0.300	-24.634	-27.733
Cos	0.430	-23.834	-29.069
H54	0.500	-30.157	-28.556

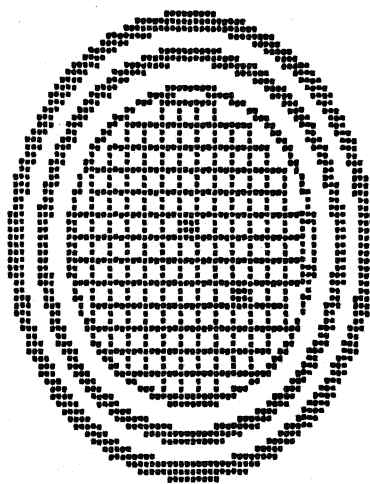
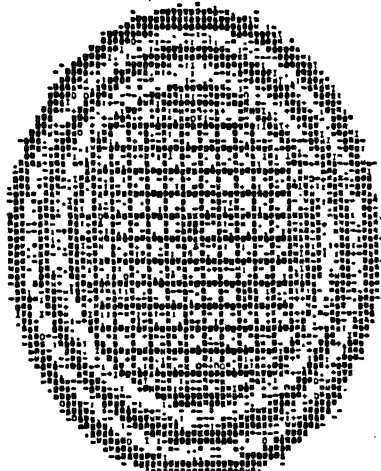


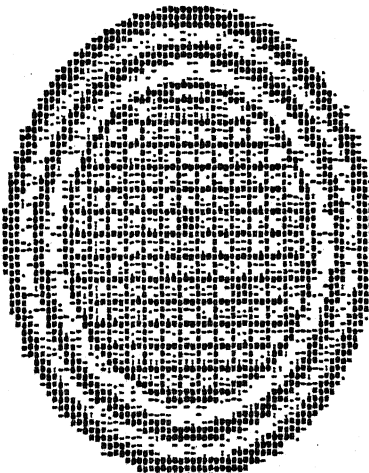
Fig 5.5 Original simulation of damaged nuclear fuel bundle (NFB)

NA*297.64 P14264 CODED CORR NPIC= 64*PIC= 64*HANDLE= 12000000 64*P= 300 312*12000000*12000000*12000000*12000000



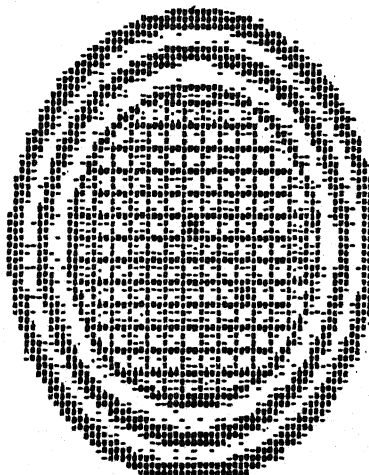
(a)

NPIC= 64*PIC= 64*HANDLE= 12000000 64*P= 300 312*12000000*12000000*12000000*12000000
NA*297.64 P14264 CODED CORR NPIC= 64*PIC= 64*HANDLE= 12000000 64*P= 300 312*12000000*12000000*12000000*12000000



(b)

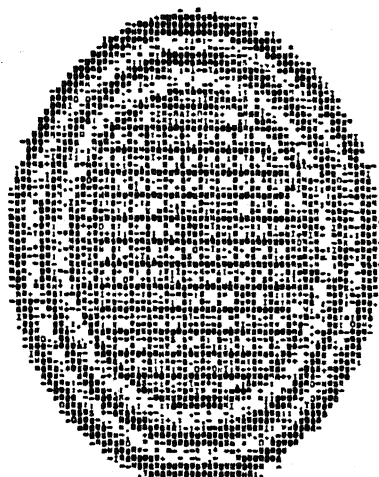
NPIC= 64*PIC= 64*HANDLE= 12000000 64*P= 300 312*12000000*12000000*12000000*12000000
NA*297.64 P14264 CODED CORR NPIC= 64*PIC= 64*HANDLE= 12000000 64*P= 300 312*12000000*12000000*12000000*12000000



(c)

NPIC= 64*PIC= 64*HANDLE= 12000000 64*P= 300 312*12000000*12000000*12000000*12000000
NA*297.64 P14264 CODED CORR NPIC= 64*PIC= 64*HANDLE= 12000000 64*P= 300 312*12000000*12000000*12000000*12000000

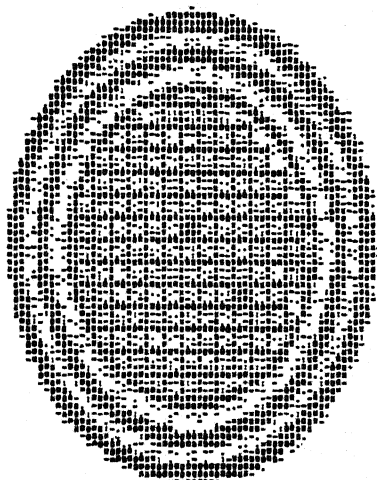
Fig. 5.6 Reconstruction of NFB with H99 Windows for (a) $R_c=16$ (b) $R_c=32$ and (c) $R_c=64$



(a)

MIN= 0.1044IN 12ENROR= 3.00%16ENROR= 3.95%10N%1EGL= 3300NPTHEL= 2012ENRITM= -10.06200ENHAY= 17.4005TERL1= 4.0600;ENL2= 5.67030

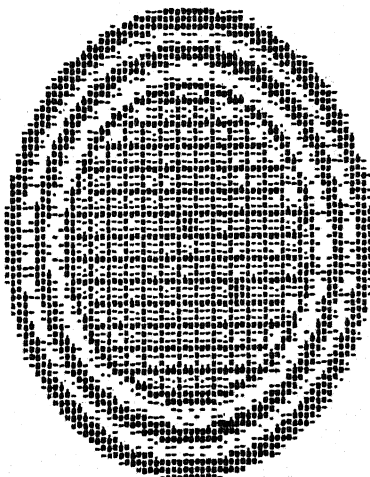
HA#917/287.64 P44K64 CODED CODE MPIC 64MPIC 64ANGLE= 200HAY= 120K= 3K= 11CR= 120ST= 91V= 01U= 001/P4P= 0PT= CUT= 10. 24000



(b)

MJN= -CHANE YERRRN 2.0000CROO= 2.0601INPXLW 333NPXHLA PRIGERNIS =-4.40706E94YU 6.78690E3LW 3.23633E2L3= 2.66346

NAN017/297.64 P04X64 CODED CORE WPIC= 84WPICn 64WANGLEn 64WDATe 35KPs 3ER= JTCN-1T00T=0ITP=0IUP=0IFSP=0ETCCTw10.0000

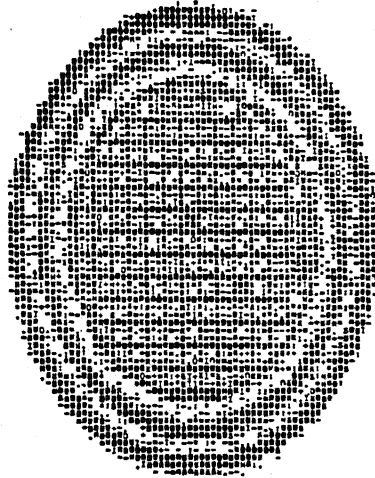


(c)

P1=0.044Xm Z=0.070m 1.0000000000 1.0119457181e 333797121e 201300712e -4.197372844Xm 3.478312211e 1.009342212e 1.27769

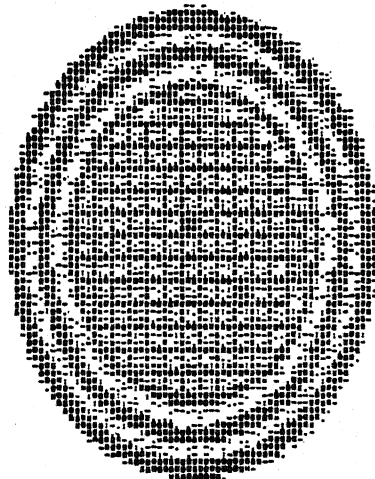
Fig. 5.7 Reconstruction of NFB with H 91 windows for (a) $R_c = 16$ (b) $R_c = 32$ and (c) $R_c = 64$.

Reconstruction of NFB with SINC windows



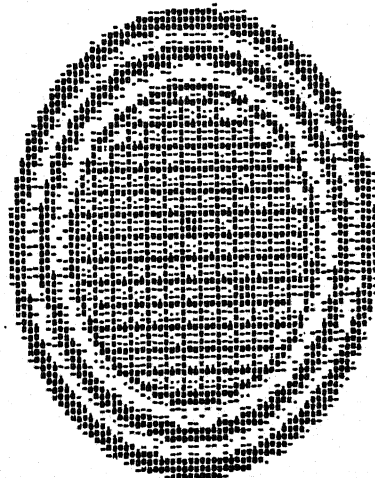
(a)

Reconstruction of NFB with SINC windows



(b)

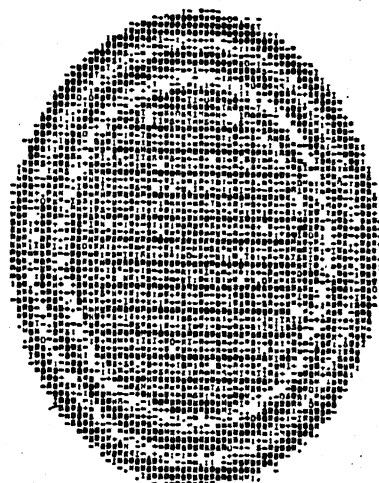
Reconstruction of NFB with SINC windows



(c)

Reconstruction of NFB with SINC windows

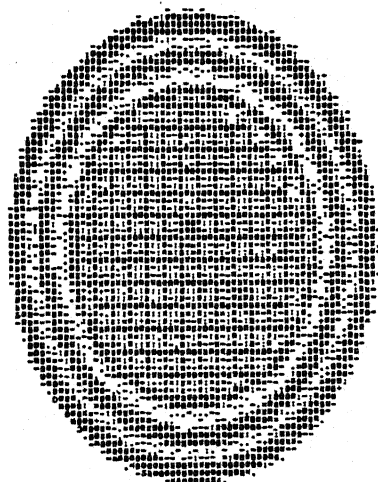
Fig. 5.8 Reconstruction of NFB with SINC windows for (a) $R_c = 16$ (b) $R_c = 32$ and (c) $R_c = 64$.



(a)

MIN = 184AX= 17EQROR= 5.29440CQROR= 1.45432NPIXEL= 3300NPIXEL= 2513EQUAT= -17.886318QRAN= 16.533402261= 5.614362262= 6.57637

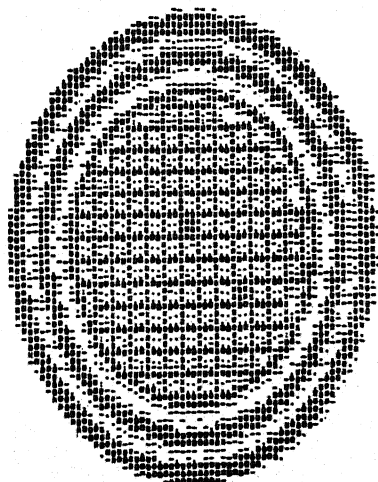
HAHM/287.64 F64K64 CNOED CDEE "PIC" 64HPICw 64HANGLE= 2800RAY= 120Kw 3Kw 3YCN=1Y80RY=0ISF=0IUP=0IFB=0PGRCHY=10.0000



(b)

NAME - PHAX= BGROR= 2.91897CNROR= 3.0776JNPAGL= 3352NPICL= 2512GRNIN= -4.06030GRAX= 8.4793JRLI= 3.18402XU62= 3.61637

HAQWU/H87.64 F64154 CODED CORE WPIC 64HPIC 64HAGLEN 640NATY 334P= 3H40 IXCALISGRTGSIUP=SIUP=OIFR=OPXRCUT=10.0000

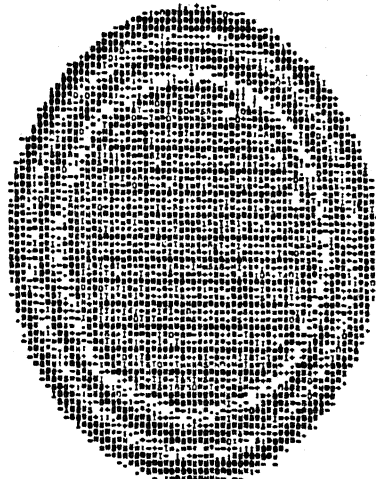


(c)

P10 = 0.5430; GEFH00 = 1.5331; C0000 = 1.5531; 40P1010 = 1.3330; 101010 = 0.5120; 101010 = -0.4270; 040000 = 0.3780; 0010 = 1.5240; 0010 = 1.5000

Fig. 5.9 Reconstruction of NFB with H80 windows for (a) $R_c = 16$ (b) $R_c = 32$ and (c) $R_c = 64$.

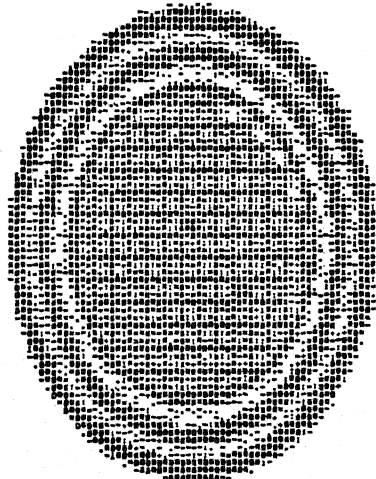
HA75/257.64 P4454 CODED CODE NPIC 640PIC 640ANGLE 1000ALV 640P 36P 270AL1000ALV 0100001000010000100000



(a)

PIA -104ALV 000000 1.001000000 4.745000100 10000100 20100000 -10.00100000 11.10400000 6.27100000 7.10000

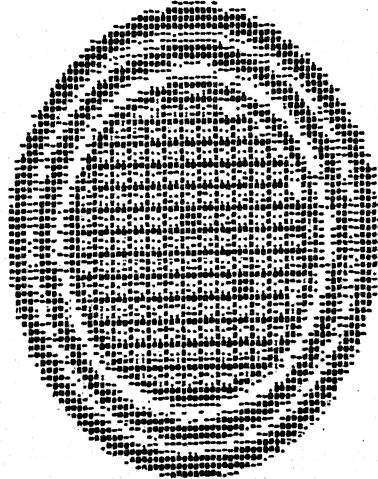
HA75/257.64 P4454 CODED CODE NPIC 640PIC 640ANGLE 1000ALV 640P 36P 270AL1000ALV 0100001000010000100000



(b)

PIA -104ALV 000000 1.221000000 3.945000100 10000100 20100000 -9.634100000 9.20000000 3.99000000 4.60700

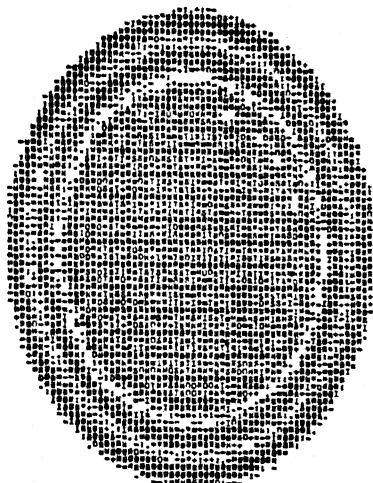
HA75/257.64 P4454 CODED CODE NPIC 640PIC 640ANGLE 1000ALV 640P 36P 270AL1000ALV 0100001000010000100000



(c)

PIA -104ALV 000000 1.731000000 1.700000100 10000100 20100000 -8.102000000 4.70000000 1.00000000 2.10000

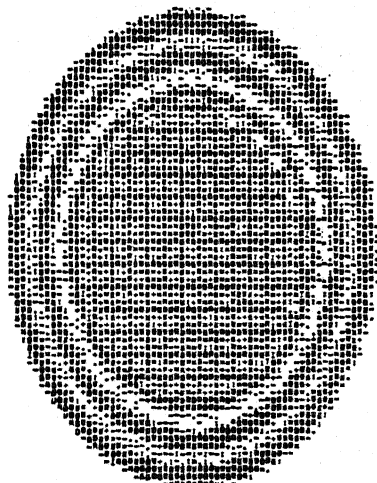
Fig. 5.10 Reconstruction of NFB with H75 windows for (a) $R_c = 16$ (b) $R_c = 32$ and (c) $R_c = 64$.



(a)

PI6 -39416 1000000 7.16782C0000 7.00000P1C6 33004P1C6 251200170 -14.00000P0A2 17.00001C610 7.70070C612 0.00200

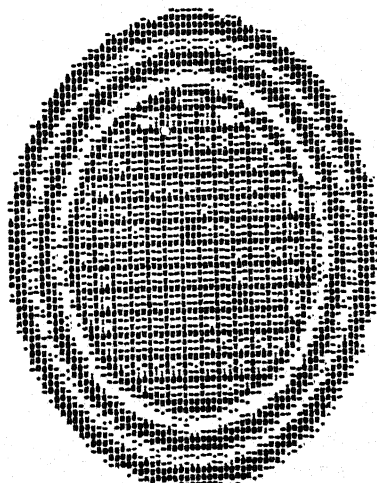
C00207.64 P4264 C0000 C000 MPIC 640P1C6 640A0L6 1000A76 640A 3000 31C61100076170P017000170000P0C710.00000



(b)

PI6 -315416 1000000 5.00220C0000 4.12010P1C6 33220P1C6 251200170 -10.50010P0A2 10.10000C610 0.17000P0A2 0.00300

C00207.64 P4264 C0000 C000 MPIC 640P1C6 640A0L6 1000A76 640A 3000 31C61100076170P017000170000P0C710.00000



(c)

PI6 -25420 1000000 5.00007C0000 2.17710P1C6 33220P1C6 251200170 -0.00720P0A2 0.20220C610 2.10777C612 2.00077

Fig. 5.11 Reconstruction of NFB with COS windows for (a) $R_C=16$ (b) $R_C=32$ and (c) $R_C=64$.

Table 5.4 : Effect of Cut-off Frequency, R_c , on Reconstruction Errors for the Nuclear Fuel Bundle

Window	$ W''(0) $	R_c	EMIN	EMAX	ERL1	ERL2	\bar{E}
H99	0.001	16	-19.5881	18.4850	4.3681	5.5141	3.210
		32	- 8.1039	5.7470	1.6940	2.1263	1.390
		64	- 3.9432	3.0305	7.7650	0.9864	0.650
H91	0.083	16	-18.8628	17.6005	4.5600	5.6703	3.880
		32	- 8.4070	6.7809	2.2363	2.6534	2.060
		64	- 4.1973	3.4703	1.0892	1.2976	1.000
Sinc	0.083	16	-18.1672	17.4219	4.8239	5.8837	4.260
		32	- 8.5377	7.1479	2.4337	2.8522	2.200
		64	- 4.2274	3.6604	1.2078	1.4123	1.120
H80	0.200	16	-17.8563	16.5334	5.6143	6.5762	5.200
		32	- 9.0565	8.4793	3.1640	3.6163	2.910
		64	- 4.6270	4.3788	1.6244	1.8505	1.510
H75	0.250	16	-18.2521	16.1644	6.2710	7.1462	5.880
		32	- 9.6341	9.2050	3.5904	4.0675	3.330
		64	- 4.8352	4.7669	1.8597	2.1052	1.730
Cos	0.250	16	-19.2868	17.9894	7.7057	8.5829	7.140
		32	-10.5801	10.1494	4.1700	4.6838	3.880
		64	- 5.0573	5.2532	2.1877	2.4607	2.060
H54	0.460	16	-20.2559	18.6033	9.5674	10.2007	8.890
		32	-12.0598	12.2534	5.4762	6.0751	5.070
		64	- 6.1569	6.4198	2.8741	3.2227	2.720

Window	$ w''(0) $	R_c	ERL1N	ERL2N	\overline{EN}
H99	0.001	16	0.2925	0.3560	0.199
		32	0.1134	0.1373	0.086
		64	0.0512	0.0637	0.040
H91	0.083	16	0.3054	0.3661	0.241
		32	0.1497	0.1713	0.128
		64	0.0729	0.0838	0.062
Sinc	0.083	16	0.3230	0.3798	0.264
		32	0.1630	0.1841	0.136
		64	0.0809	0.0912	0.069
H80	0.200	16	0.3760	0.4246	0.323
		32	0.2119	0.2335	0.180
		64	0.1088	0.1195	0.093
H75	0.250	16	0.4200	0.4614	0.365
		32	0.2404	0.2626	0.206
		64	0.1245	0.1359	0.107
Cos	0.250	16	0.5160	0.5541	0.443
		32	0.2793	0.3024	0.241
		64	0.1465	0.1589	0.128
H54	0.460	16	0.6407	0.6586	0.552
		32	0.3667	0.3922	0.315
		64	0.1925	0.2081	0.169

errors by (approx.) 50% for most windows. This factor is higher ($\approx 67\%$) for the H99 window.

Figures (5.13) - (5.15) show the effect of $|W''(0)|$ on the reconstruction errors. It has been observed that an increase in the value of $|W''(0)|$ leads to an almost linear increase in the errors, $ERL1N$, $ERL2N$ and \overline{EN} .

5.3 Reconstruction of a Simulation of a Human-brain Cross section

Figure (5.16) shows a 64×64 digitization of a cross-section of a human-brain [32]. The central region shows a damaged portion having a density different from that of the healthy tissues surrounding it.

Figures (5.17)-(5.23) show the reconstruction results using the seven window functions for three cases of R_c values of 16, 32 and 64. Tables (5.6) and (5.7) give the corresponding summary of errors obtained in the reconstructions. The pattern of errors is similar to that of the NFB case. Errors reduce by (approx.) 50% when R_c is doubled except for the H99 window where the factor is approx. 67%. For a given R_c , the performance of the window is again related to $|W''(0)|$. Errors increase almost linearly with increasing $|W''(0)|$ as is clear from Figs. (5.24)-(5.26). For large-size reconstructed images, see Appendix B.

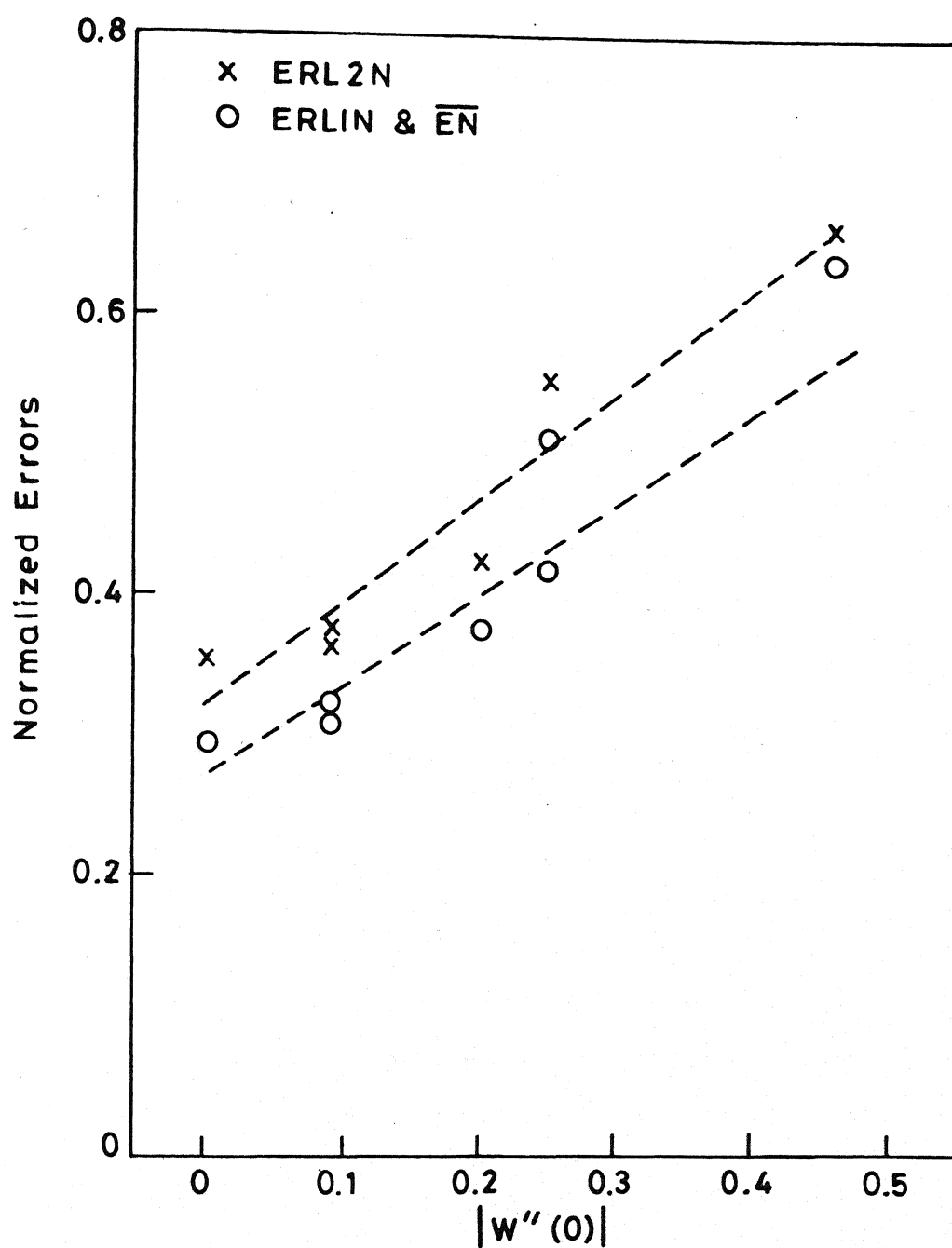


Fig. 5.13 Comparative performance (on NFB) of various windows for $R_c=16$

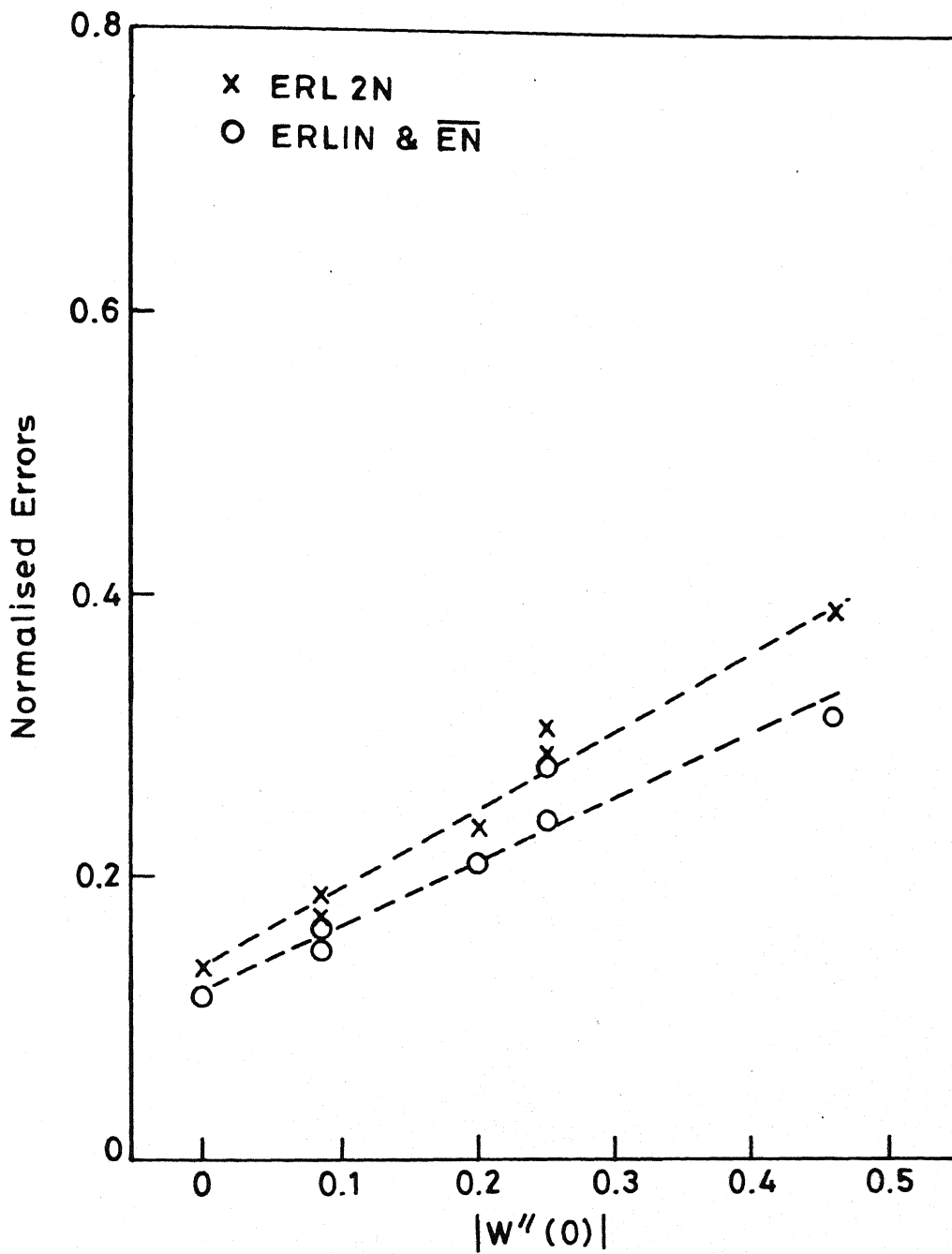


Fig. 5.14 Comparative performance (on NFB) of various windows for $R_c=32$

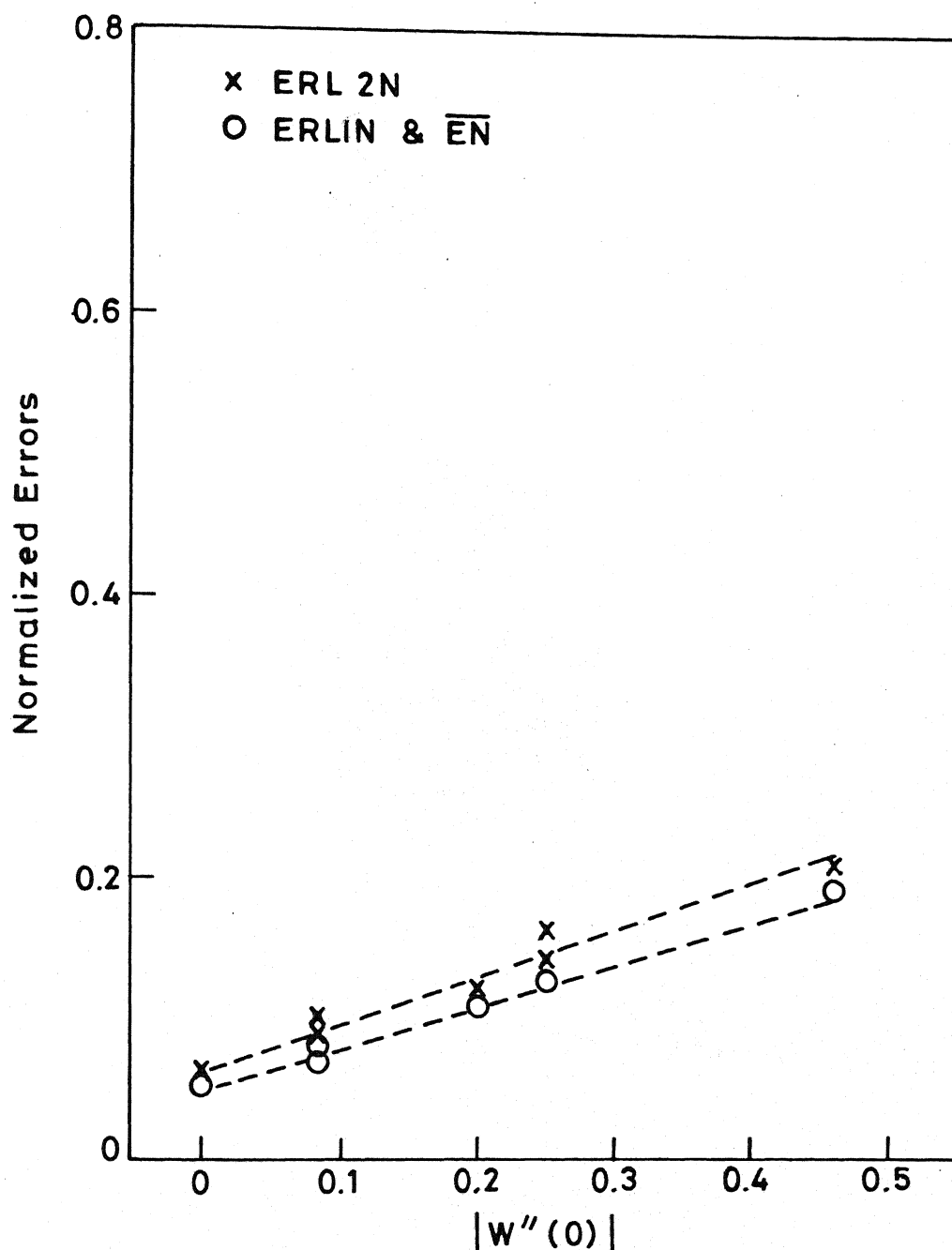


Fig. 5.15 Comparative performance (on NFB) of various windows for $R_c = 64$

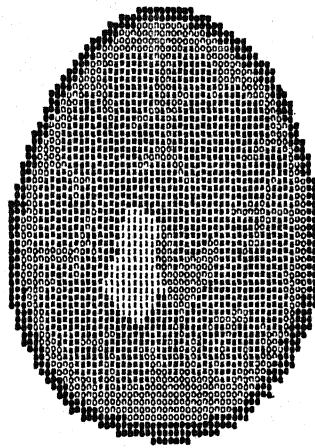
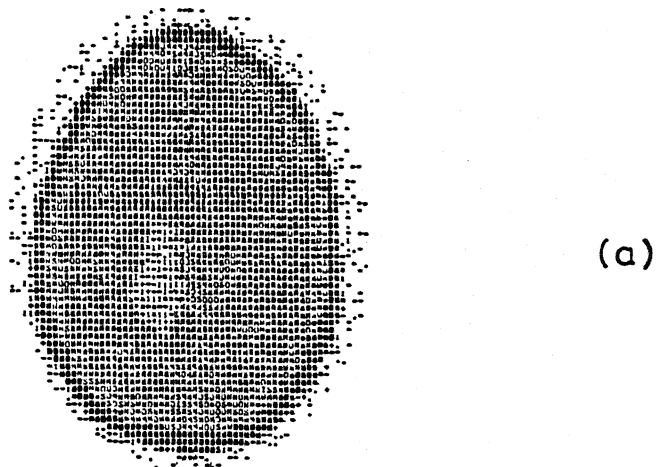


Fig. 5.16 Original simulation of human brain.

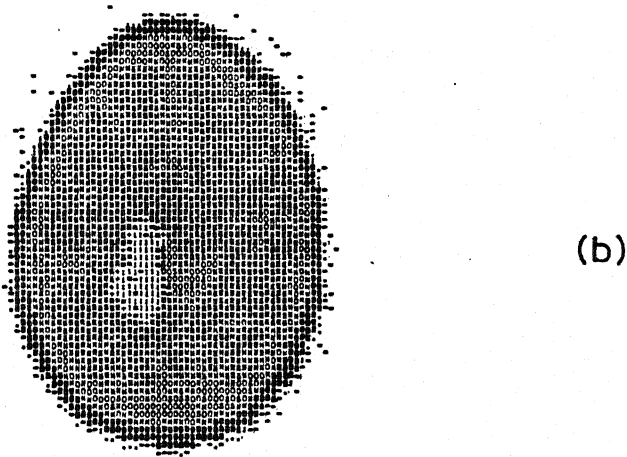


Fig. 5.17 Reconstruction of human brain with H99 window for (a) $R_C=16$ (b) $R_C=32$ and (c) $R_C=64$



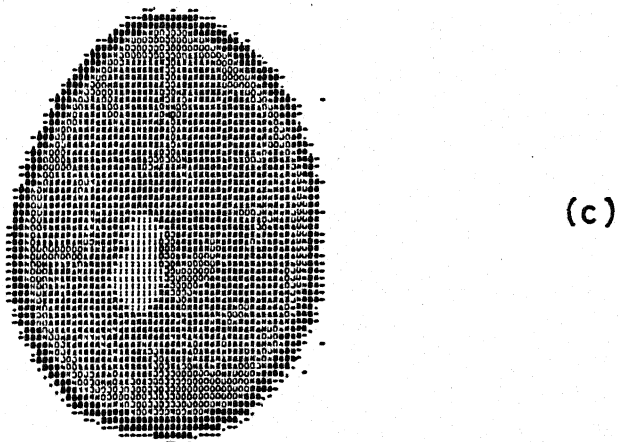
NAME = IONAK= IERADN= 1.62926CHRU= 1.57604NPICL= 3306NPICL= 3612KRT= -9.89873KRA= 10.77874KEL= 1.05836CEL= 2.27247

MM0917/807.64 F64K64 CROCO PICTUREPIC= 64NPICn 64ANGLE= 280DATA; 202P= 3KB 2ICHn; 202TogInP=0; Up=0; IF2=0; PCHT=10.0000



MINS -AMATO SCROON 0.8443DCWOp 0.6730INPXLN B337NPXELN D312RNINO -d.83470PRAZL 3.40347RNLN 0.69548RNLJ= 0.94416

MANV17/257.66 F84156 CODED PICTUREPIC= 64MPIC= 64ANGLE= 000RAT= 250Kp= 3Kb= ATCR=1150RY=0YMP=0IND=0IFBP=0PERCENT=10.00000



MIN= -3MAX= 2ECON= 0.7172VCADUM= 0.24248NP1EKL= 0.3340P1EKL= 2512EKLIN= -1.99964CMAAN= 1.61827EKLIN= 0.32271EKL2= 0.67540

Fig. 5.18 Reconstruction of human brain with H91 window for (a) $R_C = 16$ (b) $R_C = 32$ and (c) $R_C = 64$



SNPP707.64 F64164 CODED PICTUREPIC= 64NPIC= 64ANGLE= 200PRAY= 120PR= 3KB= 11CRA1:8ART=0:1PR=0:1NO=0:17PR=0:1PRCT=10.00000

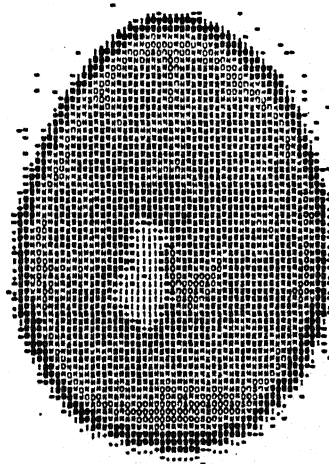
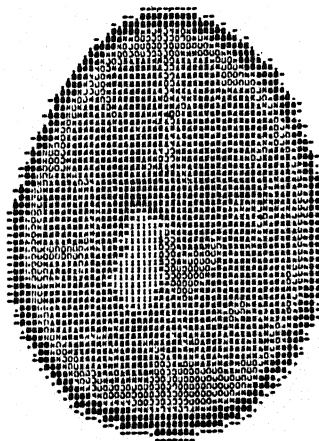


BMP:b7.c6 Pict400 COULD PICTURE:PIC= b4NPIC= 64H4UGLE= 40DHAY= 25bKp= 363b JYCR=18URX=51dP=0IUD=61FDP=pqPRINT=18.01000



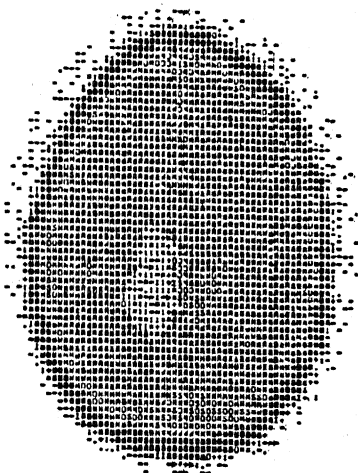
MIN= -2MAX= 2ERAD= 0.245502RAD= 0.245130PIKL= 1332PIKL= 2512GRIN= -2.14064KRAAL= 1.4411ERL= 0.14940KAL= 0.52072

Fig. 5.19 Reconstruction of human brain with SINC window for (a) $R_c = 16$ (b) $R_c = 32$ and (c) $R_c = 64$

[illegible][illegible]

NAME = JAMES ZERRON = 0.326538400 = 0.36744041000 = 0.333071000 = 0.612000000 = 0.60117100000 = 0.60117100000 = 0.649700000 = 0.60371

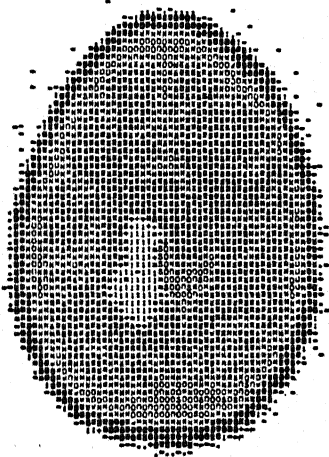
Fig. 5.20 Reconstruction of human brain with H80 window for (a) $R_C=16$ (b) $R_C=32$ and (c) $R_C=64$



(a)

R10= -12R10= 12R20R1= 1.70664CR000= 1.94020R1ZEL= 3320P1ZEL= 25120R10= -11.60730CR000= 14.10661ZEL1= 1.97173R2L2= 2.70371

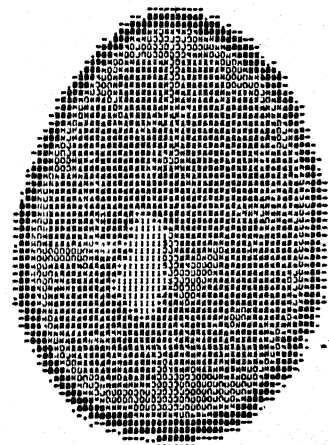
04/19/257.64 F6406 CODED PICTUREPIC= 640PIC= 640ANGLE= 1000RAT= 640R= 3180 JICRA1100Tq10P0100=01FAP0P0KCT010.00000



(b)

R10= -0R10= 0R20R1= 0.04470P1ZEL= 3320P1ZEL= 25120R10= -0.02050CR000= 0.04000ZEL1= 1.01000R2L2= 1.40007

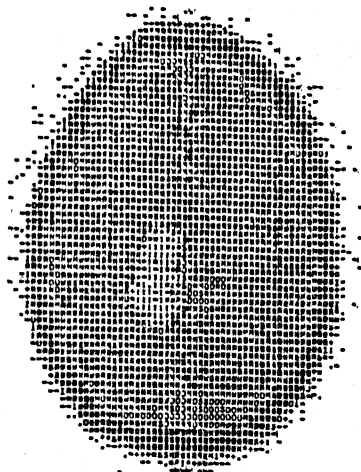
04/19/257.64 F6406 CODED PICTUREPIC= 640PIC= 640ANGLE= 1000RAT= 640R= 3180 JICRA1100Tq10P0100=01FAP0P0KCT010.00000



(c)

R10= -3R10= 3R20R1= 0.40540CR000= 0.40700P1ZEL= 3320P1ZEL= 25120R10= -2.91600CR000= 4.70667ZEL1= 0.00500R2L2= 0.77094

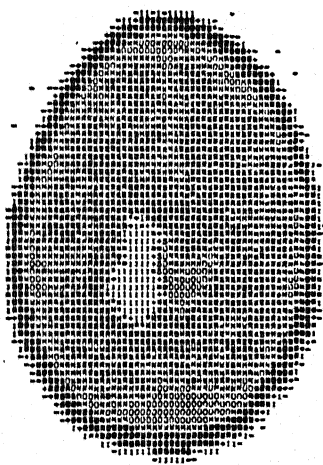
Fig. 5.21 Reconstruction of human brain with H75 window for (a) $R_c = 16$ (b) $R_c = 32$ and (c) $R_c = 64$



(a)

#100 =14NAK=14ENH004=2.37092E+004=2.61544E+012E=33004012E=2012ENH20=14.00411ENH44=14.06712E+14=2.64191ENH20=3.75035

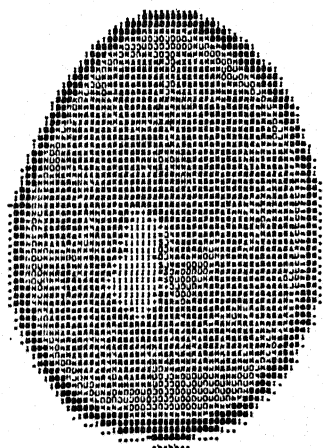
NAME/257.64 P64K64 CODED PICTUREPIC= 64NPIC= 64NANGLE= 2006RAY= 120P= 3K6= JICR1780RT001U0001U00017F0000P00CUT=10,00000



(b)

MIN= -0.986X MAX= 0.986X CORR= 1.24370CRRD= 1.39650MPXL= 3332MPXL= 2912ERTH= -0.21041KPMIN 8.46784KRL= 1.45302ECLZ= 2.30470

NAND6/25J.04 P64664 CODED PICTUREMPIC 64NPIC 64NANGLN 688URATN 256Kps 3KB JI2R118URTnSIdPn0IND=017SPnPGRCTT=10.9C000



(c)

NAME = 4NAME 4CNAME 0.00074CNAME 0.07306PIXEL 3333NAME 2512NAME -4.00795CNAME 0.00204NAME 0.74045NAME 1.17176

Fig. 5.23 Reconstruction of human brain with H 54 window
for (a) $R_c=16$ (b) $R_c=32$ and (c) $R_c=64$

Table 5.6 : Summary of Errors in the Reconstruction of Human-brain

Window	$ W''(0) $	R_c	ERMIN	ERMAX	ERL1	ERL2	\bar{E}
H99	0.001	16	-8.8861	10.0679	1.6069	2.1657	1.335
		32	-3.4002	4.9296	0.5692	0.7727	0.425
		64	-1.5447	1.3435	0.2434	0.3427	0.125
H91	0.083	16	-9.8087	10.7707	1.6502	2.2724	1.429
		32	-4.2567	5.6034	0.6954	0.9841	0.554
		64	-1.9996	1.8182	0.3227	0.4758	0.217
Sinc	0.083	16	-10.5285	11.0821	1.6687	2.3344	1.456
		32	-4.5592	5.7841	0.7415	1.0638	0.599
		64	-2.1203	1.9481	0.3494	0.5207	0.245
H80	0.200	16	-11.1108	11.7627	1.8484	2.5974	1.649
		32	-5.4923	6.5545	0.9110	1.3377	0.758
		64	-2.6415	2.4883	0.4497	0.6837	0.326
H75	0.250	16	-11.6672	12.1866	1.9717	2.7838	1.766
		32	-6.0205	6.9608	1.0109	1.4988	0.842
		64	-2.9160	2.7866	0.5058	0.7759	0.405
Cos	0.250	16	-13.5033	12.9926	2.1896	3.1912	1.966
		32	-6.7961	7.4246	1.1545	1.7360	0.972
		64	-3.2238	3.2013	0.5821	0.9035	0.478
H54	0.460	16	-14.0043	13.9671	2.6419	3.7543	2.370
		32	-8.2384	8.6678	1.4539	2.2042	1.243
		64	-4.0679	4.0828	0.7484	1.1717	0.604

Window	$ w''(0) $	R_C	ERL1N	ERL2N	\overline{EN}
H99	0.001	16	0.0871	0.2575	0.076
		32	0.0308	0.0918	0.024
		64	0.0132	0.0407	0.007
H91	0.083	16	0.0895	0.2702	0.082
		32	0.0377	0.1170	0.031
		64	0.0175	0.0565	0.012
Sinc	0.083	16	0.0905	0.2775	0.083
		32	0.0402	0.1265	0.034
		64	0.0189	0.0619	0.014
H80	0.200	16	0.1002	0.3088	0.095
		32	0.0494	0.1590	0.043
		64	0.0243	0.0813	0.018
H75	0.250	16	0.1069	0.3310	0.101
		32	0.0548	0.1782	0.048
		64	0.0274	0.0922	0.023
Cos	0.250	16	0.1187	0.3794	0.113
		32	0.0626	0.2064	0.056
		64	0.0315	0.1074	0.027
H54	0.460	16	0.1433	0.4469	0.136
		32	0.0788	0.2621	0.071
		64	0.0406	0.1393	0.034

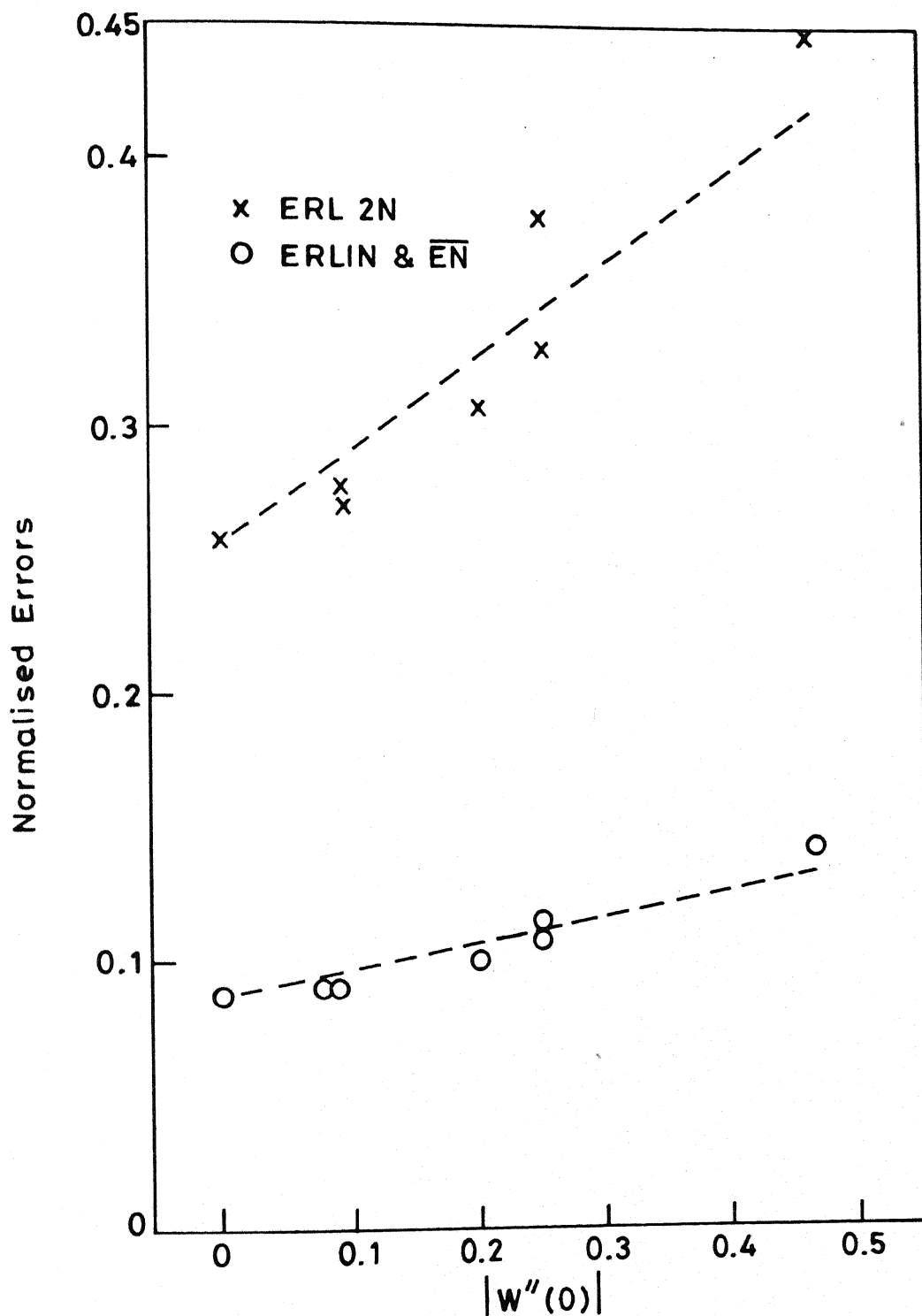


Fig. 5.24 Comparative performance (on brain) of Various windows for $R_c = 16$

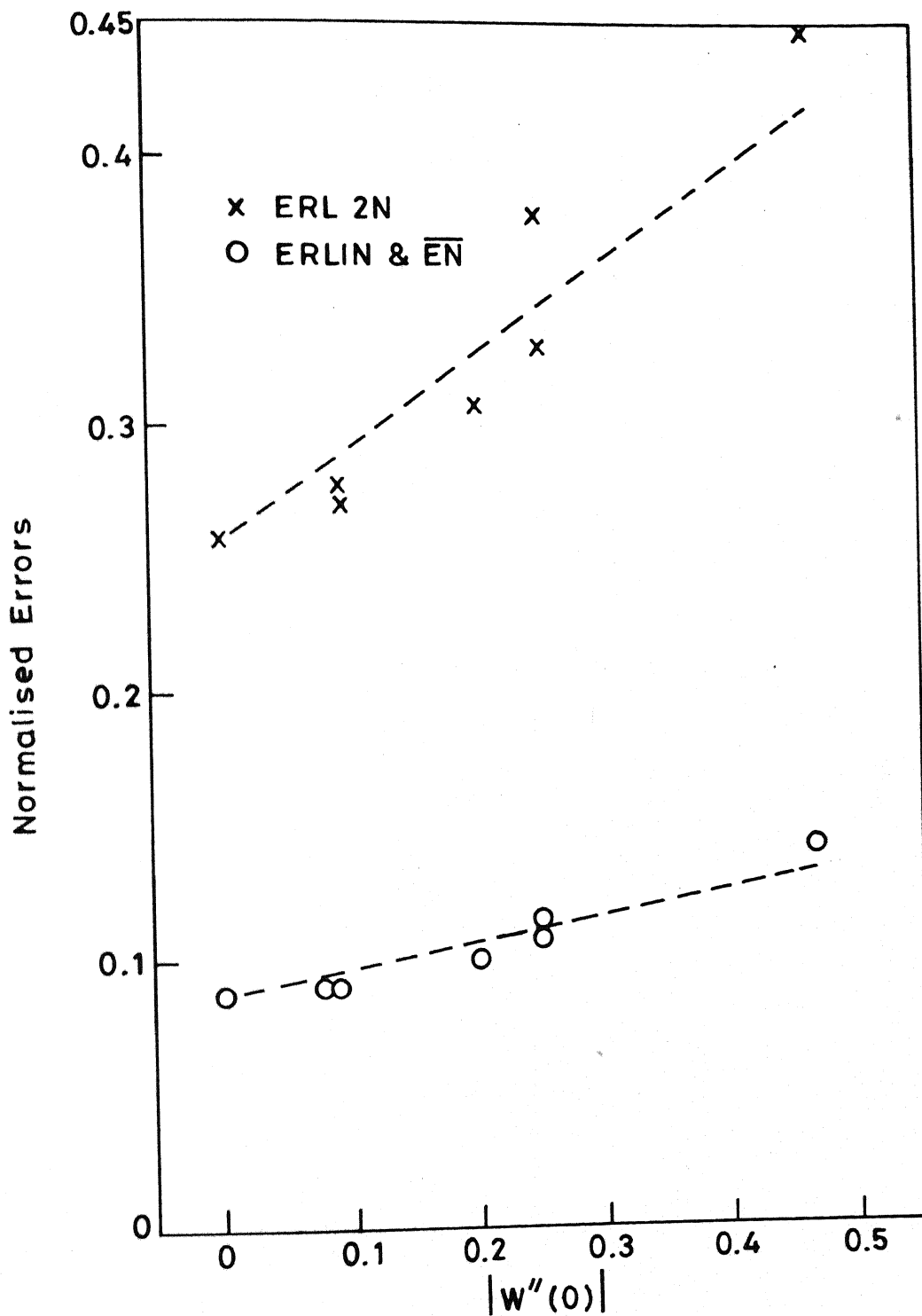


Fig. 5.24 Comparative performance (on brain) of Various windows for $R_c = 16$

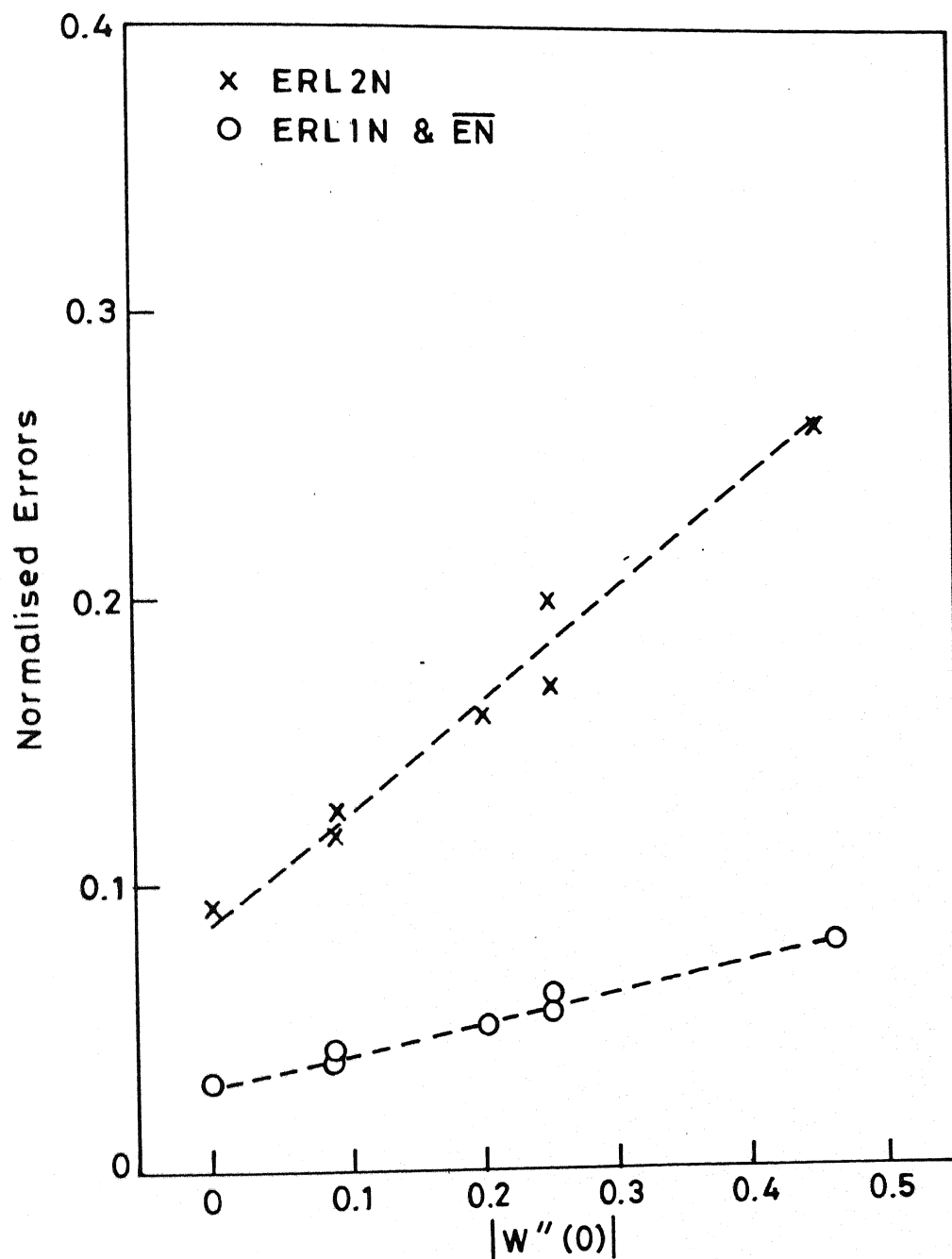


Fig. 5.25 Comparative performance (on brain) of various windows for $R_c = 32$.

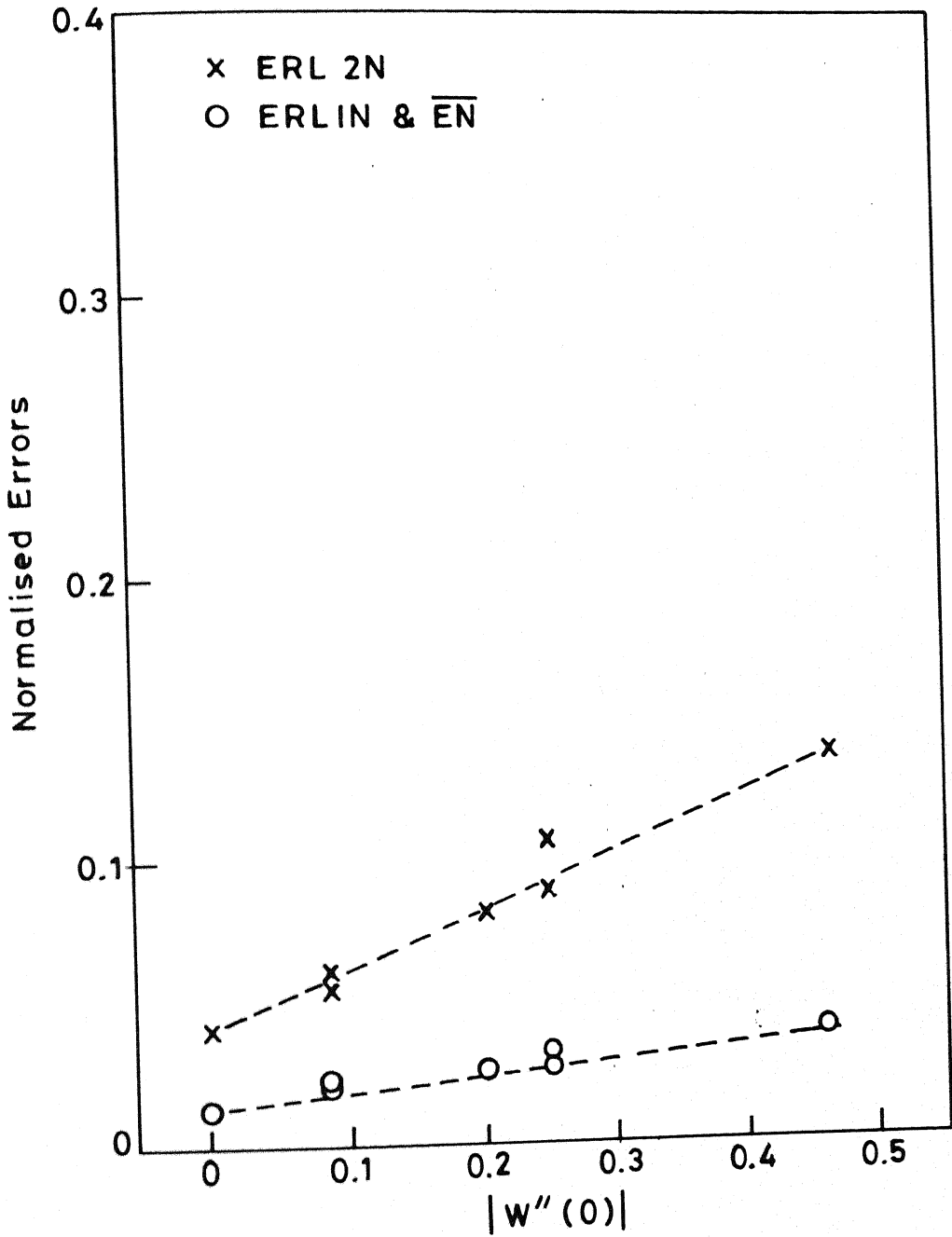


Fig. 5.26 Comparative performance (on brain) of various windows for $R_c = 64$.

CHAPTER 6

DISCUSSION

The major results of the thesis are reflected in the,

- (a) ω_c -Estimate, Section (3.3)
- (b) Asymptotic formula, Section (3.4), and
- (c) Inverse Theorem, Section (4.2).

The ω_c -estimate states that any uniformly continuous cross section f can be reconstructed to within accuracy which is at least $O(\omega_c(f^{[0]}; 1/R_c))$ as under the continuity assumption $\omega_c(f^{[0]}; \delta) \rightarrow 0$ as $\delta \rightarrow 0$. It further follows that the smoother features of the cross section are amenable to a better reconstruction. Thus, sub-regions of the cross section which are sufficiently smooth, will get reconstructed well, while the sub-regions possessing discontinuities (edges) will tend to have large reconstruction errors.

The asymptotic formula predicts the point-wise error, e_R , arising due to the band-limiting aspect of the CBP implementation. For commonly used windows, $W(R)$, e.g., sinc, cosine, and generalized hamming, we have,

$$|W'(0)| = 0, \text{ and} \\ |W''(0)| \neq 0,$$

indicating the value of m to be 1 for analysis purposes. For a fixed R_C , the asymptotic formula then implies that the pointwise e_R is proportional to $|w''(0)|$ provided R_C is sufficiently large and the second order RADAV derivatives (of the cross section) exist the point under consideration. Furthermore, for the windows considered in this study, the best e_R -error order that can be obtained is $O(1/R_C^2)$.

The Inverse theorem states that the closeness, $O(R_C^{-\beta})$, of the reconstruction to the original image belonging to the class Ω_{2m}^β cannot be improved by the CBP algorithm no matter what filter from the class IK_{2m} is used.

We note that the total reconstruction error, e_T , at a point comprises of three components, e_R , e_C and e_B . Since the composite trapezoidal approximation converges to the true value of the integral (of a Riemann integrable function) as the step-size approaches zero, for a smooth cross section, the discretization errors e_C , and $e_B \rightarrow 0$ as the number of rays and views are increased. The error in the composite trapezoidal rule, E_{TR} , for a function g , is given by,

$$E_{TR} = - \frac{b-a}{12} h^2 g''(\eta) , \quad a < \eta < b .$$

Here h is the stepsize and g is twice differentiable on $[a, b]$. Hence,

$$e_C \propto (\Delta s)^2,$$

and

$$e_B \propto (\Delta \theta)^2.$$

When the sampling and the optimality conditions are satisfied, i.e.,

$$R_C = \frac{1}{2\Delta s},$$

$$\text{and, } N_{\text{VIEW}} = \frac{(N_{\text{RAY}} - 1)\pi}{2}$$

then,

$$e_C \propto (1/R_C^2)$$

$$\text{and, } e_B \propto (1/R_C^2).$$

Hence, for $f \in \Omega_2^\beta$, $0 < \beta < 2$, if the projection data p is sufficiently smooth the total pointwise error will be dominated by the inherent error, e_R , i.e.,

$$e_T \sim e_R = O(R_C^{-\beta}).$$

It may be noted that, generally for the cross sections, f , of interest, their projection data p , being the set of line integrals of f , would be smoother than f .

6.2 The Asymptotic Formula

The results summarised in Figs.(5.13)-(5.15) and Figs.(5.24)-(5.26) reveal that, for a fixed R_c , the errors $ERL1N$, $ERL2N$, and \overline{EN} are large for windows having large magnitudes of $W''(0)$. Hence, the performance of the windows is in accordance with their corresponding values of $W''(0)$, as predicted by Theorem (3.4). The sequential ranking of the windows as per their $|W''(0)|$ is,

$$H99 < H91, \quad SINC < H80 < H75, \quad COS < H54,$$

and the errors $ERL1N$, $ERL2N$, and \overline{EN} are in the order,

$$H99 < H91 < SINC < H80 < H75 < COS < H54.$$

Figures (5.13)-(5.15) and Figs.(5.24)-(5.26) also reveal that the errors increase (approx.) linearly with $|W''(0)|$.

The reconstruction results reported by Herman [1] for different windows also agree with the predictions of the asymptotic formula, i.e., the error in reconstruction is in accordance with the magnitude of $W''(0)$ of the windows (See Appendix C).

6.2 The ω_c -Estimate

A comparative study of the results for the image of the human-brain and the NFB image, shows that all the errors measures for the brain cross section are much less

compared to those for the NFB cross-section. The inherent nature of the digitization is same for both the images, yet there is a marked difference in the magnitude of all the corresponding error measures for the human-brain and the NFB. This is because the proportion of smooth sub-regions is higher in the brain than that in the NFB image. The e_R error decreases as a direct consequence of Theorem (3.3), subsequently reducing the overall errors according to $O(\omega_c(f^{[1]}; 1/R_c)) = O(1/R_c)$.

6.3 The Inverse Theorem

For the windows chosen in the study, m takes the value 1, indicating the applicability of the inverse theorem for the range $(0,2)$ of β . The varying- R_c experiments indicate that the overall error reduces in a linear fashion for both the cases of the NFB and the brain images. Though, only three cases of R_c were considered due to the CPU time limitation, it is reasonable to assume that e_T is $O(1/R_c)$. We know that the composite trapezoidal approximation ensures negligible e_B , and e_C for sufficiently large NRAY and NVIEW. In such a case, the discretization errors would be comparatively negligible and then e_T will be dominated by e_R . It has been observed that the order of e_T is $O(1/R_c)$ for both the images. It appears that the discretized images considered in this study belong to the class Ω_{2m}^β , with β taking the

value approximately 1.

It is interesting to note that the overall reconstruction errors , $ERL1N$, $ERL2N$ and \overline{EN} , for a head phantom reported by Herman [1], also depict an order of $O(1/R_c)$ (See Appendix C).

APPENDIX A

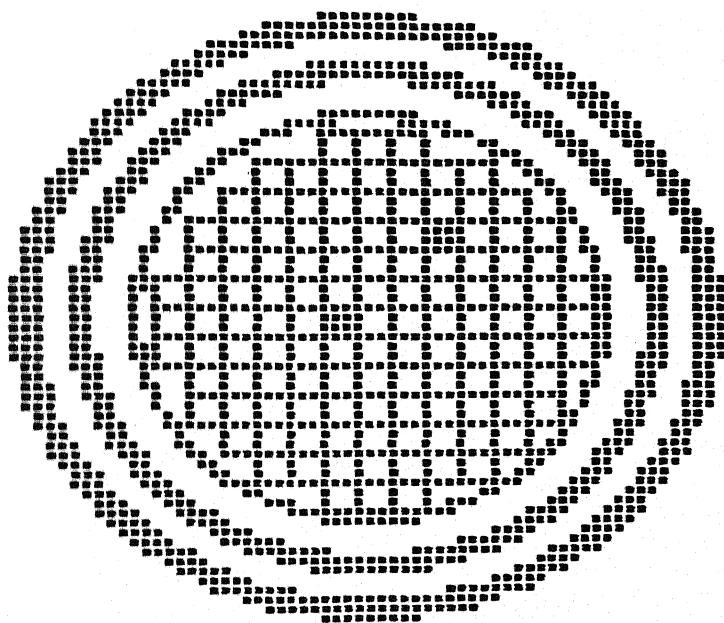
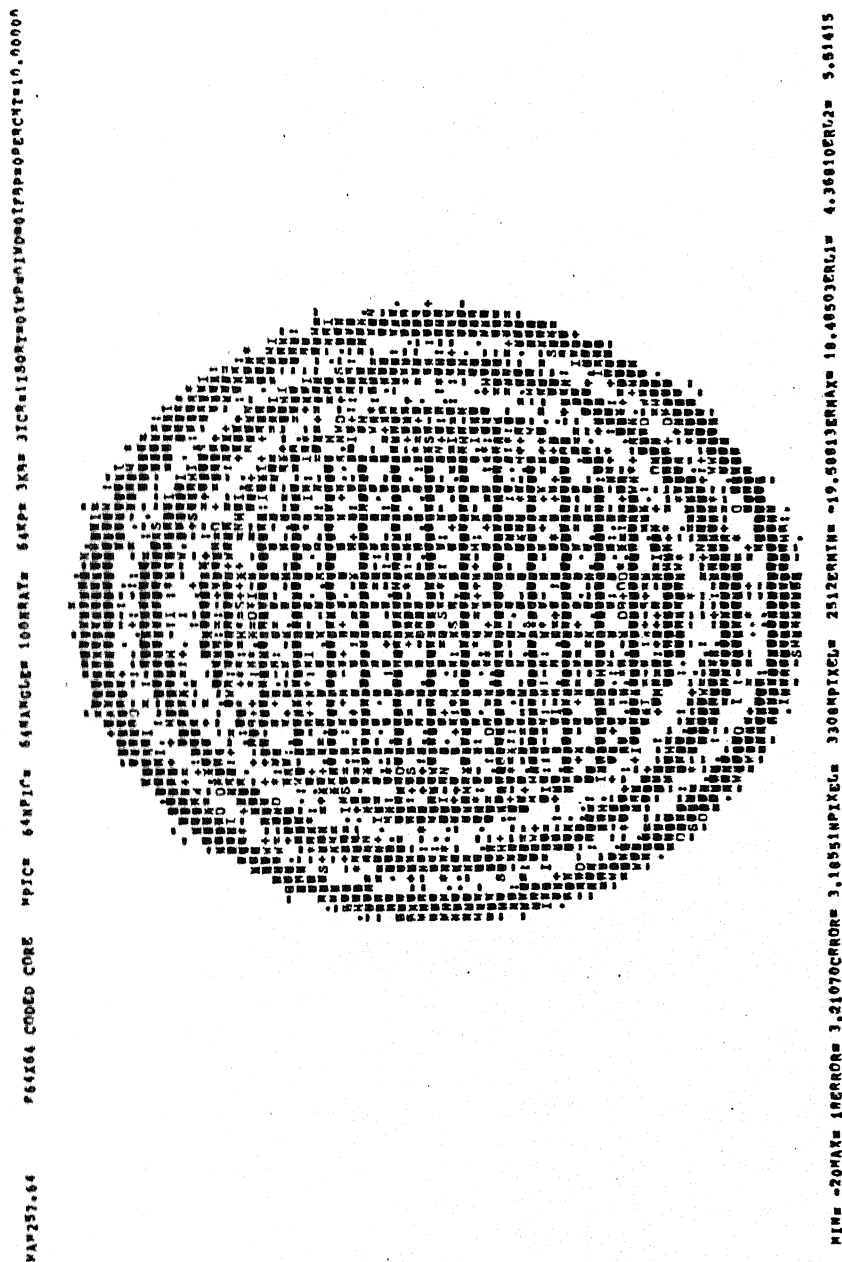
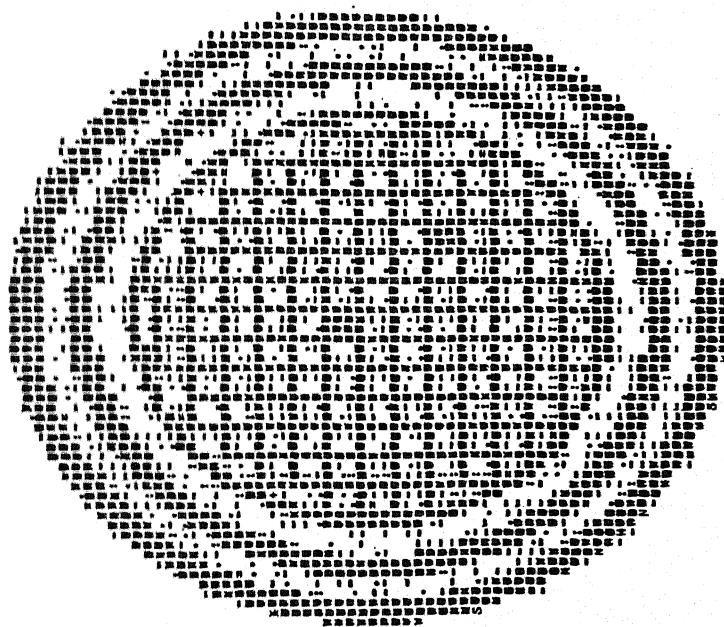


Fig. A-5.5 : Computer Output.

All figures in Appendix A correspond to
Fig. (5.5) - (5.12) of the main text.



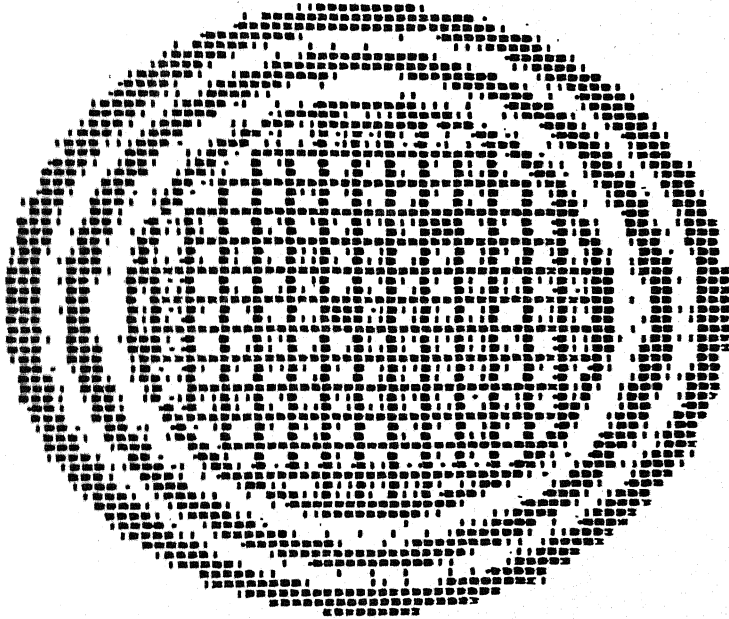
MAY257.64 F164X64 CONEO CONE MPIC= 64NPIC 64HANGLE= 200HAYE 128KP= 3KSW 3ICR=1150RT=01VP=01VD=01FP=00PCRCNT=10.00000



MIN= -0MAX= 4ERROR= 1.38986CHRON= 1.38933NPICEL= 332MPICEL= 2512ENTIN= -8.103912RMAX= 5.74706ERUJ= 1.69406PAU2= 2.12619

Fig. A-5.6(b) - Computer Output.

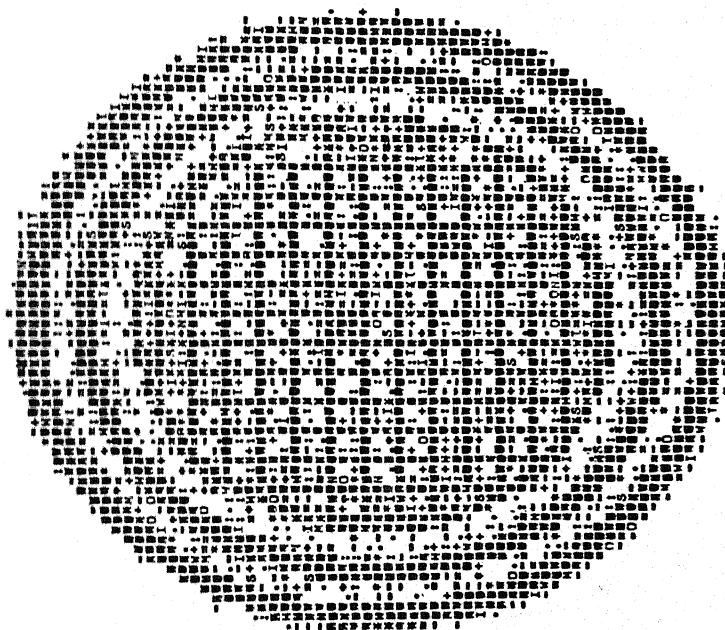
MAX237.64 #164X64 CODED CORE NPIC= 64NPIC= 640000 JESB 31CRA1150RT=01VP=01UD=01F8P=00PRCMT=10.00000



MIN= -4.9416 3ERR0R= 0.65936CRR0R= 0.61023NPICEL= 3332NPICEL= 2512ERRATE= -3.94324ERRATE= 3.03056ERRU= 0.76591ERRU= 0.98648

Fig. A-5.6(c) - Computer Output.

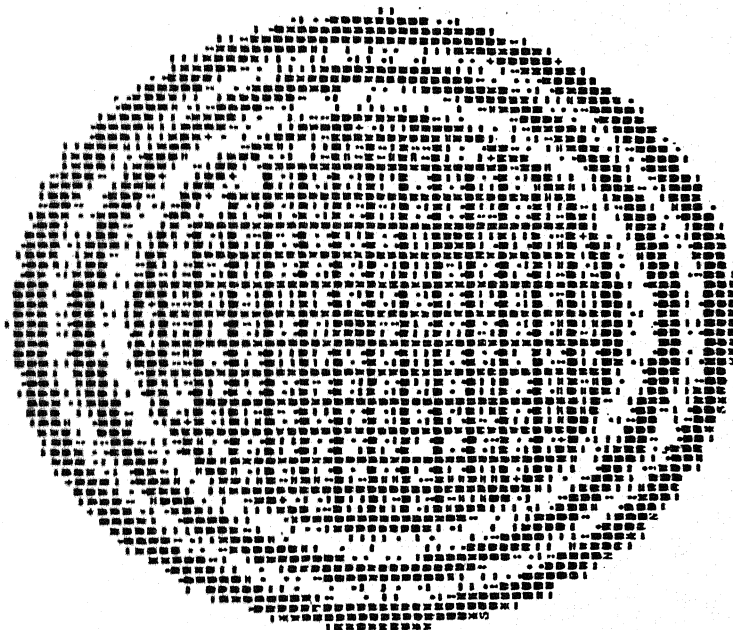
NA917/23.64 764164 CODED CORE *PIC 64PICS 64WACLES 100WAC 64CM 3KM 31CM 150RT=01W=01V=01P=01R=01E=01C=10.00000



MIN=-19MAX=18ERROR=3.8815CRNR=3.95920MPXEL=3300MPXEL=2412ENTH=-18.86288RMAX=17.60057ERL=4.96001ERL2=5.67038

Fig. A-5.7(a) - Computer Output.

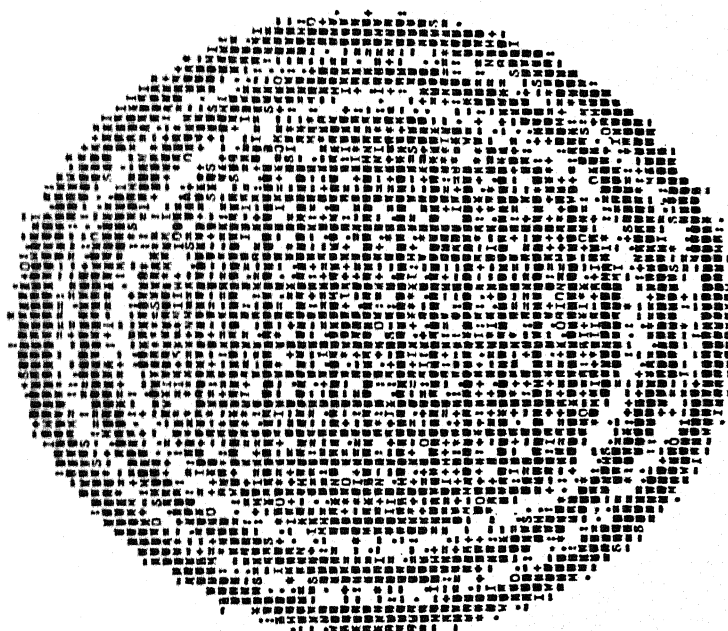
MA=917/257.64 F64X64 CODED CORE MPIC= 64NPIC= 64ANGLE= 200NAY= 128KPE 3K8= 31CM=150QT=01uP=01V=01FAP=0PERCT=10.00000



MIN= -8MAX= 7ERROR= 2.00000CPROR= 7.06011NPIC= 64 332NPIC= 64 2512ERRIN= -8.40708ERRMAX= 6.78098ERRMIN= 2.23633ERRI2= 2.65346

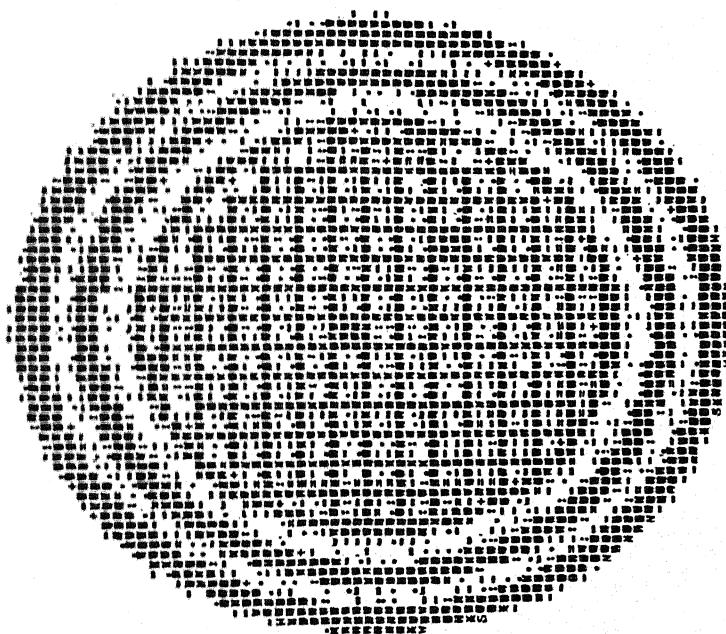
Fig. A-5.7(b) - Computer Output.

BNP_SAMPLING F16X64 CODED CORE MPIC= 64NPIC= 64NANGLE= 100NRYA 64K= 368 31Cr=1150RT=61Vp=61Vb=01F8P=0P2RCNT=10,00000



MIN= -18MAX= 17ERROR= 4.26270CROR= 4.39490NPIC= 330NPICL= 2512ERRIN= -10,16720ENAX= 17.42198ENLI= 4.82390ENL2= 5.88371

Fig. A-5.8(a) - Computer Output.



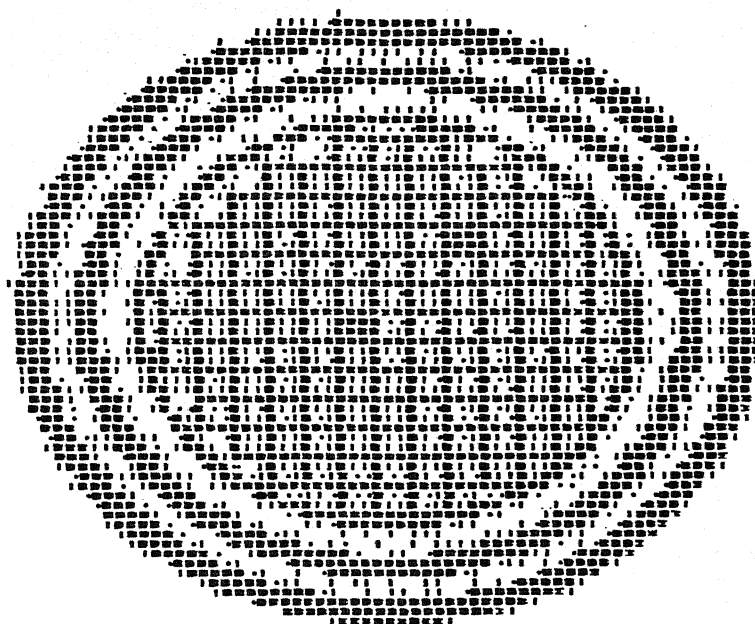
```

MIN=-9MAX=7ERROR=2.20424NPIXEL=3332NPIXEL=2512ERMIN=-8.5376ERMAX=7.1479SERL=2.43373ERL2=2.05226

```

Fig. A-5.8 (b) - Computer Output.

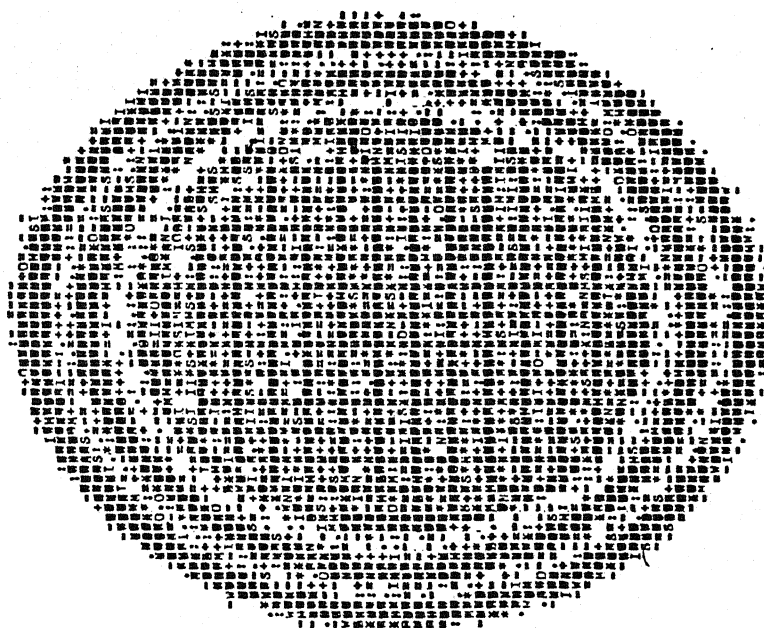
8HP,SAMPLING P144X64 CODED CORE MPIC= 64NPIC= 64NANGL= 400NAYS 256KP= 3KB= 3ICR=150RT=01VP=01ID=01P0P=0PPECNT=10.00000



MIN= -4MAX= 4ERROR= 1.12425CERROR= 1.13416NPIXEL= 3332NPIXEL= 2512CORN= -4.22746ERNAX= 3.66043ERU1= 1.20789ERU2= 1.41232

Fig. A-5.8(c) - Computer Output.

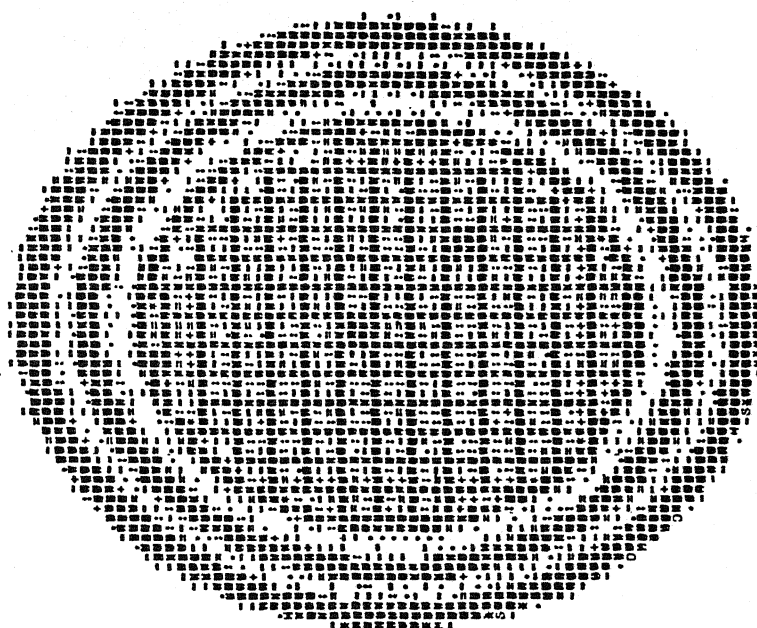
NA489/257.64 P64X64 CNOCD CORE MPIC 64PIC= 64*ANGLE= 100RAY= 64KPS 3KB= 3ICR=11087201P=01INDP=01PSP=0PCCT=10.00000



MIN= -18MAX= 17ERROR= 5.20949CNROR= 5.45422MPIXEL= 3308MPIXEL= 2512PNTN= -17.85631ERMAX= 16.53348PRG1= 5.61436PRG2= 6.57627

Fig. A-5.9(a) - Computer Output.

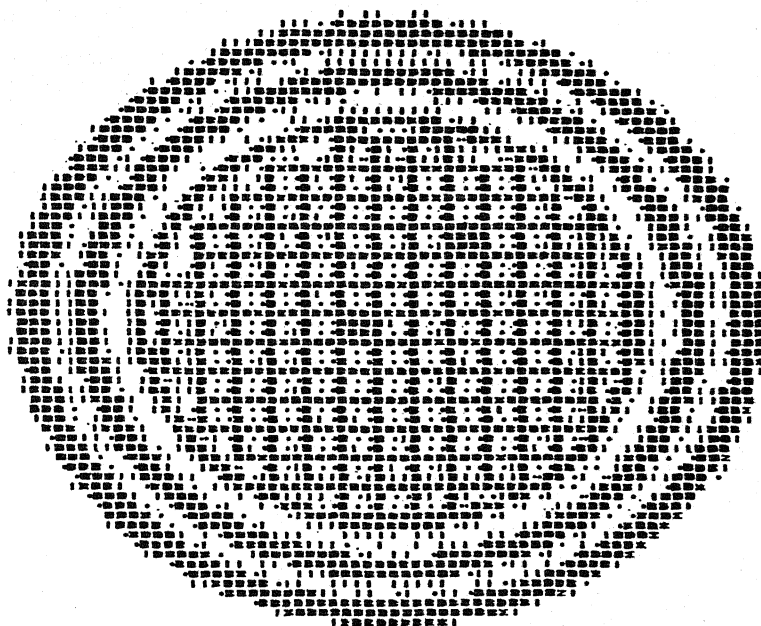
NA8M/257.64 F6AK4 CODED CORE WPC= 64NPI= 64XANGLE= 200RAY= 128K= 3K= 3IC=ISORT=0INP=0IND=0IFSP=0PERCUT=10.00000



WLM= -9MAX= MEKRON= 2.91597CMRUR= 3.0716JMPIGL= 33JMPIGL= 2512EMIN= -0.056508RMAX= 0.47933ERUJ= 3.18402FUC2= 3.61637

Fig. A-5.9(b) - Computer Output

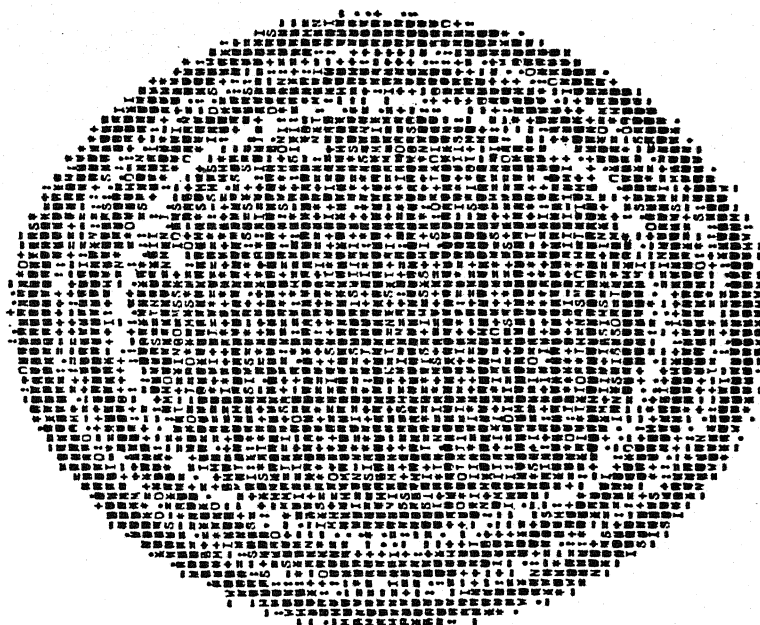
H4489/257.64 P64X64 CODED CORE MPTC= 64NPIC= 64RANGC= 400RAY= 256KPS 3K= 3ICP=1180RT=01VP=01V0=0178P=0P2CWT=10.00000



MIN= -5MAX= 4ERROR= 1.61231CROR= 1.55334NPIC= 332NPICL= 2512ERRIN= -4.62704ERRMAX= 4.37893ERRLI= 1.62440ERRU2= 1.69046

Fig. A-5.9(c) - Computer Output.

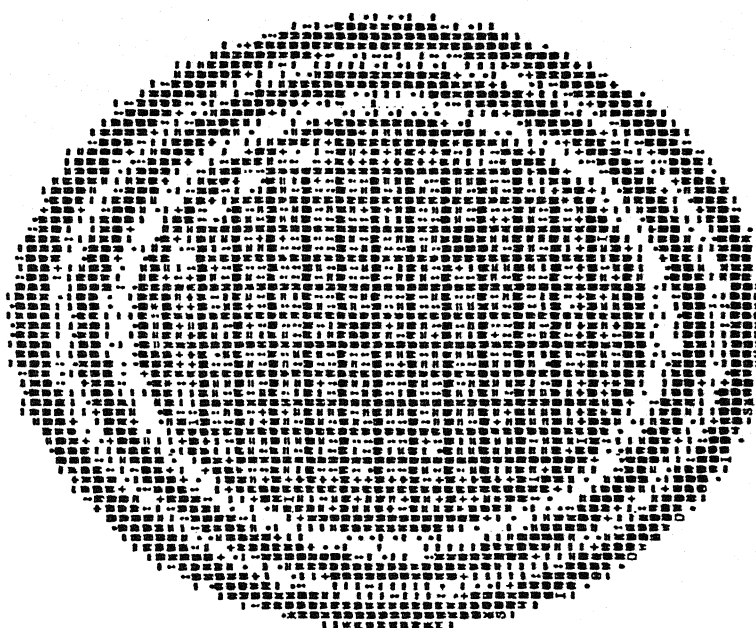
HAFT5/237.64 P64X64 CODED CORE MPIC= 64NPIC= 64NANGLES 100NPAY= 64NP= 3KN= 37CR=150RT=0TP=0IND=0IFAP=0PERCMT=10.00000



MPIC= 64NPIC= 64NANGLES 100NPAY= 64NP= 3KN= 37CR=150RT=0TP=0IND=0IFAP=0PERCMT=10.00000

Fig. A-5.10(a) - Computer Output.

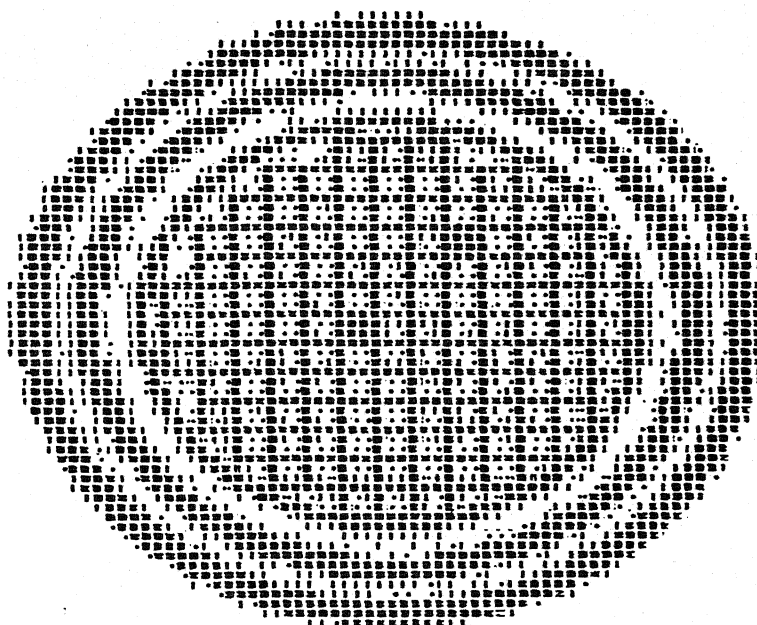
MAN75/257.64 F64X64 CODED CORE MPIC= 64NPIC= 64NANGUE= 200NAT= 128KP= 3KB 3YCR=1150RT=01UP=01ND=01AP=0PERCNT=10.00000



MIN= -10MAX= 9ERROR= 1.3103CRUR= 3.53424NPICU= 1332NPICL= 2512ERRIN= -0.63417ERRAX= 9.20502ERLU= 3.59045ERLU2= 4.06759

Fig. A-5.10(b) - Computer Output.

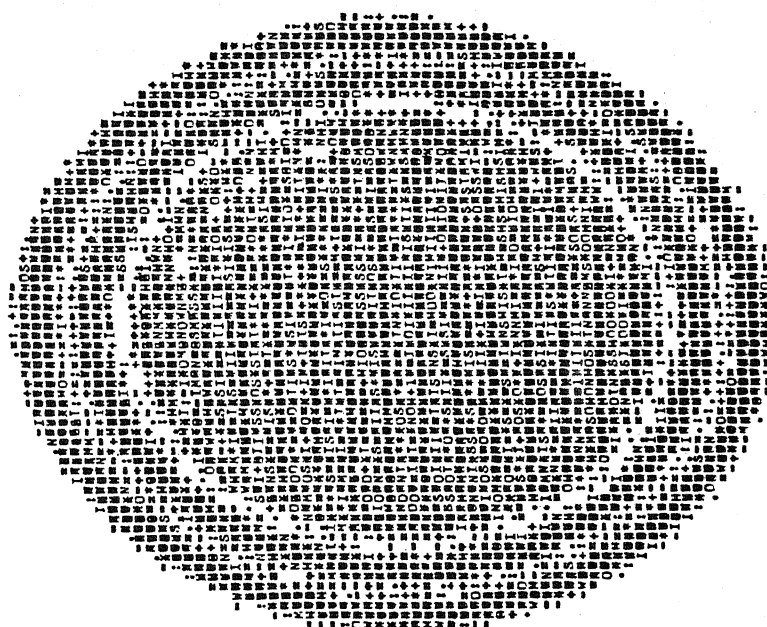
MAR/2/25/64 F54X04 CODED CURE MPIC= 64NPIC= 40UNWAY 256CP JKB= JICR=IISONW=OIMP=OIWD=OIFSP=OFCMC=TT=10.00000



MIN= -5MAX= 5ERRUN= 1.73109CKRUR= 1.7985/NPIAEU 332NPICU= 251ZERNIN= -4.8322ERNAX= 4.7669PIERU= 1.8597ZERU2= 2.10523

Fig. A-5.10(c) - Computer Output.

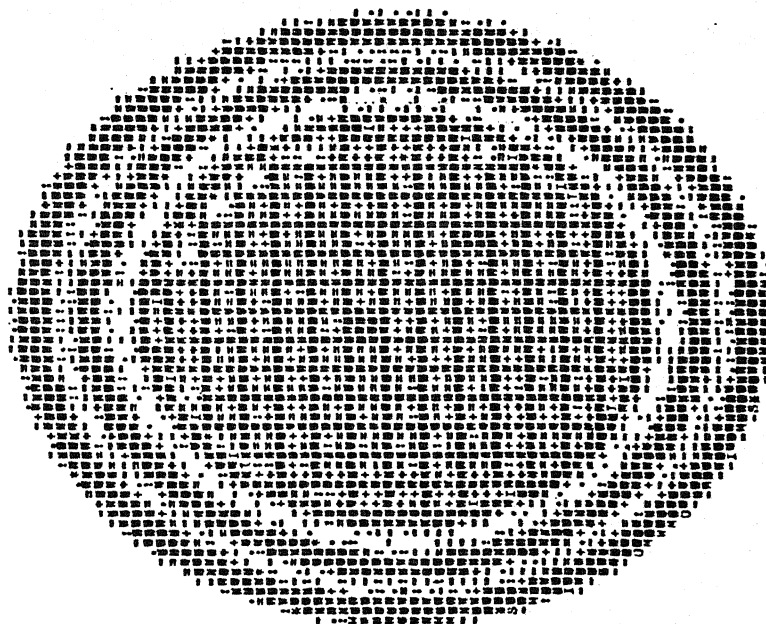
CO5257.64 P64164 CODED CORE PCIC 64NPIC 64MANULES 100NPAY 64PP= 31CRJ180RT01WPS01WDS01FRP=0PFCY=10.00000



MIN= -19MAX= 18ERROR= 7.14782CROR= 7.65844NPIC= 3308NPIC= 2512ENH= -19.2088ERRAX= 17.9843ERRU= 7.70378ERRU= 8.55249

Fig. A-5.11(a) - Computer Output.

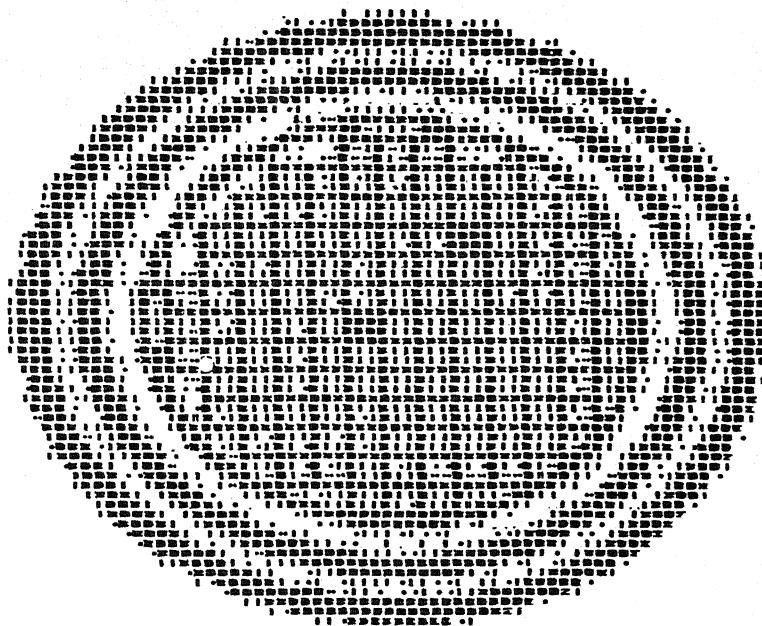
C08257.64
 P64X64 CODED CORE
 NPIC= 64NPIC= 64HANGLE= 30HRY= 12MP= 3KM= 3ICRAISORT=0INP=0IND=0IFAP=OPERCNT=10.0000



MIN= -51MAX= 10ERROR= 1.98235CRROR= 4.12810NPICU= 332MPICU= 2512ENHNT= -10.58019ERRMAX= 10.14946ERRU= 4.17009ERRU2= 4.68385

Fig. A-5.11(b) - Computer Output.

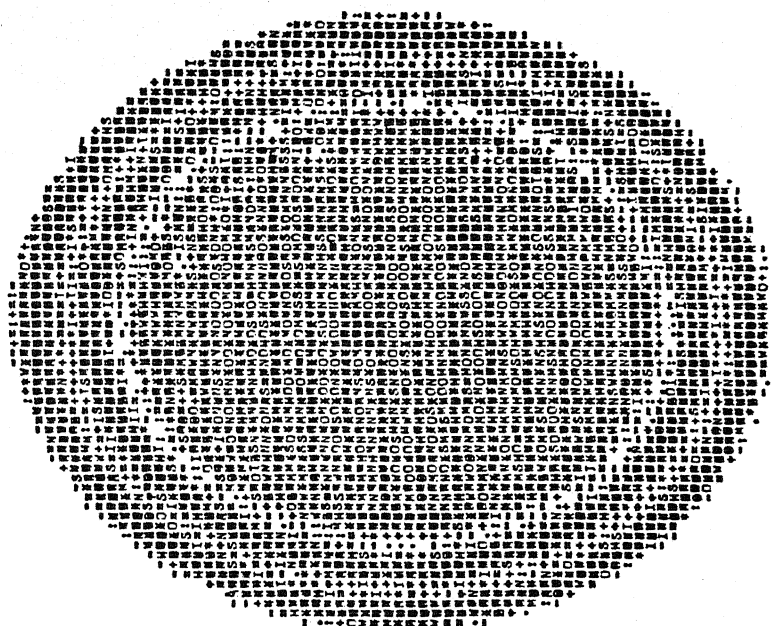
CDS257.64 P64X64 CODED CORR MPTC= 64NPTC= 64NANGLE= 400NAY= 256PZ= 3K8= 3TCRA180RT=01UP=01VD=01PD=0PESCWT=10.00000



MIN= -5NAX= 5ERROR= 2.06092CRROR= 2.17118MPXEL= 3332MPXEL= 2512ERRATM= -5.05733ENAX= 5.25324ENGL= 2.18777ERL2= 2.46077

Fig. A-5.11(c) - Computer Output.

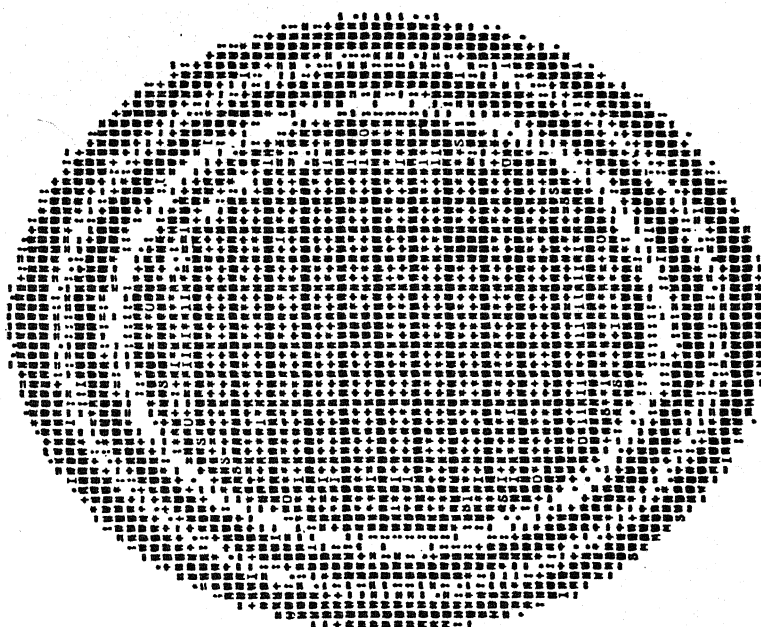
MAN54/257.64 F6X64 CODED CURE *PIC= 64NPIC= 64RANGE= 100RAY= 64RPS 3KR= 3ICR=180RT=0IMP=0IVD=0IPRP=0PXC=1IC=00000



MIN= -20MAX= 100ERROR= 8.89208CROR= 9.57166NPICXL= 330NPICXL= 2512ENIN= -20.2559RCRMAX= 18.60337ERLJ= 9.56741PRC= 10.20071

Fig. A-5.12(a) - Computer Output.

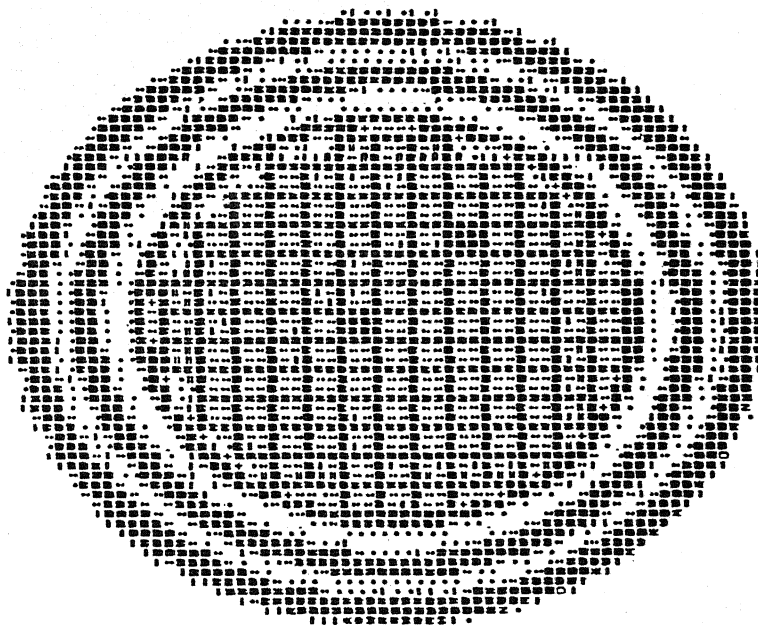
NAWS4/257.64 P64X64 CODED CORR NPIC= 64NPIC= 64NANGLE= 200NAY= 128KP= 3K= 3ICRAISOFT=0IUP=0IUD=0IAP=0PRT=10.00000



MIN= -12MAX= 12ERRUN= 5.07561CHRUN= 5.46775NPIAG= 332NPICEL= 2512ERRIN= -12.04987ERRAN= 12.25142ERRU= 5.47620ERRU2= 6.07510

Fig. A-5.12(b) - Computer Output.

MAN54/257.64 F164164 CODED CONE MPIC= 64NPIC= 64HANGLE= 400NAY= 756RP= 3R= 3ICR=150RT=0IVP=0IWD=0IFP=OPERCMT=10.00000



MIN= -6MAX= 62NROR= 2.7211VCRUR= 2.8055NPICL= 332MPICL= 2912ERNIN= -6.15657ERNAX= 6.41981ERNLI= 2.87410RNK2= 3.22376

Fig. A-5.12(c) - Computer Output.

APPENDIX B

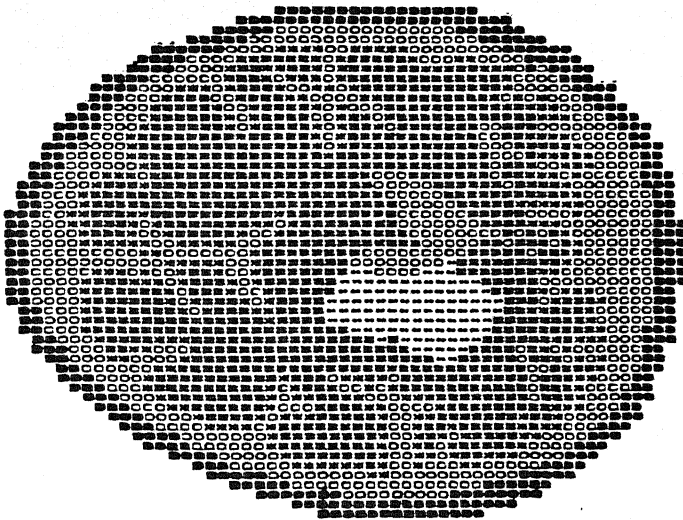
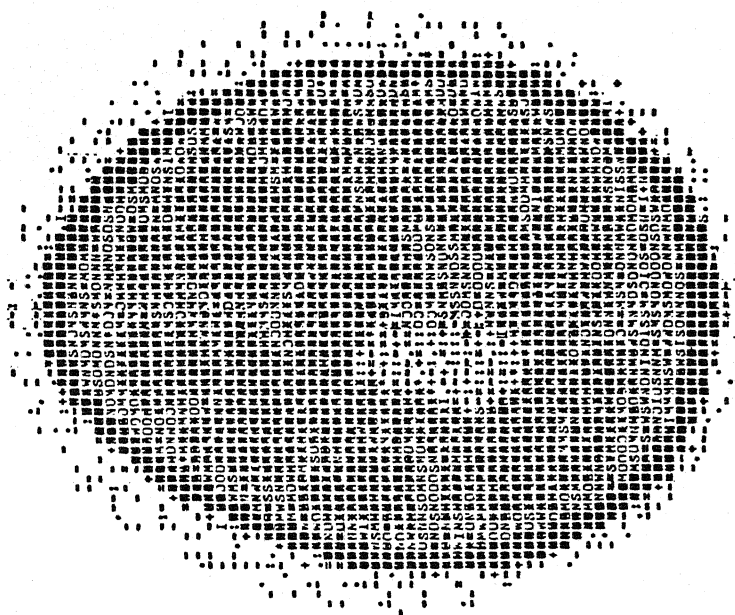


Fig. B-5.16 - Computer Output.

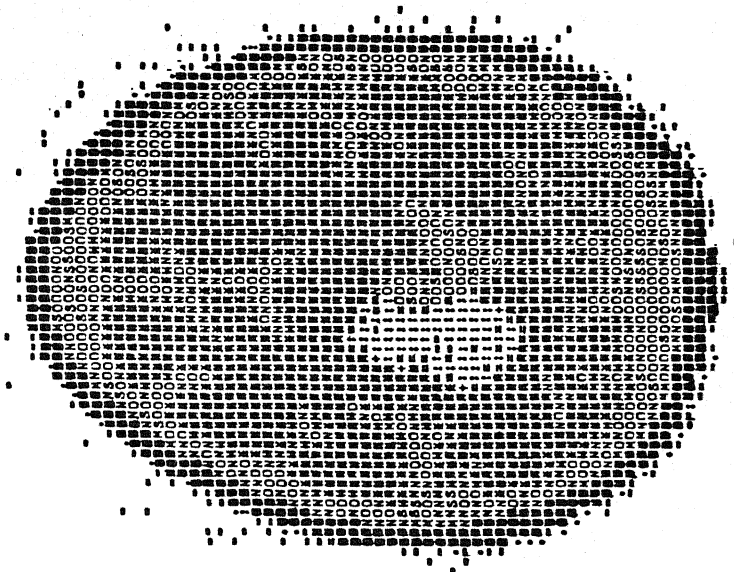
NAN999/257.65 FCTJ64X64 CODED PICTUREMPIC# 64NPIC# 64NANGLE# 100NAY# 64KPE 3K8# 315N#1150NT#01NP#01ND#01PB#0PERCENT#10.00000



MIN# -9MAX# 10ERRDN# 1.31555CRRUR# 1.48527NDPIEL# 330JMPIEL# 251ZERMIN# -8.86612ERMAX# 10.06790ERL# 1.00699ERU2# 2.16578

Fig. B-5.17(a) -Computer Output

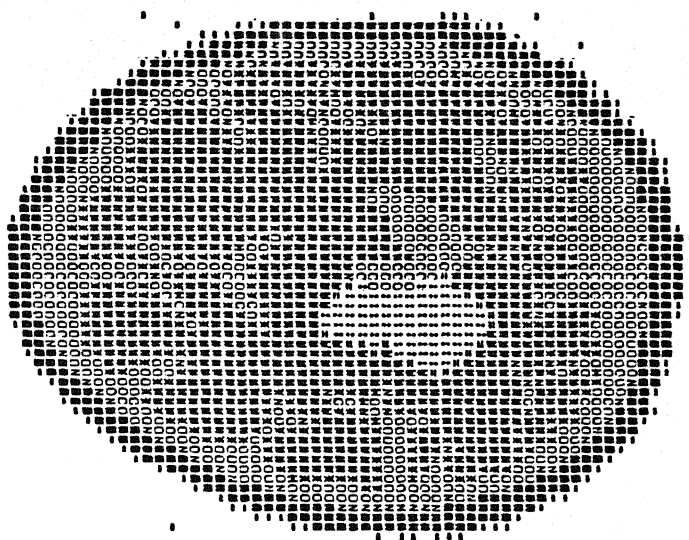
MAN9099/257.65 F64X64 CODED PICTURENPIC= 64NPIC= 64NANGLE= 200NRAY= 128KPE 3KB= 3ICR=156RT=0INP=0IND=0TFBP=0PERCNT=10.00000



MINQ -3MAX= 5ERROR= 0.43557CROBW 0.48049PIXELW 3332PIXELH 2512ERMIN -3.40023ERMAX= 4.92668ERU= 0.46921ERLU= 0.77276

Fig. B-5.17(b) - Computer Output.

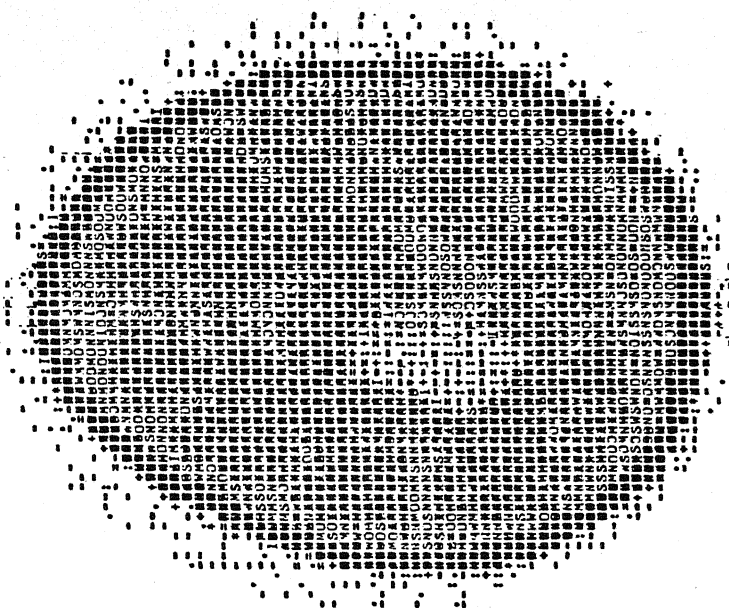
HAN999/237.65 F64A4 CODED PICTUREPIC= 64NPIC= 64NANGLE= 400NRAZ= 256KP= 3KB= JICR211SURCOTHP=0IND=0IFBP=OPENCMT=10.00000



MIN= -2MAX= 1ERROR= 0.12545CROR= 0.13615NPICEL= 332NPICEL= 251ZERMIN= -1.56479ERMAX= 1.54357ERUJ= 0.84346ERL2= 0.34371

Fig. B-5.17(c) - Computer Output.

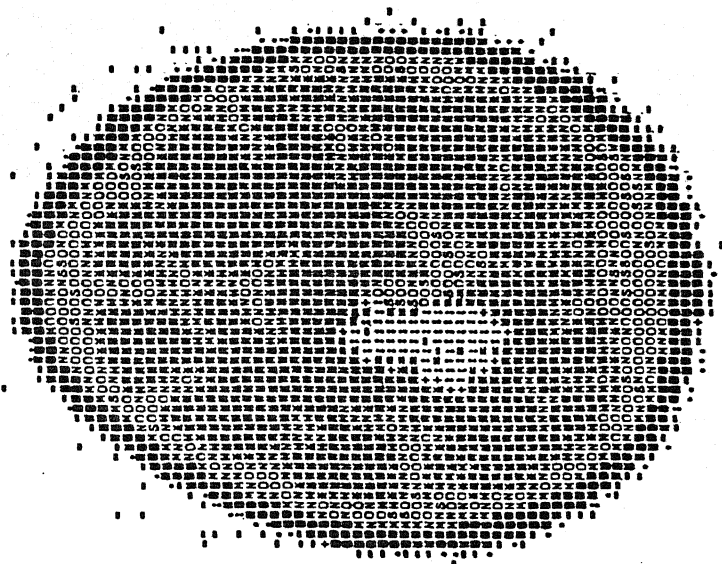
HAHV17/257.64 FCTJ94X64 CODED PICTUREMPIC= 64NPIC= 64ANGLE= 100RAY= 64KPE= 3KPE= 3ICHEL15ONT=01UP=01UD=01FSP=0PERCNT=10.00000



MIN= -10MAX= 11ERRDN= 1.42926CRRUN= 1.57604MPICEL= 330JMPICEL= 2512RMIN= -9.80873URMAX= 10.77074URL= 1.45026EALJ= 2.27247

Fig. B-5.18(a) - Computer Output

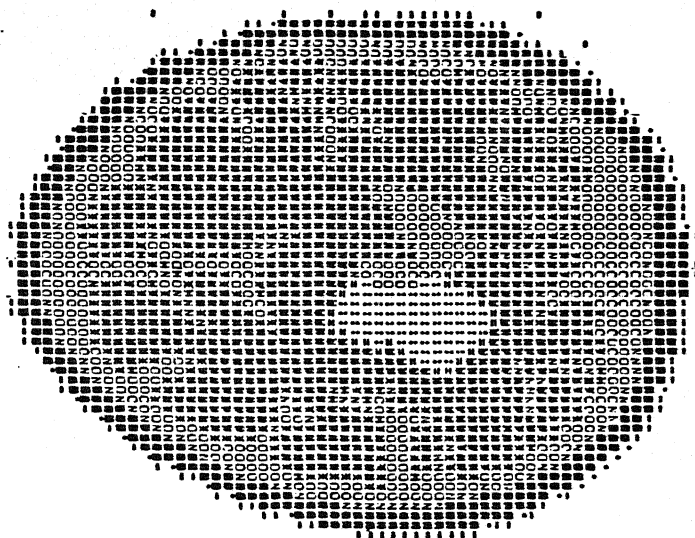
NAME=17/257.64 F64164 CODED PICTUREPIC= 64NPIC= 64NANGLE= 200NRAY= 128KPM= 3KPM= 3ICRAJISORT=0INP=0IUD=0IFBP=0PERCENT=10.00000



NAME -4MAX= 6ERR= 0.55432CHRON= 0.62301NPICUM 332NPICUM 2512ENIN= -4.05675ERNAX= 5.60347ERLI= 0.49548ERLJ= 0.98616

Fig: B-5.18(b) - Computer Output.

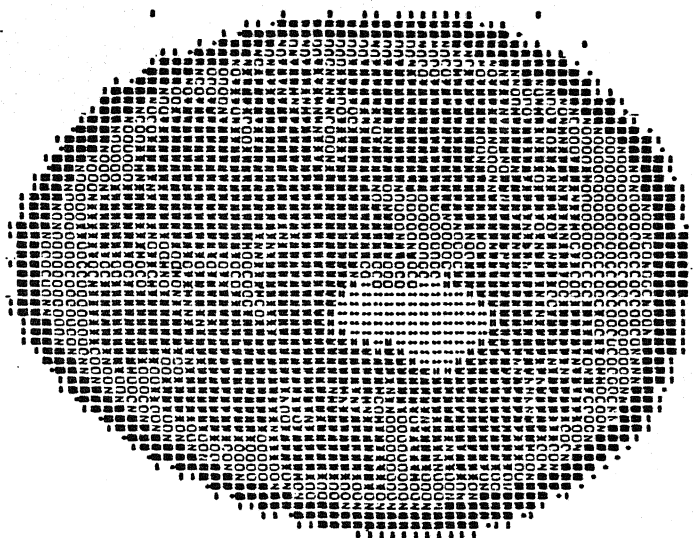
HANV17/257.64 F64X64 CODED PICTUREMPC= 64NPIX= 64MANGLE= 400RAY= 256KP= 3KB= JICR1150RT=01UP=01WD=01F8P=0PERCNT=10.00000



MIN= -2MAX= 2ERRON= 0.21729CHRON= 0.21248UPPIXEL= 333MPIXELS 2512ERNING -1.99966ERNAX= 1.91827ERL1= 0.32271ERL2= 0.47548

Fig. B-5.18(c) - Computer Output.

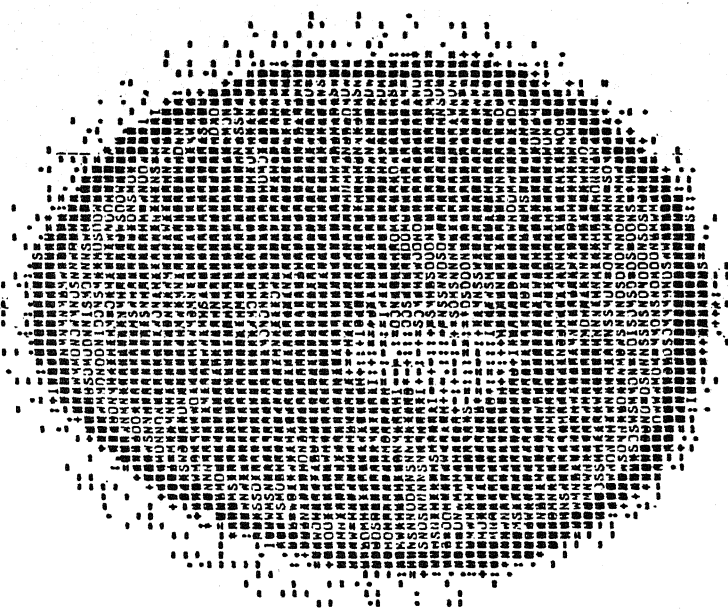
HANVIT/257.64 F64X64 CODED PICTUREMPIC= 64NPIC= 64MANGLE= 400RAY= 256RP= 3KB= JICR1150TY=0TUP=0IND=0ITFP=0PERCNT=10.00000



MIN= -2MAX= 2ERRON= 0.21729CHRON= 0.24248NPICEL= 333NPICEL= 2512ERRIN= -1.99966ERRMAX 1.91027ERRU= 0.32271ERRL2= 0.47560

Fig. B-5.18(c) - Computer Output.

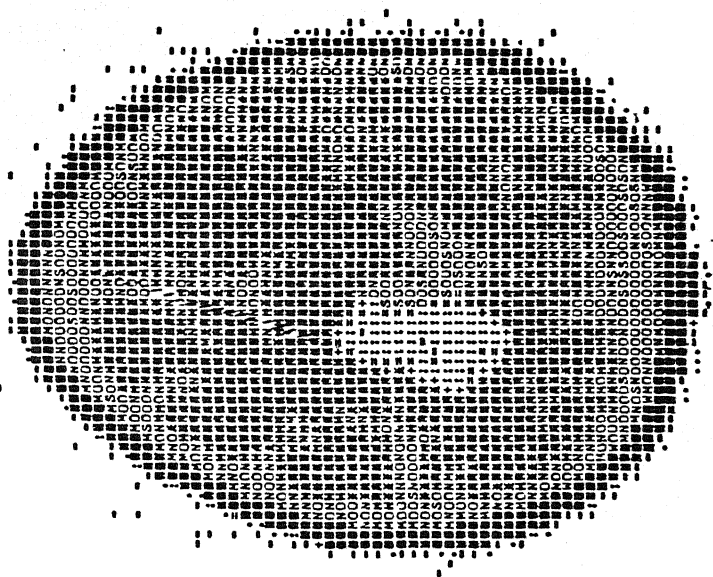
SNP257.64 FCFJ64X64 CODED PICTUREMPIC= 64NPIC= 64NANGLE= 100NRAY= 64KPE JK= 31CNEI1DONT=01WP=01WD=01F8P=0PERCENT=10.00000



MIN= -11MAX= 11ERR04= 1.4564/CR04= 1.6015/PIXEL= 330JMPXEL= 2512ERNIN= -10.5205ERNAX= 11.09213ERUJ= 1.66070ERL2= 2.33447

Fig. B-5.19(a) - Computer Output.

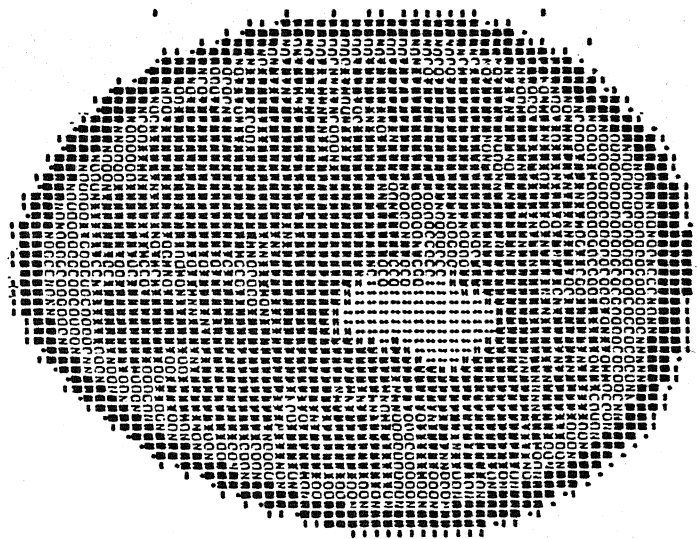
SNRPP257.64 F64X64 CODED PICTURENPIC= 64NPIC= 64NANGLE= 200NRAY= 128KPS 3KBM JTR=115URTY=1P=0JWD=0IFAP=0PERCMT=10.00000



LINE -SHAPE 628000 0.99904CHROM 0.67476NPIC= 3332NPIC= 2512ERNIM =-0.56922ERMAX 0.70419ERLL= 0.74185ERL2= 1.06306

Fig. B-5.19(b) - Computer Output.

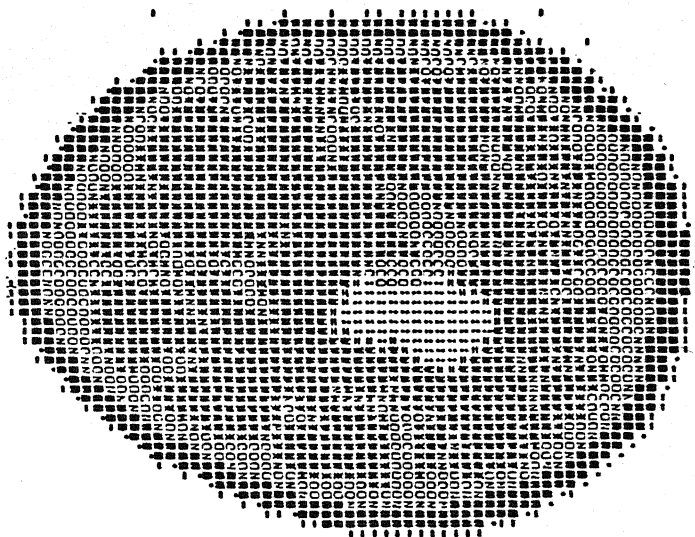
8HPJ57.64 F61A64 200ED PICTUREHPIC= 64NPIC= 64NANGLE= 400ARAY= 256KP= 3AB= JICRELLSURV=UIP=0IUD=0IFBP=0PERCNT=10.00000



MIN= -2MAX= 2ERROR= 0.24550ERROR= 0.26513NPICEL= 332MPICEL= 2512ERMIN= -2.12036ERMAX= 1.94811ERL1= 0.34940ERL2= 0.52072

Fig. B-5.19(c) - Computer Output.

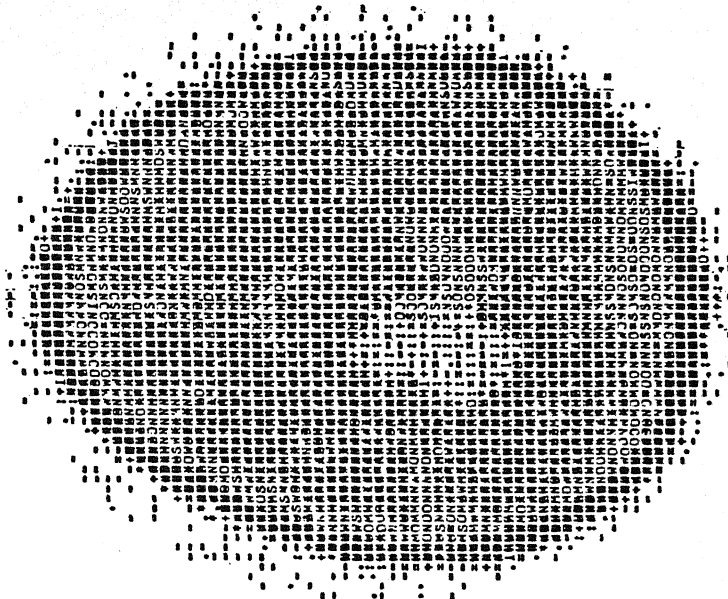
8HPJ57.64 F64N64 200ED PICTUREHPIC= 64NPIC= 64NANGLE= 400NARY= 256KP= 38N= 312RILLISURY=91P=01UD=01P=0PERCENT=10.00000



MIN= -2MAX= 2ERNJ= 0.24550CRRUN= 0.26513HPICEL= 332MPICEL= 2512ERNIN= -2.10J6LMAX= 1.94U11ERLJ= 0.34940CRJ2= 0.52072

Fig. B-5.19(c) - Computer Output.

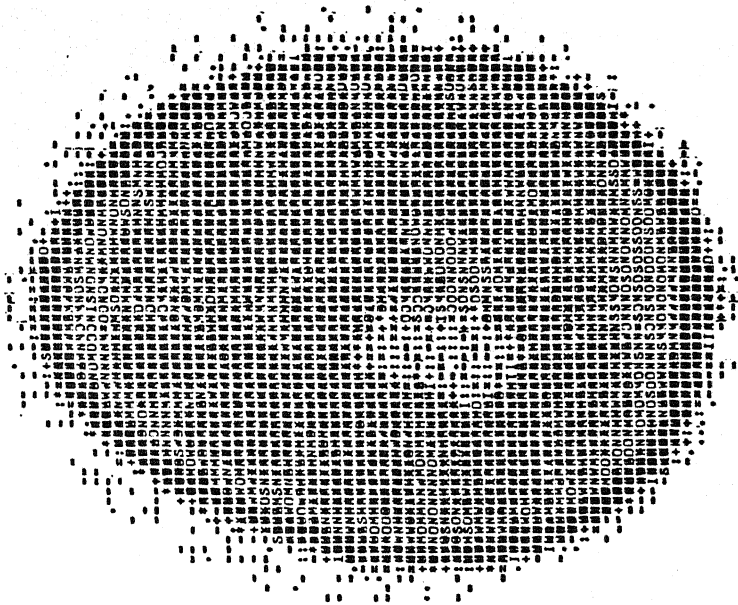
HANDJ/257.64 PCTJ6X64 CDOED PICTUREPIC= 64PIC= 64ANGLE= 100RAI= 64KP= JK= 31CK=110KTY=01UP=01ND=01P=0PERCENT=10.00000



MN= -11MA= 12ERR= 1.64VUSCROR= 1.809/INPIC= 330NPIXEL= 251ZERMIN= -11.11000R4AM 11.16273ERLI= 1.04842ERL2= 2.59744

Fig. B-5.20(a) - Computer Output.

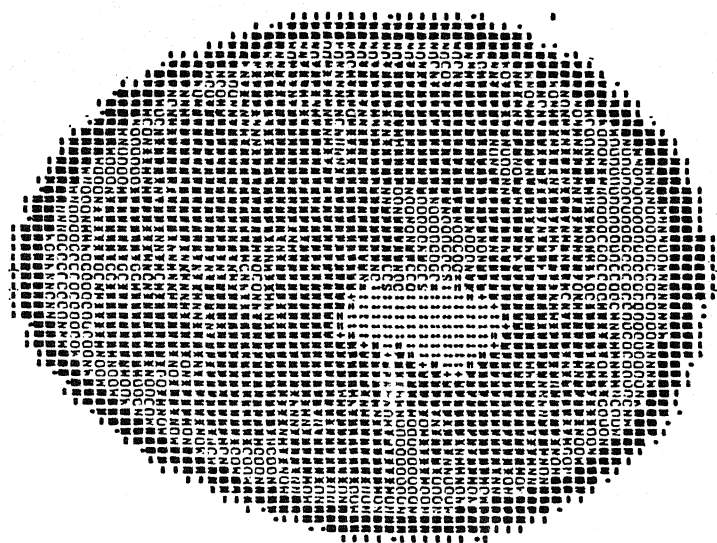
HAM/5/25/64 PCFJ64X64 CODED PICTUREMPIC= 64NPIC= 64ANGLE= 100RAY= 64KP= JK= 31ENALISQNT=01MP=01JD=01FP=00PERCNT=10.00000



MIN= -12MAX= 12ERROR= 1.7665JCRRON= 1.94029NPICEL= 3308MPICEL= 2512ERNIN= -11.66728ERRAAP 14.18661ERUI= 1.97173ERUI2= 2.78377

Fig. B-5.21(a) - Computer Output.

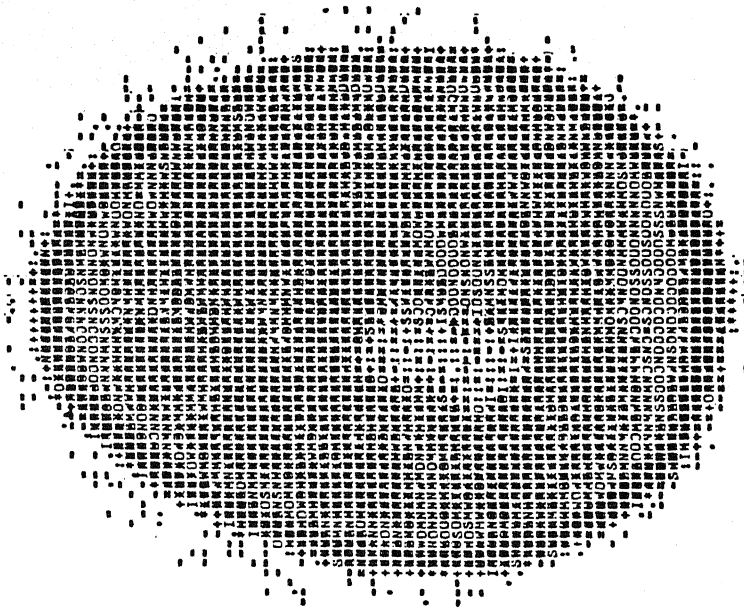
HA75/257.64 F64X54 CODED PICTUREMPIC= 64MPIC= 64NANGLE= 400HAY= 256Kp= 3Kp= JIC=18UR1=01HP=01ND=01FP=0PUCM=10.00000



NIN= -3MAX= 3ERROR= 0.40546CRRUN= 0.45701NPIXEL= 3332NPIXEL= 2512ERRIN= -2.91600LRAAM= 4.78667ERL1= 0.50580ERL2= 0.77594

Fig. B-5.21(c) - Computer Output.

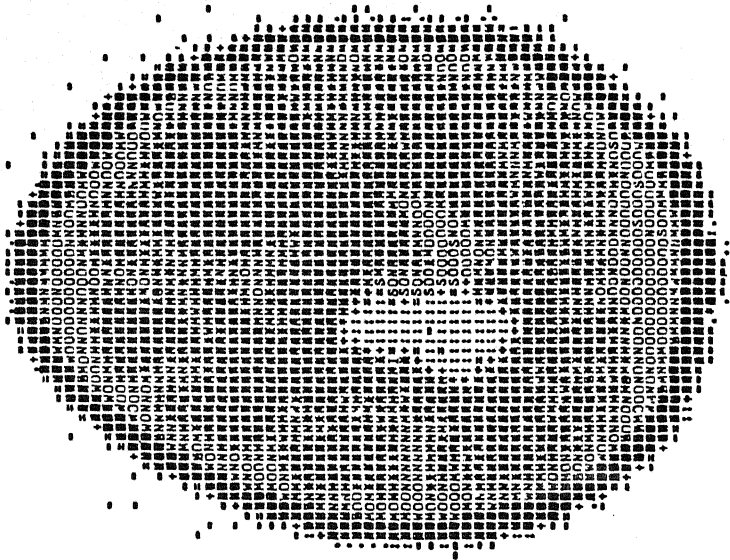
CUS257.64 PCT/BAK64 CODED PICTURENPIC= 64NPIC= 64ANGLEX 100HAX= 64KP= 3K0= 31CH=1150HT=01WP=01ND=01PBP=0PERCNT=10.00000



MIN= -14MAX= 13ERROR= 1.96675CRD0= 2.15804NPICEL= 330NPICEL= 2512CRD1= -13.50310ERR0= 12.99261ELC1= 2.18963ERR2= 3.19123

Fig. B-5.22(a) - Computer Output.

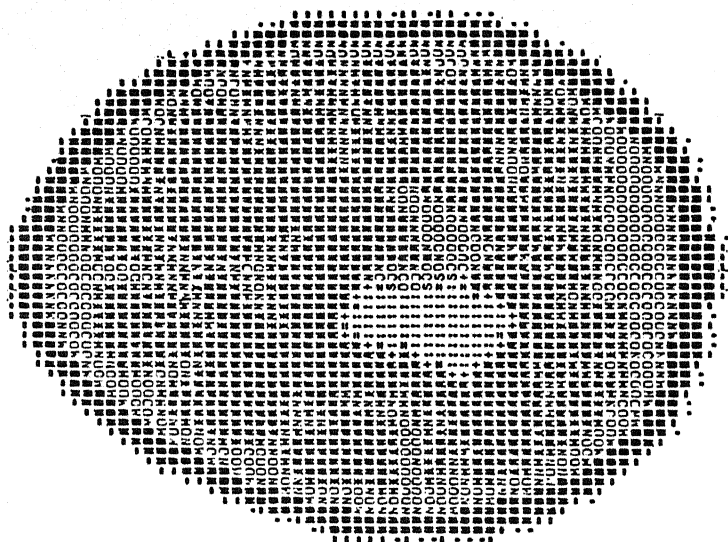
COSINE257.64 F64X64 CODED PICTUREPIC= 64NPIC= 64NANGLE= 200NAY= 128KP= 3KB= 4ICR=118URT=14P=01MD=0TFBP=0PCNCWT=10.00000



MIN -7MAX= 7ERROR= 0.97209CRORA= 1.08997NPICEL= 3332NPICEL= 2512ERMIN= -6.70614ERNAY= 7.42464ERLI= 1.45458ERL2= 1.73601

Fig. B-5.22(b) - Computer Output.

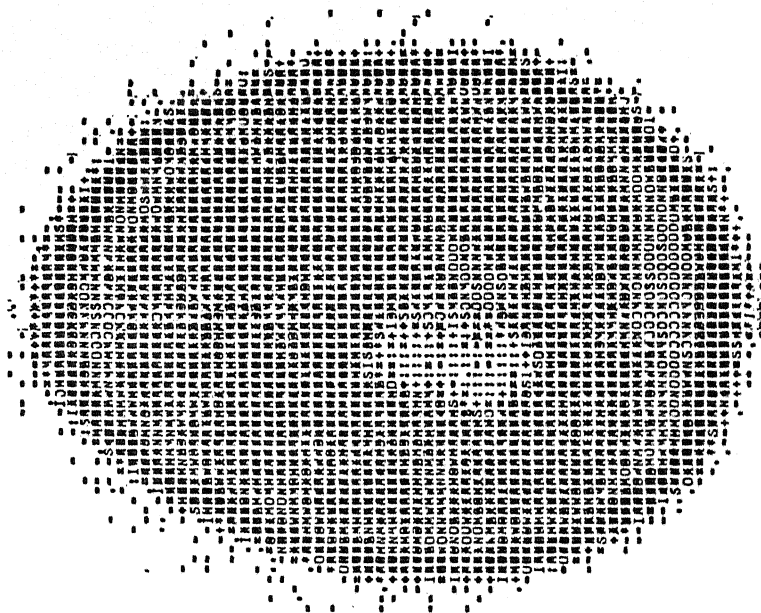
C0257.64 76166 CODED PICTURENPIX= 64NPIX= 64NANGLE= 400NRAZ= 256Kp= 3Kp. JTC=LSURICUTP=0LMD=0IFSP=0PERCUT=10.00000



NINE -3NAX= 3ERRON= 0.47869CHRON= 0.537N2PIXEL= 333NPIXEL= 2512ERNIN= -3.203WINNAX= J,0139ERU1= 0.68212ERU2= 0.90353

Fig. B-5.22(c) - Computer Output.

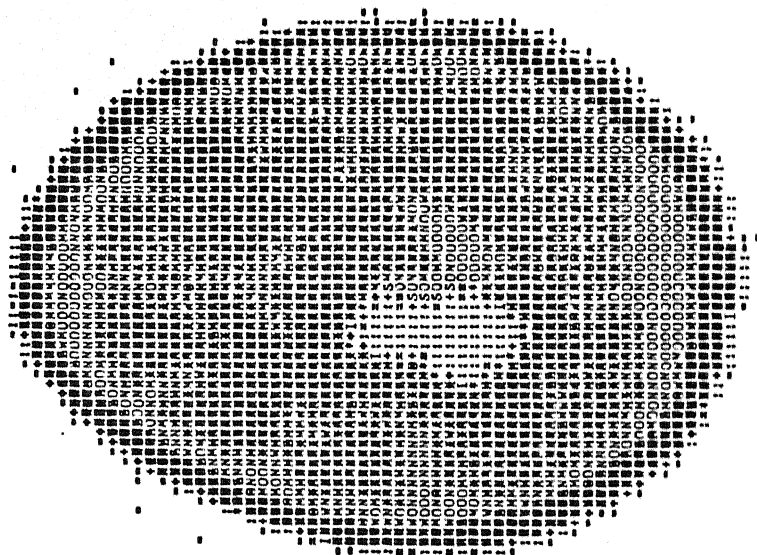
HANS4/257.64 FCISJ1X64 CODED PICTUREMPIC= 64NPIC= 64NANGLEZ= 100NRIY= 64KPS JKPS= 31JUN=1150RT=01HP=01HD=01RP=0PERCENT=10.00000



MIN= -14MAX= 14ERRDR= 2.1109ZERRUN= 2.61545NPICUL= 330MPICUL= 2512ERNIN= -14.00411ERNMAX= 17.46712ERUL= 2.64191ERNL2= 3.73435

Fig. B-5.23(a) - Computer Output.

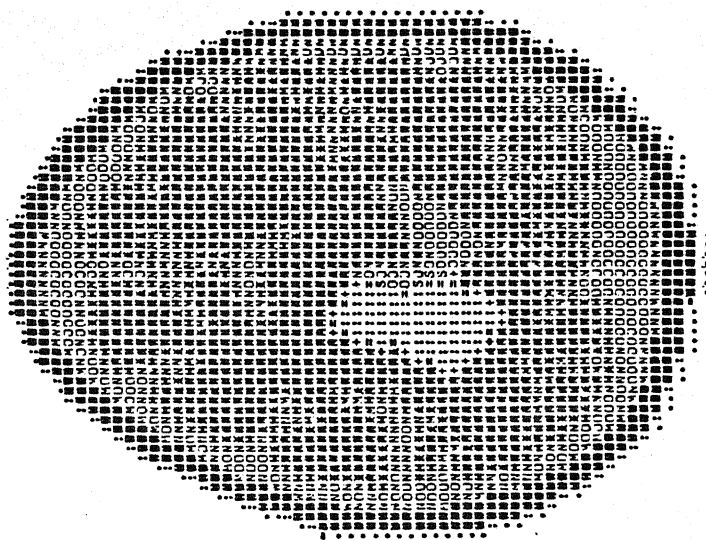
HAH54/257.64 F64X64 CODED PICTUREMPC= 64NPIC= 64MANGLE= 200RAY= 128KP= 3KR= JICR=180RT=0IMP=0IWD=0IFSP=0PERCNT=10.00000



MIN= -8MAX= 9ERROR= 1.24370CRORR= 1.39650NPICEL= 3332MPICEL= 2512ERMIN= -8.23R41CPMAX= 8.67867RLI= 1.45392ERL2= 2.20428

Fig. B-5.23 (b) - Computer Output.

HAM54/251.64 F61454 C30ED PICTURENPIC= 64NPIC= 64NANGLE= 400NRY= 256KP= 3KB. JICMAILBUNT=014P=01WD=01V8P=0PERCNT=10.00000



MIN= -4MAX= 4ERRON= 0.60474CRRON= 0.67396NPICEL= 3332NPICEL= 2512ERMIN= -4.06795ERMAX= 4.06284ERLI= 0.74845ERL2= 1.17176

Fig. B-5.23(c) - Computer Output.

Table C2 below is reproduced from Table (5.1) of Ref. [1].

Table C2 : Errors for the head phantom

NVIEW	NRAY	Δs	ERL1N	ERL2N
144	83	0.42672	0.1947	0.0858
288	165	0.21336	0.0900	0.0379
579	329	0.10668	0.0328	0.0154

We observe the errors ERL1N and ERL2N to be of the order $O(\Delta s)$, i.e., $O(1/R_c)$.

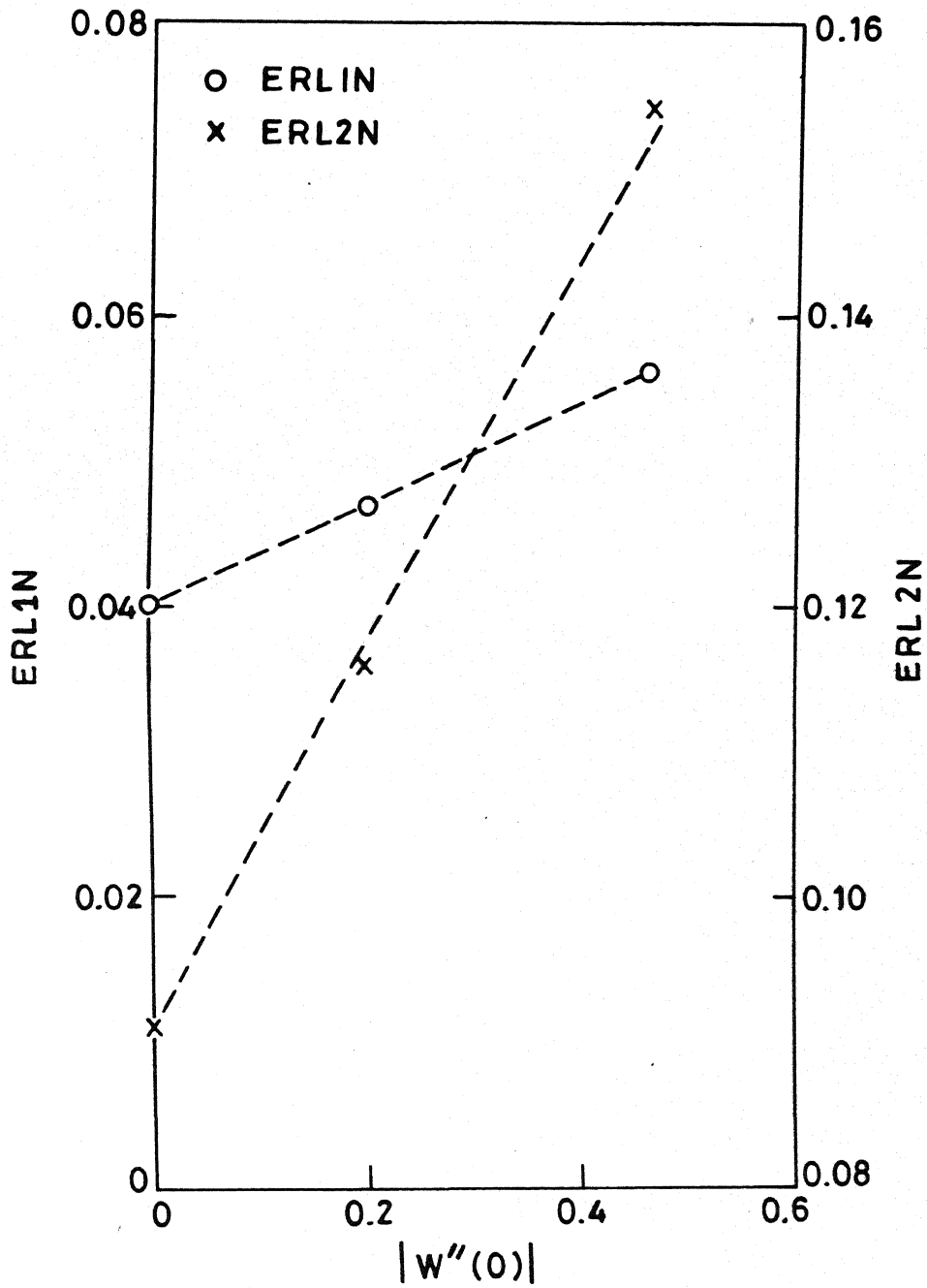


Fig. C1 Results of Table (C 1)

REFERENCES

1. G.T. Herman, "Image Reconstruction from Projections : The Fundamentals of Computerized Tomography", Academic Press, N.Y. (1980).
2. F. Natterer, "The Mathematics of Computerized Tomography", John Wiley & Sons, N.Y. (1986).
3. S.R. Deans, "The Radon Transform and Some of Its Applications", John Wiley, N.Y. (1983).
4. J. Radon, "Über die Bestimmung von Funktionen durch ihre Integralwerte langs gewisser Mannigfaltigkeiten", Berichte Sachsische Akademie der Wissenschaften Leipzig, Math.-Phys. Kl., 69 (1917), pp.262-267.
5. G.T. Herman and A. Naparstek, "Fast Image Reconstruction for Rapidly Collected Data", SIAM J. Appl. Math. 33 (1981), pp. 511-513.
6. R.N. Bracewell and A.C. Riddle, "Inversion of Fan Beam Scans in Radio Astronomy", Astroph. J. 150, (1967) pp. 427-434.
7. G.N. Ramachandran and A.V. Laxminarayanan, "Three Dimensional Reconstruction from Radio-Graphs and Electron Micrographs : Application of Convolution Instead of Fourier Transforms", Proc. Nat. Sci. Acad., U.S.A., 68 (1970), pp. 2236-2240.
8. L.A. Shepp and B.F. Logan, "The Fourier Reconstruction of Head Section", IEEE Trans. Nucl. Sci., NS-21 (1974), pp. 21-43.
9. T. Chang and G.T. Herman, "A Scientific Study of Filter Selection for a Fan Beam Convolution Algorithm", Siam. J. Appl. Math., 39 (1980), pp. 83-105.
10. F. Natterer, "A Sobolev Space Analysis of Picture Reconstruction", Siam J. Appl. Math., 39 (1980), pp. 402-411.
11. G.N. Hounsfield, "Computerized Transverse Axial Scanning Tomography : Part I, Description of the System", Br. J. Radiol., 46 (1973), pp. 1016-1022.
12. A.M. Cormack, "Representation of a Function by its Line Integrals with Some Radiological Applications", J. Appl. Phys., 35 (1964), pp. 195-207.

13. D. Kershaw, "The Determination of the Density Distribution of a Gas Flowing in a Pipe from Mean Density Measurements", J. Inst. Maths. Appls., 6 (1970), pp. 111-114.
14. P. Munshi, "Two-phase Flow Measurement Studies using a Scanning Gamma-ray Densitometer", Master of Science Thesis, Ohio State University, (1979).
15. F.A. Kulacki, P.A. Schlosser, A.C. DeVuono, and P. Munshi, "A Preliminary Study of the Application of Reconstruction Tomography to Void-Fraction Measurements in Two-Phase Flow", ANS/ASME/NRC Topical Meeting on Nuclear Reactor Thermal-Hydraulics, Saratoga Springs, New York, Nureg/CP-0014 (1980).
16. A.C. DeVuono, P.A. Schlosser, F.A. Kulacki, and P. Munshi, "Design of an Isotopic CT-Scanner for Two-Phase Flow Measurements", IEEE Trans. Sci., NS-27, 1 (1980), pp. 814-820.
17. P.A. Schlosser, A.C. DeVuono, F.A. Kulacki, and P. Munshi, "Analysis of High-speed CT Scanners for Non-Medical Applications", IEEE Trans. Nucl. Sci., NS-27, 1 (1980), pp. 788-794.
18. M.D. Seshadri, P. Munshi, I.D. Dhariyal, and R.K.S. Rathore, "Application of Digital Tomography in Two-phase Flow Studies", Nuclear Instruments and Methods A, A251, No. 3 (1986), pp. 577-582.
19. P. Munshi, R.K.S. Rathore, I.D. Dhariyal, and S.T. Swamy, "Tomographic Reconstruction of the Density Distribution using Discrete Fan Beam Algorithm", Nuclear Instruments and Methods, A257 (1987), pp. 398-405.
20. R.K.S. Rathore, P. Munshi, I.D. Dhariyal, and S.T. Swamy, "Tomographic Reconstruction of the Density Field using Radial Polynomials", Nuclear Technology, 78 (1987), pp. 7-12.
21. R.K.S. Rathore, P. Munshi, V.K. Bhatia, and S. Pandimani, "Point Density Measurements in Radially Symmetric Flows using the Bessels Functions", Amer. Nuc. Soc. Trans., 54 (1987), pp. 176-178.
22. R.K.S. Rathore, P. Munshi, and R.K. Jarwal, "Measurement of Void-Fraction Distribution using a Tomographic Chord-segment Inversion Technique", Proc. Cavitation and Multi-phase Flow Forum, Amer. Soc. Mech. Engrs., FED, 50 (1987), pp. 164-166.

23. G.C. McClellan and D.M. Tow, "Neutron Tomography of Damaged Fuel Assemblies", Neutron Radiography, Proc. Second World Conference, Paris (France), D. Reidel (1986), pp. 711-718.
24. S. Miyoshi, Y. Tanimoto, K. Uyama, and Y. Sano, "The Evaluation of SCC Defects of Steel Piping using High Energy X-ray CT Scanner", Nuclear Engg. and Design, 102 (1987), pp. 275-287.
25. W.H. Miller, "The Design of a Portable CAT Scanner for Utility Pole Inspection", Trans. American Nuclear Society (1986), 52, pp. 350-351.
26. "CT Scans for Butchers", Science Today, 22, 3 (1988), p. 26.
27. R.M. Lewitt, "Reconstruction Algorithms : Transform Methods", Proc. IEEE, 71, No.3 (1983), pp. 390-408.
28. S. Goldberg, "Unbounded Linear Operators", McGraw Hill (1966), p. 157.
29. P.R. Halmos, "Measure Theory", D. Van Nostrand, New York (1950).
30. E.C. Titchmarsh, "The Theory of Functions", 2nd Edition, Oxford U. Press (1939).
31. H. Berens and G.G. Lorentz, "Inverse Theorem for Bernstein Polynomials", Indiana Univ. Math. J., 21 (1972), pp. 693-708.
32. G.J. Romanes, Cunningham's Manual of Practical Anatomy, Vol. II, 14th Ed., ELBS Oxford U. Press, (1977).

APPENDIX C

The results summarised here have been reported by Herman [1] for the reconstruction of a head phantom. The sampling and the optimality conditions were satisfied in that study.

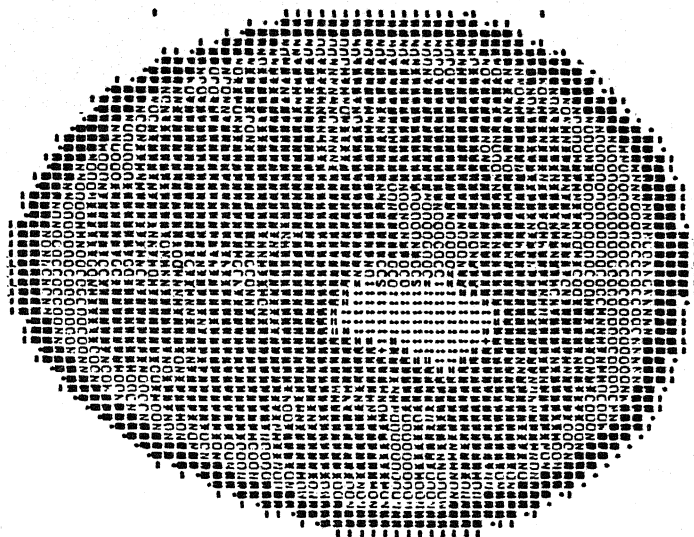
Table (C1) is reproduced from Table (5.1) of "Ref.[1].

Table (C1) : ~~Efrors~~ for the head phantom

Window	ERL1N	ERL2N
H99	0.0406	0.0913
H80	0.0465	0.1159
H54	0.0558	0.1544

Figure C1 shows that the errors vary almost linearly with respect to $|w''(0)|$.

HANS./257.64 F64464 CODED PICTUREMPIC= 64NPIG= 64NANGUE= 400NRAY= 256KP= 3KB= SICR118UR1=014P=01ND=0179P=0PERCENT=10.00000



MIN= -3MAX= 2ERR3N= 0.326#JCRRON= 0.36744NPIXEL= 3332#PIXEL= 2512ERMIN= -2.64157ERRMAX= 2.48837ERUI= 0.44976ERL2= 0.68371

Fig. B-5.20(c) - Computer Output.